

Flux of Suprathermal Ions measured by STEREO PLASTIC

Pick-Up Ions at 1 AU

Christian Drews
Diplomarbeit

*Abteilung: Extraterrestrische Physik
Institut für Experimentelle und Angewandte Physik
Christian-Albrechts-Universität zu Kiel*

Leiter der Arbeit:
Robert F. Wimmer-Schweingruber

September 28, 2009

Zusammenfassung

Die Solar Terrestrial Relations Observatory (STEREO) Mission startete im Oktober 2006 und besteht aus zwei identischen Raumsonden, wobei STEREO A (Ahead) der Erde voraus und STEREO B (Behind) der Erde hinterher läuft. Der Abstand zwischen STEREO A/B und der Erde vergrössert sich dabei um 22.5° pro Jahr. An Bord beider Raumsonden befindet sich das Plasma and Suprathermal Ion Composition Instrument (PLASTIC), welches in-situ die Eigenschaften schwerer Sonnenwind Ionen misst. Mit PLASTIC ist es ebenso möglich Ionen in einem Energiebereich oberhalb der Sonnenwind-Energie zu messen, dem sogenannten suprathermalen Bereich. Dies wird durch zwei getrennte Sektoren im Instrument erreicht. Der Sonnenwind-Sektor ist auf der Verbindungsleitung zwischen Raumsonde und Sonne zentriert und misst in einem Winkelbereich von 45° innerhalb und $\pm 20^\circ$ ausserhalb der Ekliptik, während die Wide Angle Partition (WAP) einen Winkelbereich von 210° in azimuthaler und $<10^\circ$ in polarer Richtung umfasst.

Der Schwerpunkt dieser Arbeit ist die Untersuchung von suprathermalen Pick-Up Ionen (PUIs), welche als Neutralteilchen durch solare Strahlung und Ladungsaustausch mit den Protonen des Sonnenwindes ionisiert und vom Magnetfeld des Sonnenwindes davongetragen werden. Das Magnetfeld zwingt die Teilchen senkrecht zum Magnetfeldvektor mit der Geschwindigkeit des Sonnenwindes zu gyrieren, was wiederum in einer charakteristischen Geschwindigkeitsverteilung der Pick-Up Ionen resultiert [Vasyliunas and Siscoe, 1976].

Zuerst geben wir einen Überblick über relevante physikalische Prozesse in der Heliosphäre, gefolgt von einer allgemeinen Einführung in die STEREO Mission und dem Instrument PLASTIC. Aufgrund ihrer Seltenheit im Vergleich zu anderen Sonnenwind Ionen war die Messung von Pick-Up Ionen bis dato nur schwer durchführbar [Gloeckler and Geiss, 1998]. PLASTICs grosser Geometriefaktor erlaubt jedoch sowohl die Untersuchung der temporären Variabilität von Pick-Up Zählraten, als auch die Untersuchung ihrer Energie-Spektren innerhalb kurzer Zeiträume.

Zu diesem Zweck haben wir ein Python Programm geschrieben, welches in der Lage ist Pick-Up Helium, Kohlenstoff, Sauerstoff und Neon in einem Zeitraum von 700 Tagen zu analysieren. Mit diesem Programm untersuchen wir die Form der Pick-Up Geschwindigkeitsverteilung in einer Entfernung von einer astronomischen Einheit zur Sonne. Wir haben basierend auf unseren Resultaten eine Methode entwickelt, mit der es möglich ist, Teile eines Pick-Up Energie Spektrums zu rekonstruieren, welche vom Instrument durch dessen limitierte Energie-Bandbreite ($\sim 1 \text{ keV/e}$ bis $\sim 80 \text{ keV/e}$) nicht gemessen werden können.

Darüber hinaus untersuchen wir die zeitliche Variabilität von PUIs, wobei wir eine Kombination aus Zeit- und Geschwindigkeitsmittelung benutzen, welche die Effizienzbedingte Variabilität der Zählraten unterdrückt. Damit ist es erstmals gelungen, Anzeichen einer Fokussierung von interstellaren Staubpartikeln um die Sonne herum sichtbar zu machen.

Im Rahmen dieser Arbeit haben wir darüber hinaus die Universität von New Hampshire besucht, dem Sitz des "principal investigators" von PLASTIC, um bei einer "In-Flight"-Kalibrierung zu helfen, welche in Zukunft zu einer enormen Qualitätssteigerung der Datenprodukte führen wird.

Abstract

The Solar TErrestrial RElations Observatory (STEREO) mission was launched in October 2006 and consists of two identical spacecraft. STEREO A (Ahead) leads along Earth's orbit, while STEREO B (Behind) trails it with an angular distance increasing by 22.5° per year. On board both spacecraft is the Plasma and Suprathermal Ion Composition instrument (PLASTIC), which is designed to investigate in-situ bulk properties of solar wind heavy ions. In addition, PLASTIC measures ions in an energy range above the typical Solar Wind (SW) energy, so-called suprathermal ions. This is achieved by a solar wind sector, which is centered on the sun-Earth line, covering an angular view of 45° in and $\pm 20^\circ$ out of the ecliptic plane, and a suprathermal ion Wide Angle Partition sector (WAP), covering a 210° view in azimuthal and $<10^\circ$ in polar direction.

In this thesis we focused our investigations on PLASTIC's observation of suprathermal Pick-Up Ions (PUIs), which are neutral particles, that were ionized by solar radiation or charge exchange and then picked up by the solar magnetic field. The magnetic field forces them to execute cycloidal trajectories perpendicular to the magnetic field vector with the solar wind speed, which results in a characteristic velocity distribution of these particles ranging from $0 v_{SW}$ to $2 v_{SW}$ [Vasyliunas and Siscoe, 1976].

We give an overview of physical processes in the heliosphere followed by an introduction of the STEREO mission and the instrument PLASTIC. Until now, measurements of the pick-up ions were difficult due to their low abundance in respect to the solar wind composition [Gloeckler and Geiss, 1998]. With its big geometry factor, PLASTIC allows us to investigate the temporal variability of pick-up ions and also their velocity spectra within short periods.

We have developed tools to analyze pick-up helium, carbon, oxygen and neon in a period of 700 days with STEREO PLASTIC, that have been used to study the shape of velocity distributions of PUIs at 1 Astronomical Unit (AU). Based on our results we have developed a method to reconstruct parts of the energy spectra, that can not be measured by the instrument due to its limited energy coverage of ~ 1 keV/e to ~ 80 keV/e.

Additionally, the temporal variability of PUIs has been studied. We were able to attenuate the efficiency related variations of pick-up ion count rates by using a combination of time and velocity binning. With that, we analyzed big scale structures of the PUI abundances and found first evidence of focusing of heavy pick-up ions, i.e. C^+ and O^+ , similar to the gravitational focusing of He^+ around the sun.

In the framework of this thesis, we have also visited the principle investigator institution, the University of New Hampshire, and helped to perform an in-flight calibration, that will result in a considerable improvement of PLASTIC data.

Contents

1	Introduction	3
1.1	Motivation	3
1.2	Structure of this Work	3
1.3	Solar Physics	5
1.3.1	Solar Wind	5
1.3.2	Pick-up Ions	5
1.4	STEREO Mission	8
1.4.1	Overview	8
1.4.2	Scientific goals	9
1.4.3	Instrumentation on STEREO A/B	9
2	PLASTIC	11
2.1	Overview	11
2.2	Scientific Objectives	11
2.2.1	Solar Processes and Solar Wind Studies	11
2.2.2	Interplanetary Manifestations of Coronal Mass Ejections (ICMEs)	11
2.2.3	Injection and Acceleration of Ions at CME-Driven Shocks	11
2.2.4	Heliospheric Studies	12
2.3	Instrument Description	12
2.3.1	Entrance System / Energy Analyzer	12
2.3.2	Time of Flight / Energy Chamber	17
2.3.3	Measurement Procedure	18
2.4	Pulse Height Analysis Words	19
2.5	ET Matrix	22
2.5.1	Overview	22
2.5.2	Data Accumulation	22
2.5.3	Interpretation	25
2.5.4	Analysis	27
3	Data Analysis	31
3.1	Heavy Pick-up Ions with PLASTIC	31
3.1.1	Overview	31
3.1.2	Data Accumulation	31
3.1.3	Ion Species Classification	32
3.1.4	v_{ion}/v_{SW} Distribution	34
3.1.5	Reconstruction of the O ⁺ w Spectrum	39
3.1.6	Discussion	43
3.2	Implications on Heavy Pick-up Abundances	45
3.2.1	Heavy Pick-up Ion Abundances with PLASTIC	45
3.2.2	Sungrazing Comets	55

3.2.3	Focusing Cone	56
3.2.4	Inner-source Pick-up Ions	61
4	Outlook	63
4.1	Detection Efficiency with PLASTIC	63
4.2	Virtual Detector	64
4.3	Rate Data	66
5	Summary & Conclusions	69
A	Appendix	71
A.1	Energy Conversion	71
A.2	MCP Bias	72
A.3	Ion Positions in ET Matrix	73
A.3.1	TOF Position	73
A.3.2	SSD Position	74
A.4	PLASTIC In-Flight Calibration	78
A.4.1	Mass per Charge Table	78
A.4.2	Mass Table	80
A.4.3	Discussion	80
A.5	Geophysical Research Letters Submission	83
List of Abbreviations		89

1 Introduction

1.1 Motivation

One of the most interesting developments in space physics in the last few years has been the detection of interstellar particles in form of pick-up ions in the heliosphere [Bertaux, 1971], which originate from interstellar neutrals penetrating the heliosphere. On their way to the sun, these particles are gradually ionized by solar radiation or charge exchange. Once ionized, the ionization probability strongly decreases due to a higher second ionization potential, thus pick-up ions are almost always singly charged. Nevertheless, the criterion of single charge states is not sufficient to distinguish PUIs from the remaining solar wind composition, as singly charged ions are also present in the solar wind.

The Heliospheric Magnetic Field (HMF), which is convected outwards with the solar wind, forces PUIs to move on Larmor orbits around the HMF. The resulting velocity distribution is a shell like distribution centered on the solar wind bulk speed with a radius approximately equal to v_{SW} in velocity space and differs strongly from a typical solar wind ion velocity distribution. Thus, we have the opportunity to investigate parameters of the Local InterStellar Medium (LISM) in-situ, i.e. temperature, density and composition, by observations of interstellar pick-up ions [Geiss *et al.*, 1993].

Recent investigations on pick-up ions by Geiss *et al.* [1995] showed signatures of a pick-up ion species, that has a highly thermalized velocity distribution and is attributed to a source being only few radii away from the sun. Adiabatic cooling by the expanding solar wind is the reason for the observed distribution. These, so called, Inner-Source Pick-Up Ions (ISPU) are believed to originate from solar wind particles, which interacted with interplanetary or interstellar dust [Schwadron and Geiss, 2000].

In respect to the solar wind composition, the abundance of pick-up ions, especially C^+ , N^+ , Ne^+ and O^+ , is very low. Thus, PLASTIC is an ideal instrument for investigations of PUIs due to its big geometric factor. In addition, the sun's current low state of activity allows us to observe pick-up ions without interference of Coronal Mass Ejection (CME) -related enrichments of PUIs [Berger, 2009].

By analyzing time series of inner-source pick-up ions with PLASTIC, one can improve the understanding of the dynamics of interstellar and interplanetary dust particles in the heliosphere. We especially address the question, whether gravitational focusing of dust particles could lead to the observed variation of ISPU count rates measured with PLASTIC.

1.2 Structure of this Work

In chapter 1, we give a brief overview of the solar wind and its magnetic field, followed by a description of pick-up ions. Although, our analysis is mainly based on results of the instrument PLASTIC, mounted on board the two STEREO spacecraft, we also describe

the importance of this mission and its instrumentation in general. In chapter 2, we explain PLASTIC in more detail, which includes a description of its complex entrance system, functional breakdown and measurement procedure. The chapter ends with an explanation of PLASTIC's data products and an example of how to derive physical quantities from it.

In chapter 3, we describe our analysis of pick-up ions, which contains an extensive discussion on pick-up ion data with PLASTIC. Additionally, we discuss temporal variations of observed ISPUI abundances and their implications on the nature of the inner source. Chapter 4 and 5 contain a short summary of our results and an outlook of investigations, which will be done in the future. At last, we present in the appendix of this work calibration results, which were needed for our investigations of pick-up ions.

1.3 Solar Physics

1.3.1 Solar Wind

The solar wind is a steady stream of highly ionized plasma originating at the sun. It was first measured in 1959 by the spacecraft Lunik 1 and three years later by Mariner 2 on its way to Venus, leading to E. N. Parker's famous hydrodynamic model of the solar wind. The solar plasma mainly consists of protons and helium ions ($\sim 96\%$ and $\sim 4\%$ respectively) with small fractions of heavier ions with masses above four atomic units, all traveling with supersonic speed of about 400 km/s to 800 km/s. The source of the slow solar wind (≤ 400 km/s) lies near the solar equator, which is mostly dominated by closed magnetic loops, while the fast solar wind (≥ 400 km/s) originates from coronal holes, which are dark and cold areas in the corona dominated by open magnetic field lines, as shown in figure 1.1. The solar wind is heavily affected by the 11 year solar cycle, which is caused by the sun's magnetic pole reversal. During solar maximum the sun's magnetic field undergoes pronounced changes resulting in a complicated multipole structure. Thus, the solar wind will be most variable in this time resulting in numerous heliospheric phenomena, like Coronal Mass Ejections (CMEs), corotating interaction regions (CIRs), solar flares, et cetera. These are further described in *Kallenrode* [2004]. Currently the sun is in a phase of low activity with a distinct dipole structure of the magnetic field, which makes it an ideal time to study pick-up ions without interferences by CMEs or solar flares. An illustration on the solar cycle and further descriptions are presented in figure 1.2.

Embedded in the solar wind is the solar magnetic field. Because of the high conductivity of the solar wind plasma the field lines are frozen into it and carried outward. The sun's sidereal rotation period of 27 days then winds up the magnetic field lines and forms an Archimedean spiral with

$$B(r) = \frac{B_0 r_0^2}{r^2} \sqrt{1 + \left(\frac{w_\odot}{u_r}\right)^2}, \quad (1.1)$$

where r_0 denotes a reference point, B_0 the magnetic field strength at r_0 , w_\odot the solar angular frequency and u_r the radial component of the solar wind velocity. Although this is the most commonly used model of the solar magnetic field, it is still a strong simplification without considerations of small scale effects within the solar atmosphere. A more elaborated characterization of the heliospheric magnetic field was done by *Fisk* [1996].

1.3.2 Pick-up Ions

The sun and its surrounding planets are embedded into the Local Interstellar Cloud (LIC) and form a vacancy in space called heliosphere. It emerges from supersonic solar wind flowing radially away from the sun, which is then decelerated by the inflowing Local Interstellar Medium (LISM), leading to a "bubble" in space that can not be penetrated by the local interstellar plasma. Instead, the ram pressure of solar wind and LISM will form an equilibrium at the heliopause, which marks the outer boundary of the heliosphere. Solar wind and LISM plasma are decelerated to subsonic speed resulting in the formation of two shocks, the termination- and bow shock. While latter has not

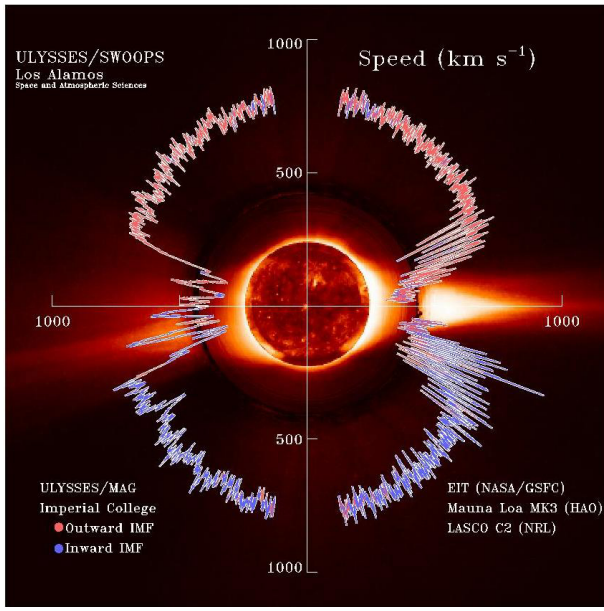


Figure 1.1:

This figure shows the solar wind velocity measured by the Ulysses spacecraft on its latitude scan. During solar minimum the slow solar wind mainly originates from the equator region of the sun, which is dominated by closed magnetic loops. The fast solar wind emerges from open field lines at higher latitudes. In solar maximum however the complicated magnetic topology and multipole structure of the solar magnetic field lead to predominant slow wind streams at all heliographic latitudes. The picture is taken from the NASA internet site <http://science.nasa.gov>.

yet been measured directly, the termination shock has been in 2004 and 2007 by the Voyager spacecraft, which is illustrated in figure 1.3. It is situated at a distance of about 90 AU from the sun depending on the heliographic longitude, whereas the bow shock is believed to be at 230 AU.

Although the interaction between solar wind and LISM prevents interstellar plasma to enter the heliosphere, we are still able to obtain information on the LISM by investigating its neutral component, which can penetrate the heliopause without interference. The neutrals enter the heliosphere with a relative speed of 20 to 25 km/s and are gradually ionized by charge exchange with solar wind protons and solar UV radiation. These new born pick-up ions are then subjected to a variety of plasma processes forming their typical velocity distribution function. It results from solar wind, which convects the newly created ions outwards with v_{SW} , while the magnetic field forces them to execute a cycloidal trajectory with the guiding center moving perpendicular to \hat{B}_{SW} with v_{SW} .

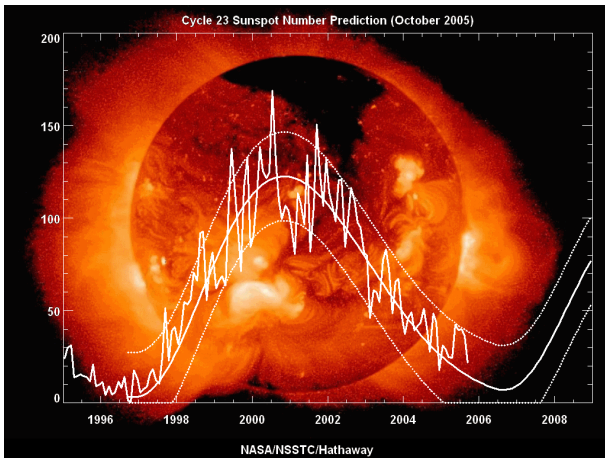


Figure 1.2:

Here the sunspot number is plotted over time. Sunspots are believed to be the visible counterparts of magnetic flux tubes in the convection zone of the sun and are an indicator for the current state of the sun's activity, whereas a high number of sunspots denotes solar maximum. The picture is taken from the NASA internet site <http://science.nasa.gov>.

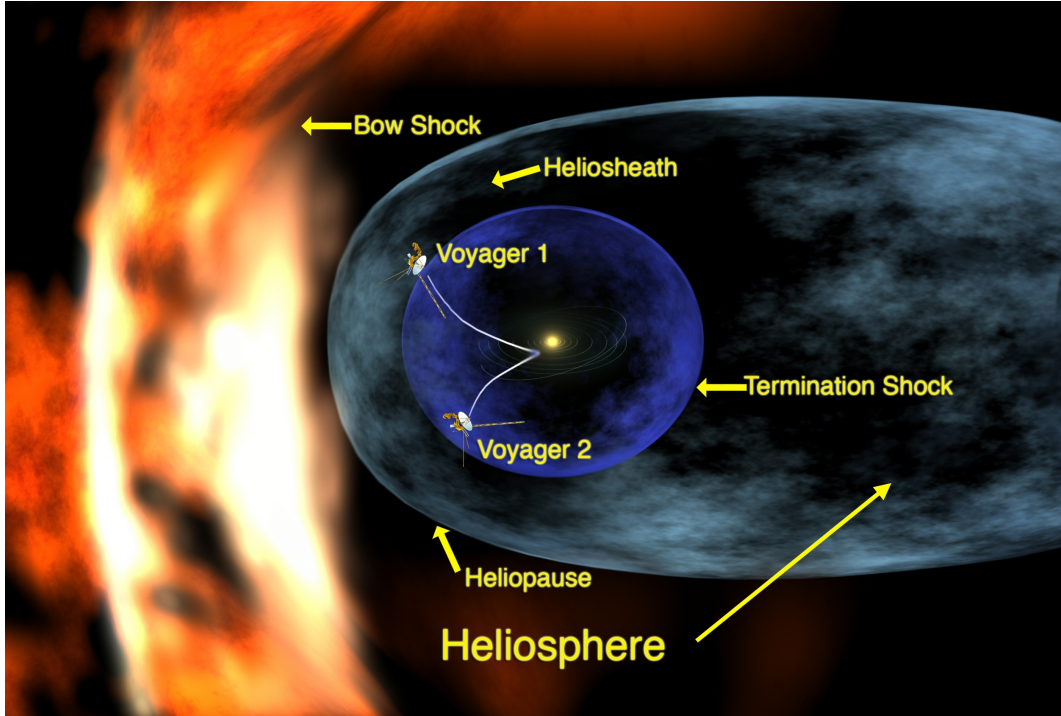


Figure 1.3: An illustration of our heliosphere together with the Voyager mission. The picture is taken from the NASA internet site <http://science.nasa.gov>

Far away from the sun, where the magnetic field direction can be considered to be at right angle with the outflowing solar wind plasma, the velocity of these ions then ranges from $0 v_{SW}$ to $2 v_{SW}$, resulting in a ring like velocity distribution of pick-up ions. Neglecting pitch angle scattering we obtain the velocity distribution from *Vasyliunas and Siscoe* [1976]

$$f(v_{\perp}, v_{\parallel}) = \frac{N_0 V_0}{\pi v_{SW}^3 r} \lambda \cdot \exp \left\{ -\frac{\lambda}{r \sin \Theta} \left(\frac{v_{SW}}{v_{\perp}} \right)^2 \right\} \delta(v_{\parallel}) \quad v_{\perp} > v_{SW}, \quad (1.2)$$

where N_0 is the neutral density of the local interstellar medium, $V_0 \simeq 25$ km/s the relative speed of the LISM, $\lambda = a^2/V_0 \tau_a$ a characteristic distance with ionization time τ_a at some reference distance a , v_{SW} the solar wind velocity, Θ the angle between the direction of the sun's motion relative to the neutral gas and the line connecting P, which is the point of measurement and r the distance of the sun to point P.

A detector with large velocity space acceptance like STEREO PLASTIC, which is capable of separate measurements of the dominant solar wind species, i.e. helium and hydrogen, and the less abundant solar wind heavy ions by its two different entrance slits, is well suited for observation of rare pick-up ions. Recent investigation on interstellar pick-up ions and their implication on parameters of the LISM are presented in *Cummings et al.* [2002].

The fact, that neutral particles are able to penetrate deep into the heliosphere results in the formation of a cone-like enrichment of He^+ behind the sun in respect to the in-flow direction of the LISM. It emerges from neutral interstellar helium, which is affected by the sun's gravitational force. The enhanced density of interstellar helium in this region

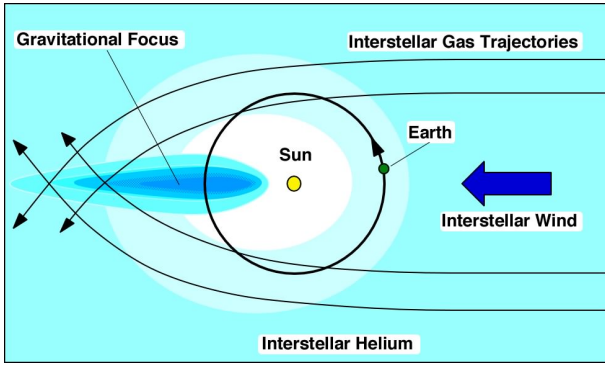


Figure 1.4:

This figure shows an illustration of the helium cone, which forms behind the sun caused by its gravitational field. A spacecraft, positioned at the Lagrangian point one, would measure an enhancement of He^+ every year at the same time. The picture is taken from *Moebius [2009]*.

then leads to an increased creation of pick-up ions in this area. An illustration of this focussing is shown in figure 1.4. Although this phenomenon has been measured for He^+ by numerous sources, other interstellar neutrals do not necessarily underlie the same focussing effect. Interstellar protons are a special case, since the radiation pressure of the sun annihilates the influence of the gravitational force. For elements heavier than helium such as oxygen, carbon, nitrogen and neon the focussing has not yet been discovered. This is mainly due to their poor observability, which emanates from their low abundance in respect to the solar wind composition.

A second well known phenomenon caused by pick-up ions are anomalous cosmic rays. They are created when interstellar ions are accelerated at the termination shock by diffusive shock acceleration leading to enhanced particle energies. A detailed discussion on anomalous cosmic rays is given in *Cummings et al. [2002]*.

Although we were mainly referring to interstellar neutrals when discussing pick-up ions, they can also originate from inner sources in the heliosphere, like dust grains orbiting the sun at small distances, sungrazing comets or planetary atmospheres emitting neutrals. These sources will be described later in this thesis together with data analysis of pick-up ions with PLASTIC.

1.4 STEREO Mission

1.4.1 Overview

The STEREO (Solar TERrestrial RElations Observatory) Mission was launched in October 2006 and consists of two identical spacecraft orbiting the sun. STEREO A (Ahead) leads along Earth's orbit while STEREO B (Behind) trails it with an angular distance increasing by 22.5° per year, leading to a total circulation period of 346 and 388 days respectively. Viewed from the sun, the two spacecraft separate at approximately 44° to 45° degrees per year and therefore allow the investigation of 3-dimensional heliospheric structures. While its main goal is the observation and examination of CMEs (Coronal Mass Ejections), the persistent stream of in-situ data from the four main instrument packages also allows the forecast of space weather. Figure 1.5 shows a concept drawing of STEREO A together with a picture of its orbit around the sun.

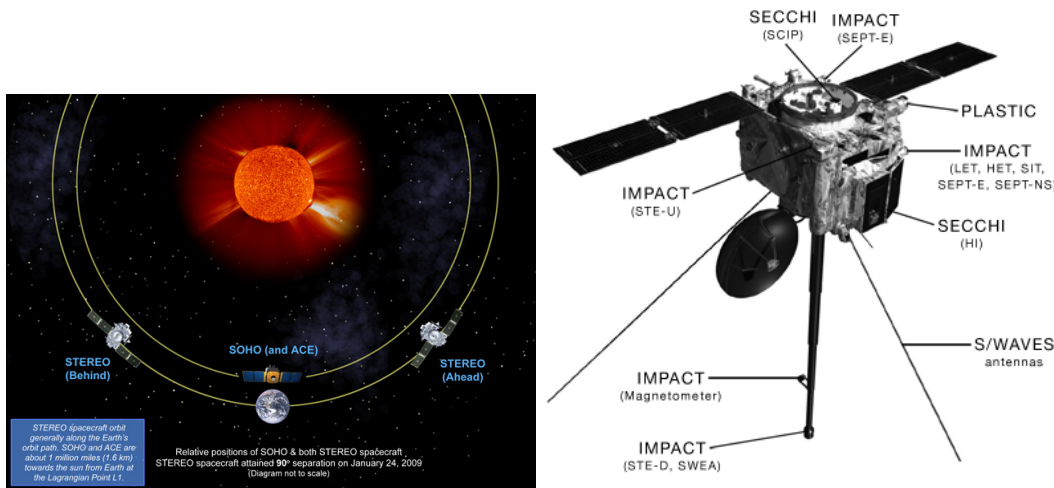


Figure 1.5: The left picture shows both spacecraft on their orbit around Earth. Also shown is the relative position of the ACE-spacecraft at the Lagrangian Point L1. The shown 90° separation of STEREO A and B was attained on 24. January 2009 and marks phase 2 of the mission, where triangulation on CMEs is optimal (diagram not to scale). The right picture shows a concept drawing of STEREO A, which differs from STEREO B only in minor details, due to the fact that the antennas have to face Earth. The picture is taken from the NASA internet site <http://science.nasa.gov>

1.4.2 Scientific goals

The main mission objective is to understand the origin and evolution of CMEs from the sun to their arrival at Earth. It can be described by the following four scientific objectives:

- Understand the causes and mechanisms of coronal mass ejection initiation.
- Characterize the propagation of CMEs through the heliosphere.
- Discover the mechanisms and sites of energetic particle acceleration in the low corona and the interplanetary medium.
- Improve the determination of the structure of the ambient solar wind.

To obtain these goals, it was required for both spacecraft to continuously measure for a period of 150 days, which was accomplished on June 21, 2007 (Minimum success). Full success of the mission required measurement of both spacecraft for a period of 2 years, finally accomplished on January 23, 2009.

1.4.3 Instrumentation on STEREO A/B

The STEREO Mission consists of four measurement packages with a total number of 18 individual sensors, all suited to contribute to the scientific goals of the mission. We will briefly present the instrumentation in this section.

Sun Earth Connection Coronal and Heliospheric Investigation (SECCHI)

SECCHI consists of an extreme ultraviolet imager, two white-light coronographs and a heliospheric imager and therefore allows to study the 3-dimensional evolution of coronal mass ejections from the sun towards its eventual impact on Earth.

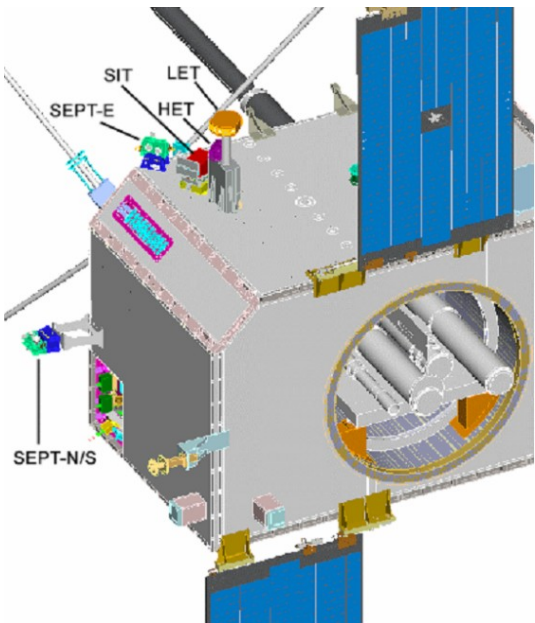


Figure 1.6:

In-situ Measurements of Particles and CME Transients (IMPACT)

IMPACT is composed of seven instruments, where SWEA (Solar Wind Electron Analyzer), STE (Suprathermal Electron instrument), MAG (Magnetic field experiment) are located on the six-meter deployable boom, while SEPT (Solar Electron and Proton Telescope), SIT (Suprathermal Ion Telescope), LET (Low Energy Telescope), HET (High Energy Telescope) are mounted on the main body of the spacecraft. IMPACT measures the 3-D distribution of solar wind plasma electrons, the characteristics of Solar Energetic Particles (SEPs) ions and electrons, and the interplanetary magnetic field. *Luhmann et al. [2007]*. The instrument is shown in figure 1.6.

STEREO/WAVES (SWAVES)

SWAVES is an interplanetary radio burst tracker, measuring radio disturbances and plasma waves from the sun. Its main goals are remote and in-situ measurements of radio sources, spatial extent and structure of CME-driven shocks, electron density and temperature in regions of cold dense plasma within CME-associated magnetic clouds. This is achieved by three mutually orthogonal monopole antenna elements, each six meters in length.

Plasma and SupraThermal Ion Composition (PLASTIC)

PLASTIC provides not only in situ measurements of solar wind protons, alpha particles and heavy ions, but also charge state, composition and spectra of suprathermal ions in a wide range of nearly 360° in the ecliptic. PLASTIC is described in more detail in the following section.

2 PLASTIC

2.1 Overview

The Plasma and Suprathermal Ion Composition (PLASTIC) instrument on STEREO measures in-situ bulk properties of solar wind protons, alphas and heavy ions. In addition, PLASTIC provides the composition and spectra of suprathermal ions in an energy-per-charge range of $\sim 0.3\text{keV}/e$ to $\sim 80\text{keV}/e$ and therefore has the capability to investigate the relationship between coronal and solar wind ion processes. A few examples of PLASTIC's relevance in understanding heliospheric phenomena are given in the next section.

2.2 Scientific Objectives

2.2.1 Solar Processes and Solar Wind Studies

Properties of the solar wind are of great interest for understanding coronal physics. For example, the charge state composition is determined in the low solar atmosphere and therefore can be understood as a "DNA sample" of the corona. The charge state distributions of different elements can be related (via models) to electron temperature, electron density and ion velocity profiles on the sun.

Additionally, STEREO PLASTIC measures all major solar wind ions under all conditions and thus, can improve our understanding of the slow and fast solar wind.

2.2.2 Interplanetary Manifestations of Coronal Mass Ejections (ICMEs)

It is believed, that CMEs originate from the low corona or chromosphere, thus carrying information of closed magnetic topologies, that can be observed by IMPACT. In combination with composition, charge state and spectra of heavy ions, one can link solar wind properties directly to the CME initiation process on the sun.

Another scientific objective of PLASTIC is to follow the evolution of ICMEs from the sun to 1 AU. Together with ACE (Advanced Composition Explorer) and WIND a three point measurement can be done. The wide separation then allows an investigation of the spatial structure and coherence lengths of ICMEs parameters over longitudinal separation of tens of degrees.

2.2.3 Injection and Acceleration of Ions at CME-Driven Shocks

Together with IMPACT, PLASTIC covers an energy range of $\sim 0.3\text{keV}$ up to $\sim 100\text{MeV}$. With PLASTIC's ability to measure composition and charge state distributions of heavy ions, this instrument package is suited to study the 3-dimensional evolution of suprathermal and energetic particles into the heliosphere, where PLASTIC covers the injection

and standard power law of stationary planar shock acceleration, while IMPACT SEPT covers the signatures of ions escaping the shock.

2.2.4 Heliospheric Studies

In addition to the main mission objectives, PLASTIC will help to understand numerous heliospheric phenomena.

- Stream Interaction Regions and Heliospheric Current Sheet
- Particle Acceleration at Corotating Interaction Regions
- Pick-up Ions
- Space Weather

2.3 Instrument Description

PLASTIC is subdivided into three main components: The ESEA (Entrance System / Energy Analyzer), TOF/E (Time-Of-Flight / Energy) chamber and the Ebox (Electronics Box). Particles enter the ESEA through different instrument sections. Those sections span a wide angular range for particles to enter the instrument, most commonly through the Solar Wind Sector (SWS), which is centered on the sun-instrument line, and consists of a Main channel and a Small channel. The two remaining sections are the Wide Angle Partition with and without a subsequent residual energy measurement (WAPSSD and WAPNOSSD respectively). They cover a total field of view of 225° (STEREO A) and 210° (STEREO B) in the ecliptic.

After passing the Entrance System, particles enter the ElectroStatic Analyzer (ESA), where they are filtered by their energy per charge ratio($\frac{E}{q}$), providing the first of three measurements needed for particle characterization. After that, ions are post-accelerated and enter the TOF/E chamber, where the time of flight τ as well as the residual energy E_{SSD} of a particle is measured.

With $\frac{E}{q}$, τ and E_{SSD} , it is possible to derive velocity, mass and charge state of incident particles. This allows for a characterization of ions leading to two sets of different data-products: Pulse Height Analysis (PHA) data and Matrix rates. The following sections will discuss the main components and different sets of data in detail. A photograph of the instrument is shown in figure 2.1.

2.3.1 Entrance System / Energy Analyzer

PLASTIC measures both solar wind and suprathermal ion distributions, spanning a wide range of ion fluxes. By segmenting the Entrance System into four apertures with different geometry factors, PLASTIC can measure solar wind protons and alphas (SWS - Small channel), solar wind heavy ions (SWS - Main channel), and different types of suprathermal ion distributions (WAPSSD and WAPNOSSD) within one instrument. A schematic of the Entrance System is shown in figure 2.2 from the top and in figure 2.3 from the side.

Figure 2.1:

Photograph of PLASTIC Flight Model, consisting of three main components: The **Entrance System** (golden, dome-like component) is divided into four different sections, Solar Wind Sector - Main channel, Solar Wind Sector - Small channel, Wide Angle Partition SSD and Wide Angle Partition NOSSD. The **TOF/E chamber** (black cylindrical center section) contains both time of flight and energy measurement equipment, while the **Electronic Box** comprises high voltage supplies and various electronics. The picture is taken from *Galvin et al. [2007]*.

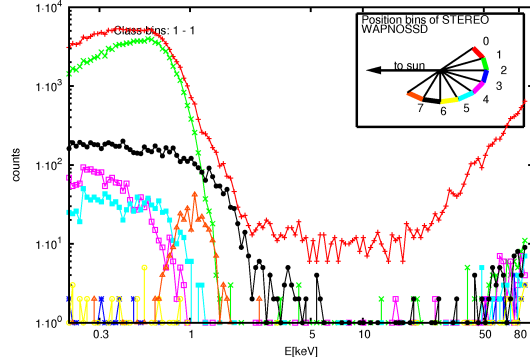
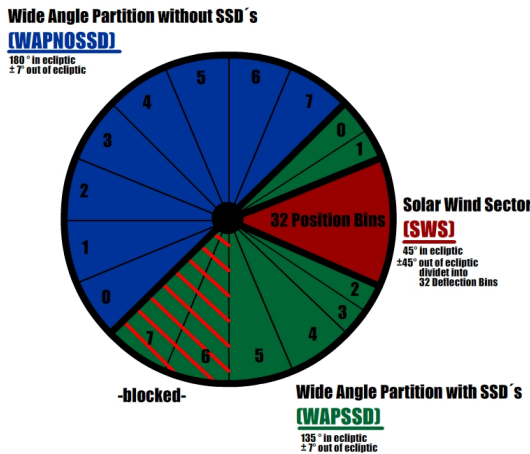
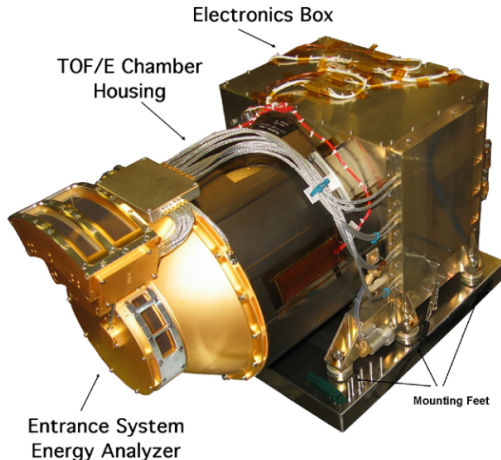


Figure 2.2: Left panel: The Entrance System is divided into three subsystems. The **Solar Wind Sector** (red) is centered on the instrument-sun line. It is accessible for incident particles in an angular range of -22.5° to $+22.5^\circ$ in the ecliptic and -20° to $+20^\circ$ out of the ecliptic, providing a sufficient spatial resolution by 32 resistive anodes (azimuthal direction) and 32 deflection bins (polar direction). The **WAPSSD** section (green) covers 135° field of view in the ecliptic plain and $<10^\circ$ in polar direction, where 45° of the section is blocked by IMPACT. The remaining sector **WAPNOSSD** (blue) spans a field of view of 180° and $<10^\circ$ in polar direction. Both WAPSSD and WAPNOSSD feature eight discrete anodes, which allow for a distinction of different inflow directions. Right panel: This figure shows energy spectra of WAPNOSSD Matrix rates accumulated over three days. The line colors correspond to the legend at the top right and stand for different position bins in this instrument section. Spectral shapes evidently depend on the inflow direction.

Wide Angle Partition

The Wide Angle Partition has a larger geometric factor than either of the two SWS channels and is therefore suited to measure the less abundant suprathermal ions. The Wide Angle Partition is subdivided into the two sections WAPSSD and WAPNOSSD, both covering a 135° or rather 180° field of view in the ecliptic and ±7° in polar direction. The main difference between WAPSSD and WAPNOSSD is a following residual energy measurement, which is only performed in WAPSSD.

Solar Wind Sector

The Solar Wind sector provides a 45° field of view in the azimuthal and ± 20° in elevation direction. It is divided into two entrance apertures, called Main channel and Small channel, to account for the measured ion composition, which consists of 96% protons, 3.9% alpha particles and less than 0.1% heavy ions with $Z > 2$ (solar wind composition). The most abundant heavy ion is O⁶⁺, which still is 2000 times less abundant than protons. A statistically relevant flux of minor ions can only be achieved by a big geometry factor of the entrance system. To prevent the Solid State Detectors (SSD) and Micro Channel Plates (MCPs) from aging, the flux of the more abundant ions, like protons and alphas, must be reduced, which is achieved by a small geometry factor. To combine both measurements, PLASTIC makes use of two entrance slits:

- *Main - Channel*: big geometry factor ($\sim 3 \cdot 10^{-3} \text{ cm}^2 \text{ eV/eV sr}$)
suited for measurements of the elemental composition, ionic charge state distribution and bulk and thermal speeds of solar wind heavy ions (e.g. C, O, Mg, Si, Fe).
- *Small - Channel*: small geometry factor ($\sim 6 \cdot 10^{-7} \text{ cm}^2 \text{ eV/eV sr}$)
suited for measurements of the distribution functions of the more abundant solar wind ions (H⁺, He²⁺), providing proton density, temperature and velocity.

To determine which channel is best to be active, PLASTIC makes use of a following ElectroStatic Analyzer (ESA), that filters incident particles by their $\frac{E}{q}$ -ratio. One can assume a constant bulk velocity for all solar wind ions with a small aberration of ± V_A (Alfven velocity). Thus, an E/q -filter in combination with a constant bulk velocity results in a mass-per-charge m/q -filter, using $\frac{E}{q} = \frac{1}{2q}mv^2$. This $\frac{m}{q}$ -filter can be used to distinguish solar wind protons and alphas (with $m/q < 2$) with a bulk velocity of v_{SW} from the remaining solar wind composition by ESA step. The less abundant heavy ions are collected first in the initial part of the ESA stepping cycle by enabling the Main channel aperture. When the monitored ion flux reaches a critical value on a specific ESA step, which usually marks the beginning of protons and alphas to enter the instrument, the IDPU switches to the Small channel aperture for the remaining ESA cycle.

To provide spatial information on the incoming particles, the azimuthal angle is reported by a resistive anode position detector. It can distinguish between 32 different directions in the ecliptic.

Solar Wind Sector - Deflection System

Spatial resolution in polar direction is realized by a combination of polar deflectors and the ESA. A total set of 32 different voltage steps can be applied to a pair of deflector

electrodes. These, so called, Deflection Steps are swept through in a time interval of 435 ms, 12.8 ms per Deflection Step, and filter incoming particles of constant $\frac{m}{q}$ -ratio by polar direction. In combination with the Electrostatic Analyzer, this results in particles coming from one discrete polar direction per Deflection Step with a polar angle acceptance of 0.4° and 2° FWHM (Full width at half maximum).

Electrostatic Analyzer

After passing the Entrance System, ions enter the Electrostatic Analyzer, a pair of toroidal domes cylindrically symmetric around the instrument's azimuth, which allow both solar wind and suprathermal ions to enter the ESA simultaneously. By applying 128 different voltages to the inner and outer dome of the top hat, incoming ions are filtered by 128 different energy-per-charge ratios with an $\Delta \frac{E}{q} = 6\%$ in a range of 0.3 keV/e to 80keV/e. For every ESA step, all 32 Deflection Steps are swept through, resulting in a minimal time resolution of ~ 1 minute. The voltages of the deflectors are matched to each ESA voltage in order to collect incident ions up to $\pm 20^\circ$. The nominal energy-per-charge response of the ESA is given by

$$\frac{E}{q} [\text{keV}/e] = 0.2 \cdot 1.04895^{(127-ESA)}. \quad (2.1)$$

For a detailed discussion on the Entrance System and pre-flight calibration of the ESEA see *Karrer [2007]*. Before entering the TOF chamber ions are post-accelerated by a constant voltage drop of about 20 kV, that can be changed by command. This post-acceleration assures low-energy particles to exceed the threshold of the solid state detectors.

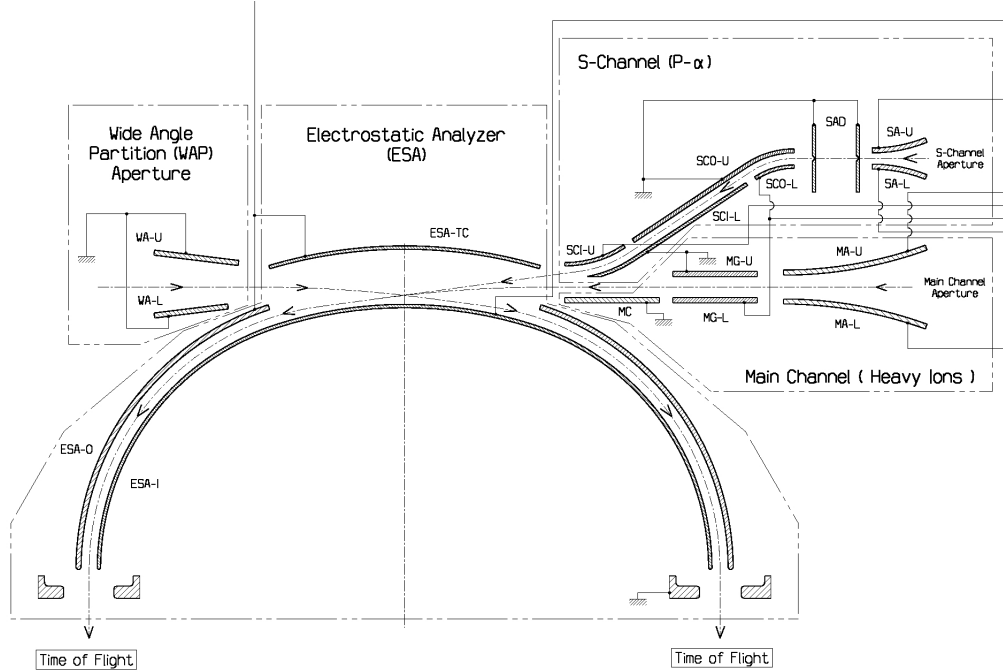


Figure 2.3: A schematic view of the Entrance System is shown. Ions enter the instrument from the right (Main/Small channel Aperture) or from the left through the Wide Angle Partition Aperture. In the Solar Wind section the polar deflectors SA-U, SA-L, MA-U, MA-L are ramped through in 32 different deflection voltages, selecting ions by their out-of-ecliptic angle. As only one channel is active at the time, channels can be disabled by the electrodes MA-U, MA-L, SCO-L, SCI-U. Channel switching is based upon a monitored count rate. The less-abundant heavy ions are collected first in the initial part of the ESA stepping cycle by enabling the Main channel aperture. When the ion flux reaches a critical value on a specific ESA step, which usually marks the beginning of protons/alphas to enter the instrument, the IDPU switches to the Small channel with a much smaller geometry factor for the rest of the ESA cycle. Ions are then filtered by the their energy-per-charge ratio with an electrode pair of toroidal domes that are used as an electrostatic analyzer (ESA-0, ESA-1). Both voltages are swept through to a total set of 128 different, logarithmic spaced values to cover the full $\frac{E}{q}$ -range from $\sim 0.3\text{keV}$ to $80\text{keV}/e$. For each of the ESA voltages the Deflection voltages are stepped through with an accumulation time of 12.8 ms each, which results in a total time of 60 seconds per cycle. This picture is taken from *Galvin et al.* [2007].

2.3.2 Time of Flight / Energy Chamber

Time of Flight

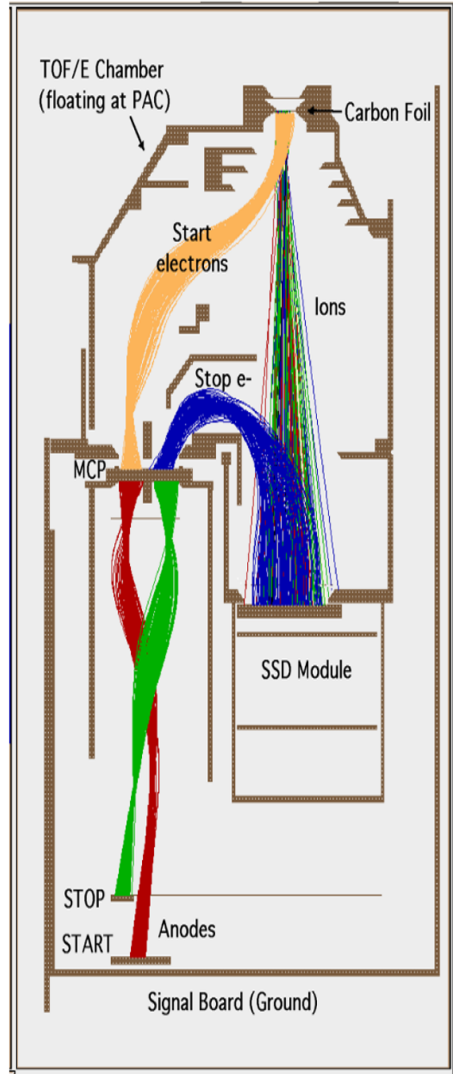


Figure 2.4: Ion and electron trajectories from a SIMION 3D simulation for the TOF/E chamber on the Solar Wind Sector. This picture is taken from Galvin *et al.* [2007]

Particles enter the Time-Of-Flight (TOF) Section by passing through a $3.5\mu\text{g}/\text{cm}^2$ thin Carbon foil, emitting secondary electrons. These electrons are guided by a system of electrodes to a MCP (Micro Channel Plate), where they trigger the "START" signal of the time-of-flight measurement. After penetrating the carbon foil ions will then travel the distance of 8 cm to the SSDs (SWS and WAPSSD) or alternatively the distance of 5.8 cm directly to the MCP (WAP-NOSSD). Ions hitting the SSD will produce secondary electrons, that will be steered by a pair of electrodes to the MCP, triggering the "STOP" signal of the TOF measurement. The time-of-flight is binned into 1024 TOF channels, ranging from 4ns to 250ns. The maximum time resolution is $\sim 2\text{ns}$, it is affected by the angular spread and energy straggling of the ions' carbon foil passage. Because of its complex design the TOF/E chamber has undergone a detailed analysis and calibration phase, fully described in Allegrini [2007]. Chamber dimensions and applied electrode voltages were designed, using the electrostatic ion optics analysis and design program SIMION 3D, that calculates ion and electron trajectories for a user specified particle distribution (here, solar wind). Figure 2.4 shows such a simulation, where particles enter the TOF/E chamber and produce secondary electrons, that are steered by a system of steering electrodes. The target efficiency for hitting either the SSD or MCP was estimated to be greater than 92%. The total efficiency for measuring a particular ion is affected by three separate contributions, which are the efficiency for getting a "START" signal, "STOP" signal and a "VALID" signal. A non-sufficient total efficiency can cause various "misleading" effects on the data (especially the PHA data), which are described in chapter 2.5.

Residual Energy

To measure the energy of incoming ions, sixteen Solid State Detector (SSD) pixels are located at the end of the time-of-flight path in the Solar Wind and WAPSSD sectors. They are custom-made Canberra Passivated Implanted Planar Silicon (PIPS) detectors with an equivalent entrance window of 25nm silicon. Energies are measured within a range of 15keV to 2000keV and converted into 1024 channels. The SSDs not only measure the residual energy of incident particles, but also trigger the "STOP" signal for the time-of-flight measurement.

The calibration of the solid state detectors, including information on the energy response function, is described in *Blush et al.* [2005].

2.3.3 Measurement Procedure

One scientific goal of the PLASTIC instrument is the distinction of different solar wind ions. It is realized with the three measurements of E_{res} , $\frac{E}{q}$ and τ described in 2.3.1 and 2.3.2. These three values are adequate to fully characterize incoming ions by their mass m , charge q and velocity v ,

$$m = \frac{2}{\beta(E, m)} E_{res} \left(\frac{\tau}{d} \right)^2 \quad (2.2)$$

$$\frac{m}{q} = 2(E/e + V_{PAC}) \alpha(E, m) \left(\frac{\tau}{d} \right)^2 \quad (2.3)$$

$$v = \sqrt{2 \frac{E/e}{m} q}, \quad (2.4)$$

where d is the flight path in the TOF section and V_{PAC} the post acceleration voltage. $\alpha(E, m)$ denotes the species dependent energy loss in the carbon foil, while $\beta(E, m)$ denotes the pulse height defect in the solid state detector (see appendix A.3). Both functions were determined in pre-flight calibrations and simulations.

Hence, the equations above allow us to assign an ion species to each measured event with uncertainties caused by the errors $\Delta E/q$, $\Delta \tau$ and ΔE_{res} . Important factors influencing the quality of species classification are:

- Resolution of time of flight measurement τ
- Resolution of residual energy measurement E_{SSD}
- Resolution of ESA measurement $\frac{E}{q}$
- Knowledge of energy loss in carbon foil $\alpha(E, m)$
- Knowledge of pulse height defect in SSD $\beta(E, m)$

Following sections of this diploma thesis will discuss the influence of these factors in more detail.

2.4 Pulse Height Analysis Words

From the time-of-flight, residual energy and energy-per-charge measurement PLASTIC generates three different types of data products. The PHA words (1) contain all obtained information on incident particles. These are directly sent to the classifier board for further analysis. In addition, PLASTIC computes several, so called, Matrix Rates (2) from the raw PHA data within a specific time interval, that are directly fed into the IDPU together with Housekeeping and Status information (3). In this work we heavily focus on analysis of PHA words. Other data products are described in *Kistler and Ellis [2007]* and *Galvin et al. [2007]*.

Every incident ion that satisfies the event selection logic conditions is assigned to a 48-bit pulse height analysis word, which consists of the following set of informations.

- *ESA* (0 - 127)

ESA steps are connected to the $\frac{E}{q}$ -ratio of incident particles determined by the Electrostatic Analyzer via equation 2.1. They translate into logarithmically spaced energy-per-charge ratios, that can be used to derive velocities of particles with known charge. The lowest ESA step is linked to the highest possible E/q ratio of $\sim 80\text{keV}$.

- *SWPD* (0 - 31)

Deflection steps contain information on the polar direction of ions entering the Solar Wind Sector. The full range of $\pm 20^\circ$ is divided into 32 SWPD bins, where SWPD=15 translates into a polar direction of about 0° . Every event measured within the WAP section, that does not provide any polar angle resolution, is assigned to SWPD=0.

- *QUADRANT* (0 - 3)

The instrument is divided into four 90° quadrants.

- *SSDE* (0 - 1023)

SSDE is connected to the residual energy E_{SSD} of particles, which is measured by a solid state detector. The conversion from SSDE to E_{SSD} is dependent on the SSD pixel hit, but still can be approximated with a nominal gain of 2keV per channel. An accurate conversion from channel number to energy for each SSD pixel is presented in A.1.

- *SSDID* (0 - 15)

The SSDID denotes which pixel of the solid state detectors is triggered. This information is crucial for an accurate transformation from SSDE channel to residual energy.

- *TOF* (0 - 1023)

With TOF channel information one can derive the time-of-flight of incident particles using a nominal gain of 0.25 ns per channel. This results in a maximum measurable τ of about 250 ns. We have to point out, that the data seem to be shifted in TOF with up to five nano seconds, which has to be considered for deriving τ .

- *POS* (0 - 63)

Position bins describe the azimuthal angle of incident particles. There is a total of

32 position bins in SWS and eight in WAPSSD and WAPNOSSD each. (See Fig.: 2.2)

- *SECTION* (0 - 3)

This describes, which section of the instrument was triggered (SW - Main 0, SW - Small 1, WAPSSD 2, WAPNOSSD 3).

- *PRIORITY* (0 - 3)

The Priority bin is based upon an event classification. Every incident particle is assigned to a priority bin, which is determined by a particle's m and m/q . Due to the limited telemetry of the instrument only a sample of 768 measured PHA words per instrument cycle can be sent to Earth. This sample is chosen by an event's priority bin and assures the collection of a representative part of the data, but still emphasizes the importance of heavy ion data in respect to the more abundant proton events.

Pulse height analysis words provide the most detailed information on incident particles available, but also have the disadvantage of containing only a fraction of all measured events. For each ESA step a sample of 512 PHA is collected, which is already sorted by priority. This sample then contains of

- 32 PHA WAP Priority 0 (H^+, He^{2+})
- 32 PHA WAP Priority 1 (Heavy ions)
- 64 PHA SWS Priority 0 (H^+)
- 64 PHA SWS Priority 1 (He^{2+})
- 160 PHA SWS Priority 2 (Heavy ions)
- 160 PHA SWS Priority 3 (Heavy ions)

adding to a total of 65536 events per ESA cycle (1 min). These events are used for calculations of PLASTIC's various Matrix rates described in *Galvin et al.* [2007], which are then sent to earth. The limited telemetry allocation of 3 Kb/s then only allows for 768 PHA words per minute to be transmitted.

An illustration of how these 768 pulse height analysis words are sampled is presented in figure 2.5. The data is collected by the DPU on every second ESA step, resulting in 12 possible PHA words per ESA divided into 8 SWS and 4 WAP events. To obtain events from all ESA steps, the DPU alternates between starting a cycle on ESA 0 and ESA 1. For every step the DPU buffer is then filled with twelve PHA words from the front, until the maximum buffer size of 768·48 bit is reached. If there are not enough events to fill the complete buffer, additional PHA words can be saved into the buffer from the back with a focus on low ESAs. Hence, the explained method of data accumulation is strongly biased towards heavy ion events on low ESA steps, which has to be taken into account for data analysis. Although this weighting on heavy ions is intended, one needs to correct this effect to emphasize the real solar wind ion abundances. In section 2.5 we present our algorithm for accumulating PHA words, which also covers the details of PHA normalization.

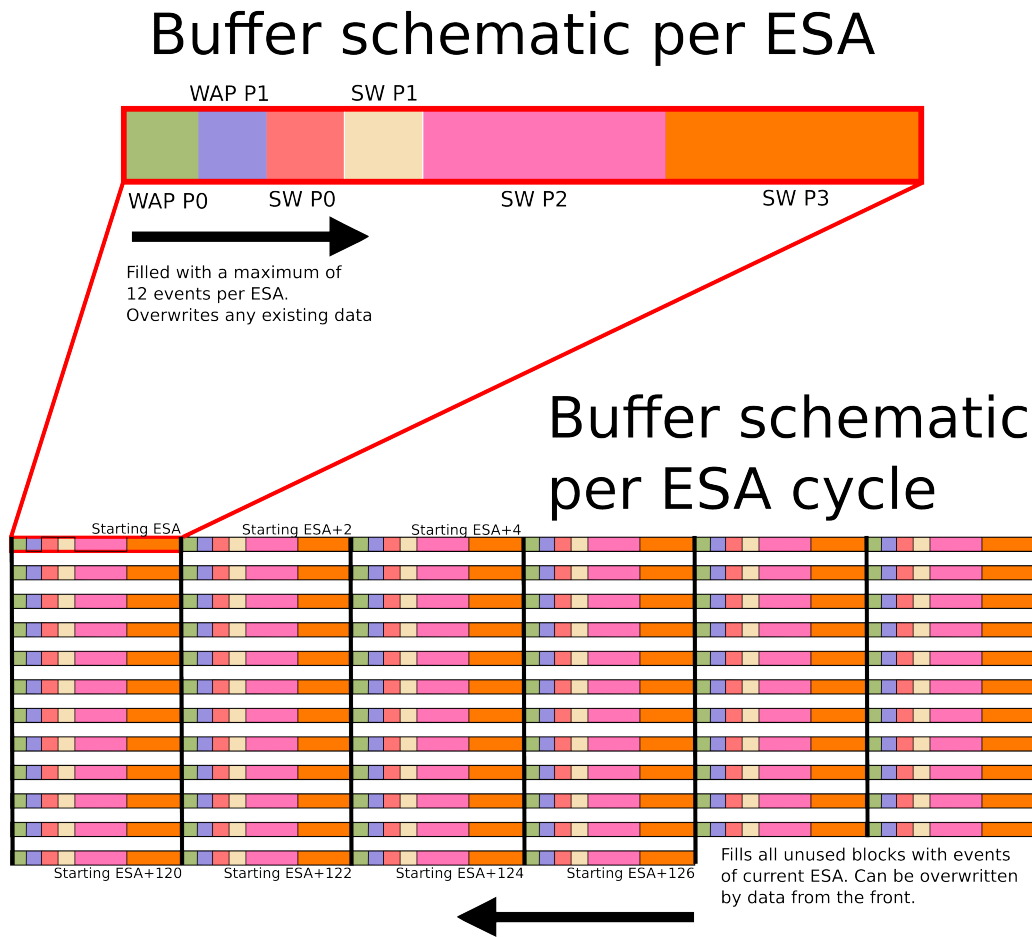


Figure 2.5: This is an illustration of PLASTICs DPU buffer. Each second ESA step it is filled from the front with a maximum of 12 events, leading to a total buffer size of 768·48 bit. These 12 available data blocks are reserved for the different priorities of WAP and SWS and will overwrite any existing data when filled. The preset number of data blocks for each priority allows for an emphasis of the importance of heavy ions. Nevertheless, by reserving a good portion of the buffer for the less abundant heavy ions, it could happen, that blocks of high priority end up unused. To prevent this, the 12 reserved blocks of each ESA always begin after the last written block of the previous ESA step. Additionally, the buffer is simultaneously filled from the back, but without the allowance to overwrite existing data. Thus, at the end of an ESA cycle, the buffer contains as many reserved priority events as possible, while the remaining blocks are filled with events from the back with an emphasis on low ESA steps. The starting ESA step of each cycle alternates between zero and one, in order to get events from every ESA step [Kistler and Ellis, 2007].

2.5 ET Matrix

2.5.1 Overview

PHA data of PLASTIC comes in form of lists, which are saved in ASCII (American Standard Code for Information Interchange) or CDF (Common Data Format) format. They are provided by the University of New Hampshire for each day of the mission and contain 768 PHA words for every one-minute ESA cycle, adding up to a total of over 1.1 million events per day (without consideration of data gaps). Every event is linked to a corresponding timestamp with a maximum resolution of one minute, an error flag preventing use of corrupted data, and channel switch number, which corresponds to the current cycle's ESA step of channel switching. With this information we are able to produce, so called, ET matrices, which accumulate corresponding counts for each SSD, TOF, and ESA bin. They are our initial point of data analysis.

2.5.2 Data Accumulation

For our investigation of suprathermal ions with STEREO PLASTIC, we developed a python tool, which is able to derive numerous physical quantities from PHA data. As mentioned before, most of our data analysis begins with the analysis of the, so called, ET matrices, which are a representation of PLASTIC's PHA data. There is a total of 128 ET matrices, one for each ESA step of the instrument, which consist of 1024 x 1024 (TOF x SSD) possible coordinates.

Each measured event is linked to a corresponding SSD, TOF, and ESA channel, which depend on an event's energy and species. It is assigned to an ET matrix corresponding to its ESA channel and coordinate, which is determined by the SSD and TOF channel. By accumulating PHA data over long periods, the ET matrices are gradually filled with events, whereas the number in ET matrix x at position (y,z) denotes the amount of measured events on ESA step x , TOF channel y and SSD channel z . The channel numbers can be converted into their respective residual energy, time-of-flight, and energy-per-charge value by equations A.6, A.3, 2.1 on pages 74, 73, 15.

Our program is capable of creating long-term ET matrices, which are useful for in-flight calibration of the instrument (see chapter A.3), and short-term ET matrices, used for calculation of energy spectra within short periods (see chapter 2.5.4). The time resolution of our short-term ET matrices is limited to five minutes, because of the necessity of PHA normalization, which accounts for the priority based weighting of PHA data. It can only be done for maximum of five minutes samples of PHA data, as it depends on various rate products, which are provided with a maximum time resolution of 5 minutes. Additionally, SWS, WAPSSD, and WAPNOSSD require a separate data treatment, due to different geometry factors, Field of Views (FOV) and numerous other parameters, which depend on the instrument section.

Our program creates ET matrices by passing the desired parameters, i.e. timespan, time resolution, section of the instrument, etc., and is also able to filter events by SSDID, SWPD, POS, and Priority (explained in chapter 2.4). Our python tool is able to derive energy and composition spectra from the obtained ET matrices, which are used to calculate further physical quantities (see chapter 2.5.4).

The following simplified python source code describes the details of data accumulation and PHA normalization.

```

1
2 """Defining input parameters"""
3
4 #Start date of data accumulation
5 year,month,day=2007,2,1
6
7 #duration of data acc. in day
8 timespan=700
9
10 #spacecraft ("A" or "B")
11 stereo="A"
12
13 #Section of the instrument [0:SWS-MAIN,1:SWS-SMALL,2:WAPSSD,3:WAPNOSSD]
14 ip_section=2
15
16 #Deflection step
17 ip_defl=0
18
19 #SSD pixel id
20 ip_ssdid=0
21
22 #Priority
23 ip_priority=0
24
25 (...)

26
27
28 """Creating two empty ET matrices"""
29 #These matrices are filled when looping through PHA words, where
30 #et_array_longterm contains counts of the whole period,
31 #while et_array_tmp only contains counts for a five minute
32 #interval
33
34 et_array_longterm=zeros((128,1024,1024))
35 et_array_tmp=zeros((128,1024,1024))
36
37 """Loop through pha files in time period"""
38 for curr_day in range(timespan):
39
40     """ Creating normalization array (baserate weighting)"""
41     # First the baserates are loaded, which contain number of saved PHA
42     #word events of the current day in each ESA, section, priority and
43     #5min bin of the day. Next the priority rates are loaded, which
44     #contain number of measured events of the instrument in each ESA,
45     #section, priority and 5min bin of the day. In order to account for
46     #the biased PHA event selection, we then create a normalization
47     #array, containing the priorityrate/baserate value for each bin,
48     # which corresponds to a mean number of events in each bin per saved
49     #PHA word. Applying this value to each PHA event instead of a simple
50     #event count, leads to normalized data.
51
52 baserates      = load_baserates(year,month,day,curr_day,stereo)
53 priorityrates = load_priorityrates(year,month,day,curr_day,stereo)
54 norm_calc=lambda x,y: x/y
55 norm_counts=map(norm_calc,priorityrates/baserates)
56
57 #Creating filename of PHA file for the current date
58 current_file = create_filename(year,month,day,curr_day,stereo)

```

```

59
60     #Opening corresponding PHA file
61     pha_file = open(current_file, "r")
62
63     #Setting current 5min interval of day
64     5min_of_day_last=0
65
66     """Reading through PHA words of current file"""
67     for pha_words in pha_file:
68         pha_word = pha_words.split()
69         TIME      = pha_word[1]
70         ESA       = pha_word[2]
71         TOF       = pha_word[7]
72         SSD       = pha_word[6]
73         section   = pha_word[9]
74         deflection = pha_word[4]
75         priority   = pha_word[10]
76         ssd_id    = pha_word[5]
77
78     #Deriving 5min bin of current day:
79     5min_of_day=create_5min_bin(TIME)
80
81     """Filtering pha words by input parameters """
82     if section,defl,ssdid,priority,(...) == ip_section,ip_defl,(...):
83
84         """Adding PHA events to ET matrices"""
85         et_array_longterm[ESA,TOF,SSD]+= norm_counts[ESA,ip_section,5
86             min_of_day]
87         et_array_tmp[ESA,TOF,SSD]+= norm_counts[ESA,ip_section,5min_of_day]
88
89         """Create high resolution data from et_array_tmp"""
90         if 5min_of_day != 5min_of_day_last:
91             # Every 5min bin et_array_tmp is passed to the function
92             # data_analysis, which could be any routine computing further
93             # data products of 5min resolution data.
94             data_analysis(et_array_tmp)
95             # et_array_tmp is reseted for next 5min bin
96             et_array_tmp[:, :, :] = 0
97             5min_of_day_last=5min_of_day
98     pha_file.close()

```

Listing 2.1: Data accumulation of PHA data with python.

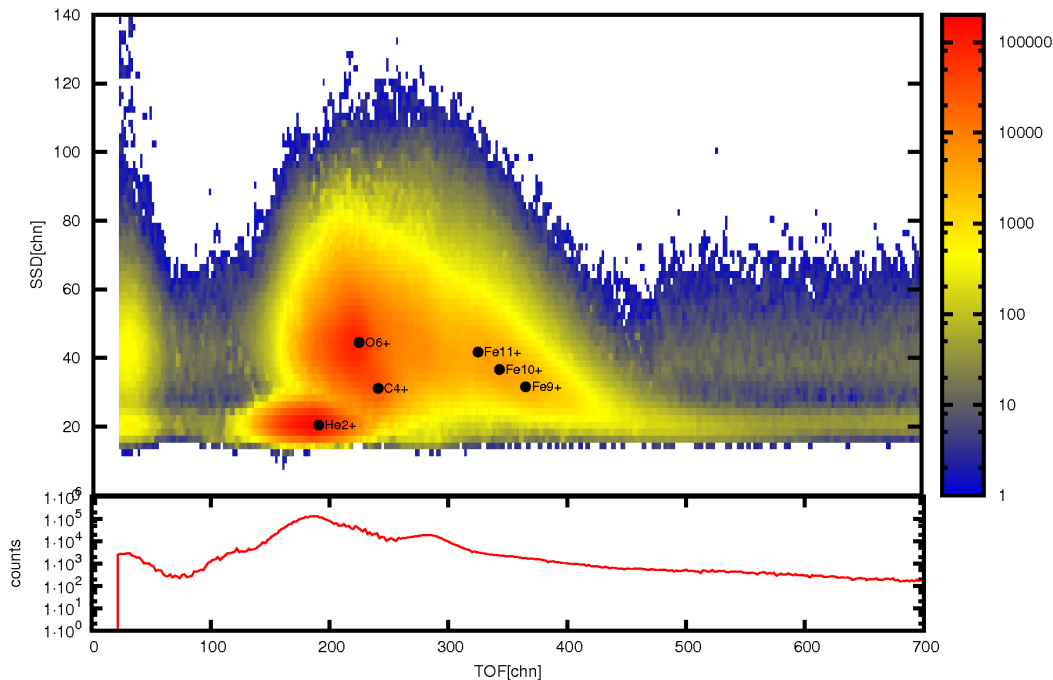


Figure 2.6: The upper panel shows an exemplary ET matrix for STEREO A - SWS - ESA step 57. Counts were accumulated in a period of 700 days beginning in February, 2007. The x- and y-axis show TOF and SSD channel. Number of counts in each TOF/SSD bin are color coded. The lower panel shows double coincidences for the given time-of-flight range. The theoretical positions of $\text{Fe}^{(11-9)+}$, C^{4+} , O^{6+} and He^{2+} in the upper panel were calculated by our algorithm, described in A.3.

2.5.3 Interpretation

In figure 2.6 we present the resulting long-term ET matrix of our accumulation algorithm for ESA step 57 in a period of 700 days. The top panel shows triple coincidence counts, which are events, that triggered a time-of-flight and residual energy signal. The bottom panel shows PHA events, that did not trigger a residual energy signal, so called double coincidences. Ions of specific mass and mass-per-charge occur in the ET matrix according to their time-of-flight and residual energy given by equations 2.2, 2.3, and 2.4., whereas the finite measurement accuracy causes uncertainties in TOF and SSD bins.

Thus, ions do not appear as sharp peaks, but rather as two dimensional gaussian or kappa distributions with a characteristic width in TOF and SSD. The center of density of these distributions marks the mean position of an ion in the ET matrix and is used to identify its species. The SSD and TOF positions will change in dependence of the ESA step, which is illustrated in figure A.3 on page 77. One can see how the ion distributions wander to lower SSD and higher TOF bins with increasing ESA steps. The SSD and TOF position of these ion sequences were calculated with equations A.2 and A.7 (described in chapter A.3). Events, which appear on low ESA steps, correspond to events of high energy per charge ratios and thus are most likely suprathermal particles, while ET matrices of high ESA steps will contain ions of low energy-per-charge.

In figure 2.6 the SSD and TOF position of six typical solar wind ions, i. e. He^{2+} , O^{6+} , C^{4+} , Fe^{9+} , Fe^{10+} , Fe^{11+} , is shown together with our long-term data for ESA step 57. Although, each ion is assigned to a unique position in the ET matrix corresponding to its mass and mass-per-charge, the characteristic width of its distribution can cause overlap with adjacent ions. For most ions, this overlap plays an important role, as contributions of adjacent ion distributions have to be taken into account for further data analysis. Nevertheless, some ions, i. e. He^{2+} , He^+ , H^+ , O^+ , C^+ , Ne^+ , are mostly not affected by contributions of adjacent ions and thus, allow an easier approach for data analysis. Two possible approaches of calculating further physical quantities from the obtained ET matrices are described in chapter 2.5.4.

In figure 2.6 one can see a cut-off at low SSD bins. This cut-off is due to a commandable offset for each of the SSD pixels to prevent the SSDs from causing too much noise in the data. Events with an energy signal below this offset, will be assigned to SSD channel zero, illustrated in the bottom panel of figure 2.6. This offset has undergone several changes since the beginning of the mission and therefore, does not produce a sharp cutoff in our long-term ET matrices. As mentioned before, peak distribution will wander to lower SSD channel with raising ESA steps. Thus, the ratio of double- to triple coincidences will also increase with increasing ESA steps. As a consequence, the calculation of an event's mass by equation 2.2 can only be done for a fraction of ions on high ESA steps. Additionally, the background of double coincidence counts in time-of-flight is higher as for triple coincidence counts, thus the calculation of an event's mass-per-charge on high ESA steps is also affected. The higher background is caused by solar wind protons, which are most prominent on high ESA steps and often trigger an invalid time-of-flight signal.

Similar to the SSD cut-off, the comandable cut-off at low TOF bins is also apparent in our long-term ET matrix. It suppresses PHA words without a valid time-of-flight signal. An invalid TOF signal could be caused by an ion x penetrating the carbon foil and triggering the "START" signal of the time-of-flight measurement. Ion y , which has already passed the carbon foil without a related "START" signal, then could trigger a "STOP" signal, which would be attributed to ion x . As a result, a truncated time-of-flight signal would be assigned to ion x , that has no physical relevance.

Furthermore, two additional effects, so called, energy and time-of-flight pile ups can cause invalid SSD and TOF signals. The time-of-flight pile up causes a slowly decaying background with increasing time-of-flights. It is most pronounced in an SSD range, that corresponds to an energy of O^{6+} and He^{2+} (the dominant species in our ET matrices), centered on SDD channel 40 and 20 in figure 2.6. The time-of-flight pile up can occur if ion x triggers a "START" signal without a related "STOP" signal. After that, an ion y , which has not triggered a "START" signal on its carbon foil passage, triggers a "STOP" signal, which would be related to ion x . Thus, the resulting time-of-flight of ion x would be extended.

The energy pile up on the other hand causes an increased energy signal of incident ions. It is most pronounced on high ESA steps in the time-of-flight range of protons and therefore, is not visible in figure 2.6. It is caused by two (or more) particles entering the TOF chamber almost simultaneously. Due to the electronic's dead time, only one particle is able to trigger a valid time-of-flight signal. However, both particles will deposit their energy and thus, causing an energy signal, which is twice (or more) as high than the expected one. On high ESA steps, this often results in a mirrored proton distribution,

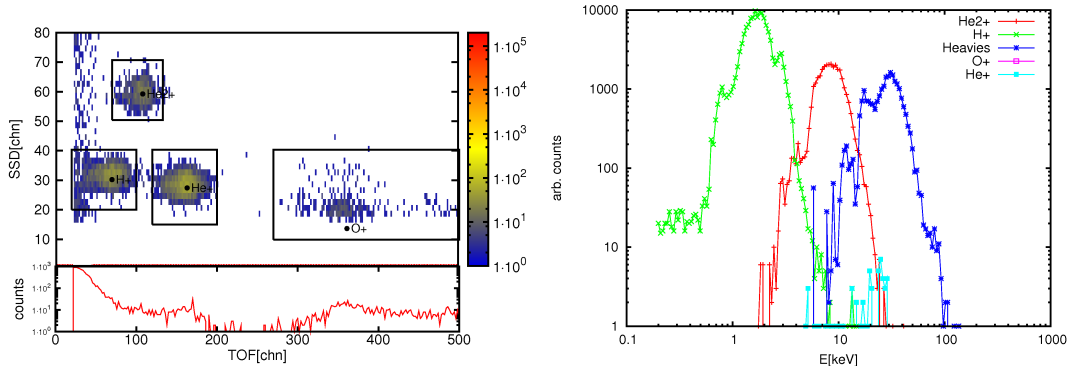


Figure 2.7: The left figure shows an ET matrix on ESA 12 together with our ion boxes, which are used for computing energy spectra. Every PHA event occurring in one of these boxes within a given period is sorted by its energy (derived from an event's ESA) and species, which finally leads to the energy spectra illustrated in the right figure. Here, the spectra of He^+ , He^{2+} , O^+ , H^+ are drawn in a logarithmic scale for WAPSSD in a period of 2 days. The "Heavies" spectrum primarily contains O^{6+} events but is polluted by adjacent ions.

which lies above the original one.

2.5.4 Analysis

In order to derive physical quantities, like ion velocities, densities, and temperatures, from our ET matrices, we need to consider two points.

1. Composition

Currently our ET matrices consist of events of all observed solar wind ions. Thus, we need to find a way to obtain counts of single solar wind ions.

2. Solar wind properties

The ion count rates are used to derive solar wind properties. For that, we have to convert ESA, SSD, and TOF information into physical quantities and address PLASTIC's duty cycle and detection efficiency.

Composition

In the following, we will discuss two analysis techniques, which are able to derive the composition from ET matrices. Both have been developed for the instrument SWICS aboard the ACE and Ulysses spacecraft.

The first one has been developed by *von Steiger et al.* [2000]. Assuming the ion positions in the ET matrices are known, one can put boxes around them and sum up all counts that lie inside. For the case of ions, which are covered by a box without contributions of adjacent ion peaks, the energy spectra can be obtained directly (see figure 2.5.4). In fact, this is the case for the most abundant solar wind ions, i. e. H^+ and He^{2+} , and pick-up ions. Nevertheless, for other solar wind ions, adjacent ion distributions do contribute a significant amount of counts, so called spill-over, to their box-rate. Additionally, the, so

called, probabilistic-rates have to be considered. They denote events of ion x , which do not lie inside its corresponding box with a width of σ . The details of this technique are described in *von Steiger et al.* [2000].

The second analysis technique has been developed by *Berger* [2008]. First, instrumental response functions of all major solar wind ions are determined. This is achieved by a standard Levenberg-Marquard fit to long-term ET matrices. Then, the normalized distribution functions can be used for a simultaneous fit (with the count rate as the only free parameter per ion) of over 80 ions to the short-term ET matrices. As a result, one obtains count rates of each fitted ion in the ET matrices. A detailed description of this technique is presented in *Berger* [2008].

Since we are dealing with C⁺, O⁺, N⁺, Ne⁺ and He⁺ in our analysis of pick-up ions, we use the first step of the analysis technique of *von Steiger et al.* [2000] by defining boxes in our long term ET matrices for H⁺, He⁺, He²⁺, and heavy pick-up ions. These ions have in common, that they are well isolated from the rest of the solar wind composition, thus we are able to define boxes, which cover the complete ion peaks with very small contributions of adjacent ions. The advantage of this approach is, that we do not have to deal with spill-rates, probabilistic- rates, or a simultaneous fit of over 80 ions in our ET matrices. The disadvantage is obviously, that we are confined to a fraction of solar wind ions for our analysis.

An example of our boxes is shown in the left panel of figure 2.7 for H⁺, He²⁺, He⁺ and heavy pick-up ions (labeled O⁺) on ESA step 12. The right panel shows the resulting energy spectra, which were derived from the ion box rates of all possible ESA steps.

Solar wind properties

At this point it is necessary to derive the velocity distribution of our box rates in order to calculate the properties of solar wind ions. From *Berger* [2008] we obtain the velocity distribution

$$f(v_x) = \frac{N(v_x)}{v\tau g\eta(v_x)\Delta v D(\phi, \theta, \beta)}, \quad (2.5)$$

where $D(\phi, \theta, \beta)$ denotes PLASTIC's duty cycle, which is a function of the azimuthal and polar angle of PLASTIC's entrance system and the Mach angle $\beta = \arctan(\frac{v_{th}}{v_{SW}})$. It describes which part of a velocity distribution can be detected by the instrument. Δv is determined by the uncertainty of an ESA step's E/q -ratio, τ is the duration of measurement, g the geometry factor of the active section, v the ion velocity obtained from the instrument's E/q step, $\eta(v_x)$ the detection efficiency and $N(v_x)$ the amount of measured counts.

The parameters g , v , Δv , and τ are known, while $N(v_x)$ can be derived from our box rates. The efficiency $\eta(v_x)$ has to be obtained from in-flight calibrations, which is explained in chapter 3.1.6. Unfortunately, we were not able to derive the detection probability of PLASTIC in the time frame of this thesis, but instead present an ansatz of its calculation in chapter 4.1. The duty cycle $D(\phi, \theta, \beta)$ of the instrument can be simulated by our developed virtual detector, which is briefly described in chapter 4.2. Nevertheless, the missing parameter $\eta(v_x)$ already prevents us from calculating the precise velocity distribution of an ion and thus, we do not have to calculate $D(\phi, \theta, \beta)$ either.

The solar wind parameters, i.e. density n , velocity v and temperature T , can be obtained

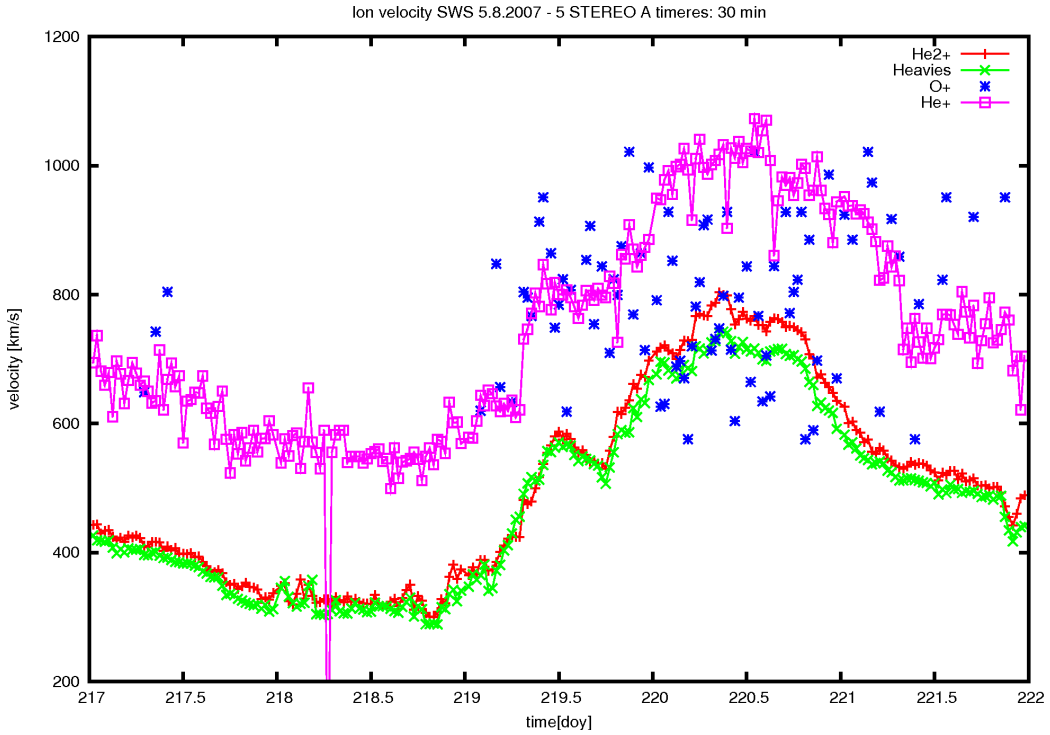


Figure 2.8: The x- and y-axes denote ion velocity in km/s and time in day since 2007. v_{ion} is plotted in a period of five days for He^{2+} , He^+ , O^+ and "Heavies", which mainly consists of O^{6+} . Day 219.4 marks the beginning of a corotating interaction region. One can see, that He^{2+} and O^{6+} have the same velocity with small aberrations. He^+ and O^+ on the other hand seem to have a slightly higher velocity caused by the typical velocity distributions of pick up ions, exceeding up to twice the solar wind speed. We also point out, that the rarity of O^+ leads to distinct uncertainties in the determination of the first moment. This is especially the case in slow solar wind stream, where the O^+ velocity can not be derived most of the time (see doy 217 to 219).

by calculating the moments of a known velocity distribution.

$$\begin{aligned} n_{ion} &= \int_{-\infty}^{\infty} f(v_x)(v_x)^0 dv_x \\ v_{ion} &= \frac{1}{n_{ion}} \int_{-\infty}^{\infty} f(v_x)(v_x)^1 dv_x \\ T_{ion} &= \frac{m}{k_b n_{ion}} \int_{-\infty}^{\infty} f(v_x)(v_x - v_{ion})^2 dv_x \end{aligned}$$

As a first estimate, we calculated the first moment of He^{2+} , He^+ , O^+ and "Heavies" neglecting PLASTIC's duty cycle and assuming a constant efficiency of 100 percent. The resulting ion velocities are shown in figure 2.8. They were derived for SWS in a period of five days with a resolution of 30 minutes.

3 Data Analysis

3.1 Heavy Pick-up Ions with PLASTIC

3.1.1 Overview

Pick-up ions are characterized by their single charge state and their broad velocity distribution, which can exceed up to twice the solar wind velocity. The best investigated pick-up ion so far is He^+ , which is believed to originate from the interstellar medium. It is far more abundant than the heavy pick-up ions with masses greater than four atomic units, due to a lower first ionization potential (FIP) and a higher neutral density in the outer heliosphere. By using the model of *Vasyliunas and Siscoe* [1976] one can derive fluxes of pick-up He_{IS} and O_{IS} at the nose of the heliosphere with $f_{O+} = (6.13 \pm 1.53) \cdot 10^0 \text{ cm}^{-2}\text{s}^{-1}$ and $f_{He+} = (3.06 \pm 0.72) \cdot 10^2 \text{ cm}^{-2}\text{s}^{-1}$ (from *Cummings et al.* [2002]). Due to various effects, calculating theoretical fluxes for these pick-up ions in the inner heliosphere is more difficult. A well known phenomenon for He^+ is an enrichment at about 1 AU, which is caused by gravitational focussing of incident He atoms. This will lead to a cone of enriched He aligned along the inflow direction of the interstellar medium around the sun. This focussing has not yet been discovered for interstellar O^+ and so could alter the expected ratio of He^+/O^+ .

Another important consideration, especially for the heavy pick-up ions, is the occurrence of inner-source pick-up ions. These inner source pick-up ions can emanate from dust grains near the sun, sungrazing comets or planetary atmospheres.

All these effects have to be taken into account when discussing fluxes of pick-up ions in the inner heliosphere. This section will provide an outline of heavy pick-up investigations with PLASTIC.

3.1.2 Data Accumulation

The first step was to accumulate all available heavy pick-up ion data from PLASTIC for a preferably long period, which is necessary to compensate for the rarity of pick-up ions with masses greater than four atomic units. This was done for the SWS of STEREO A in a period of 700 days beginning in February 2007, leading to a total number of about 23000 events. In order to anticipate any loss of information, the data could not just been accumulated in form of a long term ET matrix but has been saved as a list of PHA events with a time resolution of thirty minutes. For every event the list contains information on ESA, TOF, SSD, proton bulk velocity, proton density and time, thus allows to account for varying time-dependent inner sources, e.g. sungrazing comets.

The PHA events were selected by applying a TOF-, SSD-, and ESA-filter, which translates into a box-like filtering of the ET matrices. This is possible due to the high mass-per-charge ratios of incident heavy pick-up ions, resulting in a long time-of-flight in contrast to ions with higher charge states. An example of these heavy pick-up boxes is shown in figure 3.1 for ESA 7, where ESA 27 is the lowest E/q -ratio (and highest ESA

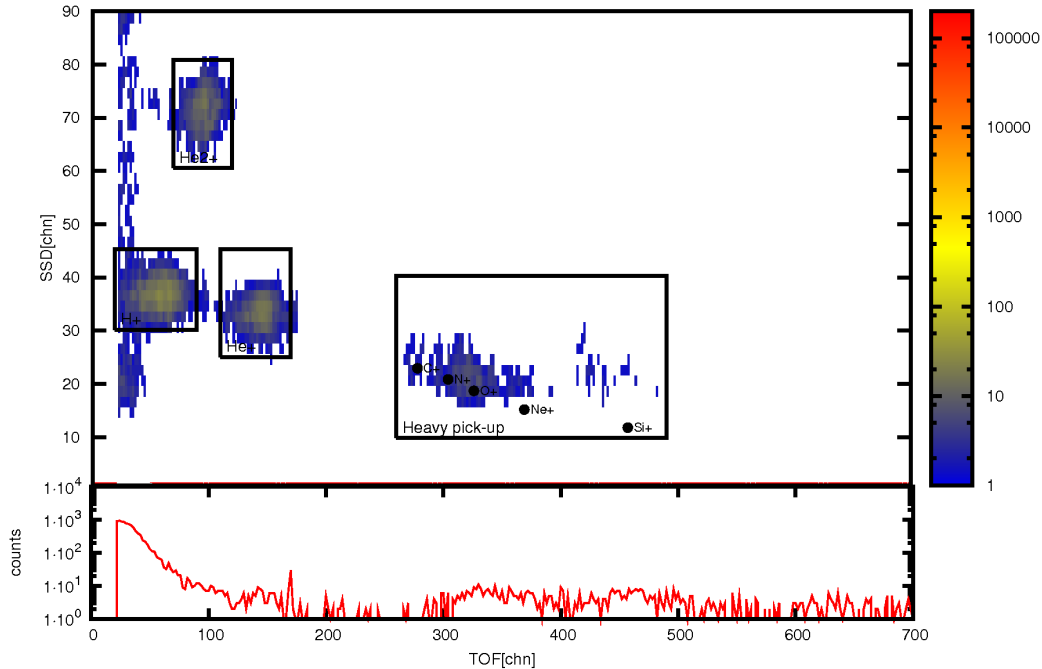


Figure 3.1: This figure shows an exemplary ET matrix for STEREO A - SWS on ESA step 7. Counts were accumulated over a period of 700 days, beginning in February 2007. The x- and y-axes show TOF and SSD channel. The number of counts in each TOF/SSD bin is color coded. The lower panel shows double coincidences for the given time-of-flight range. The black boxes in this ET matrix demonstrate the applied filtering method. For H^+ , He^+ , He^{2+} and heavy pick-up ions an upper/lower limit of TOF/SSD/ESA bins is assigned, in which presumably only events of the specified ion occur.

step) for which the heavy pick-up box can be clearly separated from the heavy ion box. All events of the heavy pick-up and He^+ box were then saved separately into two files, containing the information mentioned above. He^+ will be used mainly for comparisons of pick-up spectra.

We have to point out, that there were aperiodic changes of the Micro Channel Plate (MCP) bias in 2007 and 2008 with voltages ranging from 2.5kV to 2.98kV, which could heavily effect the efficiency of heavy ion detection, hence resulting in time-dependent variances of ion incidences. The accurate dates of changes of the MCP bias are presented in chapter A.2. By investigating only periods of a constant MCP bias, one could avoid these variances. We choose to disregard these voltage changes in order to maintain the already low count rates.

3.1.3 Ion Species Classification

In the next section we are going to examine the ion velocity divided by solar wind velocity distributions ($w = v_{ion}/v_{sw}$) of heavy pick-up ions. In order to create those w -spectra we need information on incident ion masses, which could be derived from the time-of-flight

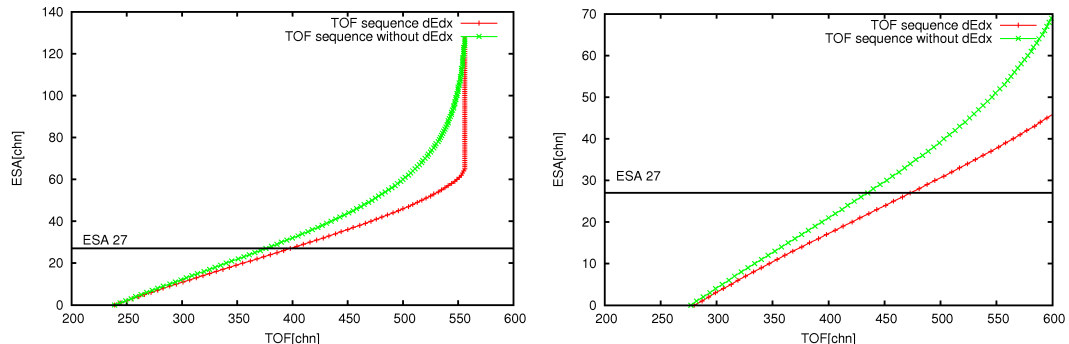


Figure 3.2: This plot shows TOF sequences for O^+ (right panel) and C^+ (left panel). The red curves denote a TOF sequence under consideration of energy loss in the carbon foil, while for the green curves energy loss is neglected. The sequences were calculated with equation A.2 on page 73, using values for the energy loss, which were calculated with SRIM (see chapter A.3). The black lines mark the maximum ESA value of the heavy pick-up filtering and comprise maximum mismatch between these curves.

information under the assumption of singly charged ions.

$$m/q = 2 \cdot (E/q + V_{PAC}) \cdot \alpha(E, m) \cdot (\tau/d)^2, \quad (3.1)$$

where E/q and τ can be derived from the ESA and TOF information. V_{PAC} is a constant voltage of about 20kV. The parameter $\alpha(E, M)$ denotes the energy and species-dependent energy loss in the carbon foil. For any further calculations we assumed a constant energy loss in the carbon foil of 5 percent in respect to the particle energy (species independent), that will, in particular for the heavier ions, lead to an error $\Delta(m/q)$. As a first estimate of this error, we calculate the resulting mismatch $\Delta(m/q)$ of theoretical TOF sequences with and without the allowance of energy losses in the carbon foil. They were derived with equation A.2 on page 73. The energy loss was simulated with SRIM for numerous ions (see chapter A.3). The sequences are shown in figure 3.2 and the resulting errors are shown in table 3.1.3. The disparity between these curves increases with descending E/q -ratio, hence the possible error $\Delta(m/q)$ is most pronounced on ESA step 27. In addition, this error is derived under the assumption of no energy loss at all, leading to a greater disparity of these curves as it would be with our assumption of a constant energy loss of 5 percent. Therefore, this error can only be considered as a maximum error, whereas the calculated m/q will most likely be afflicted with a much lesser deviation than $\Delta(m/q)$.

For every event of the heavy pick-up box we calculate the mass-per-charge ratio, which is then sorted into equidistant mass-per-charge bins ranging from zero to forty with a bin width of 0.4 [u/e]. This m/q spectrum is our initial point of species classification. Any incident particle, assuming a singly charged state, should be sorted into a m/q bin, which corresponds to its mass. So for N^+ we would expect a m/q -ratio of $(m/q)_{N^+} = 14.01$ and for C^+ a ratio of $(m/q)_{C^+} = 12.01$. We emphasize that this does not imply a m/q distribution, which is centered on $(m/q)_{ion}$ with a FWHM of $\Delta(m/q)$, but rather gives an estimate on the center position of the m/q distribution with a deviation of $\Delta(m/q)$. Aberration of the observed distribution center from the expected one will most likely be caused by the assumption of a constant carbon foil energy loss and instrumental

Ion	TOF[chn]	TOF(α)[chn]	$\Delta(m/q)$ [u/e]
C ⁺	375	398	1.5
N ⁺	406	438	2.3
O ⁺	435	472	3.1
Ne ⁺	486	537	4.4

Table 3.1: Maximum errors $\Delta(m/q)$. They were derived by comparing TOF sequences with and without energy loss in the carbon foil (see figure 3.2).

effects, e.g. a constant time-of-flight shift of three to six nano seconds. Furthermore, the FWHM of the m/q distribution can cause overlap of adjacent ions, which demands further analysis of the spectrum to ensure small mutual interference of these ions.

The m/q spectrum is presented in figure 3.3 together with a fit of the spectra, which consists of a combination of four gaussian functions. In order to keep the number of fit parameters small, peak center and FWHM of the four distributions are preset. They were roughly estimated considering the derived errors $\Delta(m/q)$ and the resulting fit. We note, that using this fit for short-term data would require a more precise determination of peak centers and FWHMs by studying the TOF distributions in the ET matrices. Nevertheless, for our purpose of illustrating the four ion contributions, a rough estimate is sufficient.

$$\begin{aligned} f(m/q) = & A_{C^+} \cdot \exp\left(\frac{1}{2}\left(\frac{(m/q) - 12.7}{0.65}\right)^2\right) + A_{O^+} \cdot \exp\left(\frac{1}{2}\left(\frac{(m/q) - 16.8}{1.25}\right)^2\right) \\ & + A_{N^+} \cdot \exp\left(\frac{1}{2}\left(\frac{(m/q) - 14.3}{0.65}\right)^2\right) + A_{Ne^+} \cdot \exp\left(\frac{1}{2}\left(\frac{(m/q) - 20.0}{0.85}\right)^2\right) \end{aligned}$$

In order to obtain species information we define m/q ranges, that are linked to incident particles. Due to overlap of the four discrete m/q ion distributions this is only possible for C⁺ and O⁺, where overlap of adjacent ions contributes only minor parts to the total number of counts in the defined m/q range. For N⁺ and Ne⁺ this contribution can exceed up to fifty percent of total counts, thus preventing an accurate determination of these ions (see figure 3.3). Because of their low count rates, events with m/q -ratios greater twenty are completely neglected, as it is impossible to distinguish between them and the noise of the spectrum. We define our m/q ranges as [14.8:19.0]_{O⁺} and [0.00:13.6]_{C⁺}, so that any event, falling into these ranges, is assumed to be either O⁺ or C⁺.

3.1.4 v_{ion}/v_{SW} Distribution

With information on time-of-flight, mass-per-charge, species and solar wind velocity we can finally derive w -spectra from our list of PHA events. The ion velocity is determined by an event's mass, energy, and charge, where again the energy loss, caused by the carbon foil, is considered to be constant. This leads to a w of

$$w = \frac{v_{ion}}{v_{SW}} = \frac{\sqrt{\frac{2E}{m}}}{v_{SW}}, \quad (3.2)$$

with energy E being calculated with equation 2.1, mass m being derived by an event's mass-per-charge and solar wind velocity v_{SW} being directly obtained from the proton

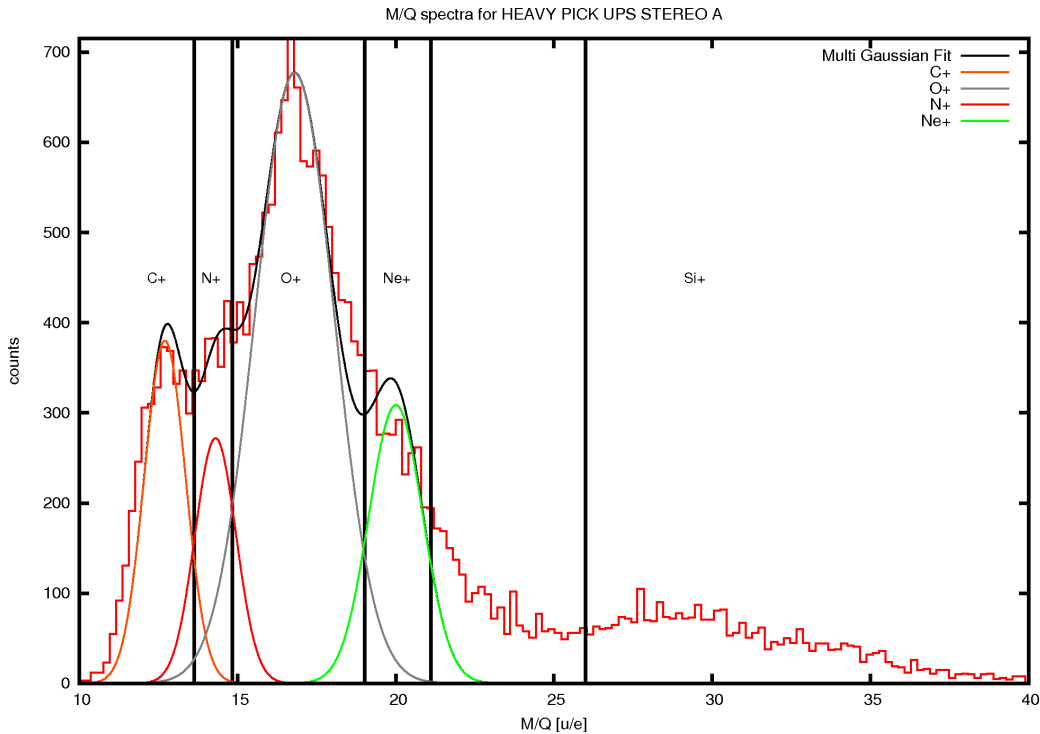


Figure 3.3: This figure shows a m/q spectrum for a period of 700 days of all events from the heavy pick-up box. The x-axis shows mass-per-charge and the y-axis shows counts. All events are sorted into m/q bins with a width of 0.4 u/e. The spectrum is fitted by a combination of four gaussian, labeled C^+ , O^+ , N^+ , and Ne^+ , in order to divide the spectrum into four distinct contribution of the most common heavy pick-up ions. The resulting fit is labeled "Multi Gaussian Fit" and drawn in black.

moments. For events of our heavy pick-up and He^+ box w was computed and sorted into 100 equidistant bins ranging from zero to three, covering the typical range of a pick-up w -spectrum. We present the resulting w -spectrum of He^+ and the most common heavy pick-up ion O^+ in figure 3.4. One can see two peaks within the distribution of He^+ at $w=1$ and $w=2$, which translates into an ion velocity of $v_{ion} = v_{SW}$ and $v_{ion} = 2 v_{SW}$. There is also an efficiency related increase of counts with increasing w , which is caused by the energy dependent detection probability of the instrument. In addition, we accentuate the well pronounced suprathermal tail of He^+ , beginning at about $w=2$, with more than 500 counts even at $w=3$.

A direct comparison of the He^+ and O^+ spectra bares some differences between them. Aside from the obvious lower number of O^+ counts, the spectrum of oxygen seems to be more flattened, without the formation of two peaks at $w=1$ and $w=2$. This is caused by two instrumental effects of STEREO PLASTIC, which we will describe in further detail. PLASTIC measures solar wind particles in an energy-per-charge range of 0.3 keV/e up to 80 keV/e, thus singly charged ions can not exceed a residual energy of 80 keV. For lighter pick-up ions like He^+ this hardly has any effect on the spectrum, because He^+ particles with an energy of 80 keV also travel with a velocity of 2042 km/s, which is greater

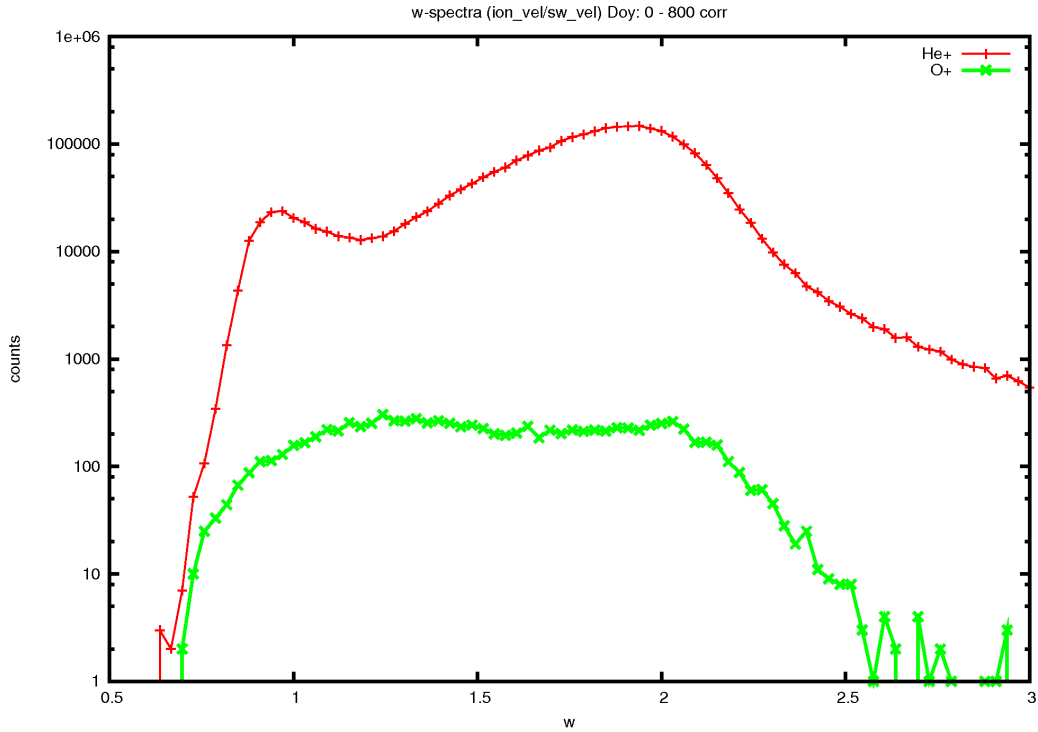


Figure 3.4: This figure shows w -spectra for He^+ and O^+ . The x- and y-axes denote $w = v_{\text{ion}}/v_{SW}$ and counts in a logarithmic scale. Both spectra were computed for a period of 700 days. The maximum bin width of w was set to 0.03.

than $2 v_{SW}$. Heavier pick-up ions, on the other hand, can be strongly influenced by the limited energy range due to their higher mass and resulting slower velocity. Therefore, O^+ can only be measured up to a maximum velocity of 1010 km/s, which corresponds to the maximum energy of about 80keV filtered by the ESEA. This results in a solar wind velocity dependent cut-off of the O^+ w -spectrum, that could explain the weakly

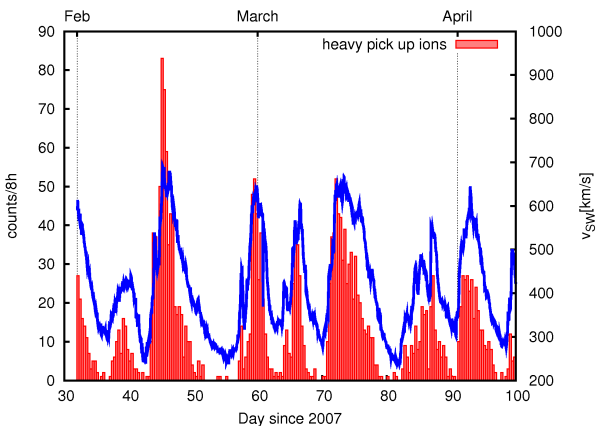


Figure 3.5:
Count rates of heavy pick-up ions are shown for a period ranging from February to April, 2007. Counts on the y-axis are accumulated over 8 hours and plotted over time on the x-axis. The blue curve is linked to the second y-axis on the right side and denotes the solar wind velocity. The number of counts seems to be strongly correlated with v_{SW} . This effect also occurs for other ions than heavy pick-up ions.

pronounced peak at $w=2$.

$$v_{max,ion} = \sqrt{\frac{2((E/q)_{max} \cdot e)}{m_{ion}}} \quad (3.3)$$

Nevertheless this can't explain a missing peak at $w=1$.

Another instrumental effect can influence the O⁺ spectrum in a way, that could result in a depletion of counts at low energies. PLASTIC's SSDs have a minimum measurable energy E_{thresh} of about 35 keV. This will lead to a minimum detectable velocity of

$$v_{min,ion} = \sqrt{\frac{2(E_{thresh})}{m_{ion}}}. \quad (3.4)$$

Presumably, this effect would have a greater effect on He⁺ as on O⁺ due to its lower mass, which seem to be in contrast to our presented w -spectra. But considering that O⁺ will likely lose more of its energy passing the carbon foil, hence having a smaller residual energy E_{res} than He⁺, this still could explain a depletion of counts at small w for the heavier ions.

Bearing these two effects in mind, investigations on heavy pick-up spectra get considerably complicated, as it is difficult to distinguish between effects caused by the instrumental cut-off and effects that are caused by heliospheric phenomena. Though, we are able to estimate the conditions under which an O⁺ spectrum would be most affected by the spectral cut-off, which allows us to create a rough valuation of the real spectrum later in this chapter.

A visualization of the cut-off effect is presented in figure 3.6 for O⁺ and He⁺. Events of the heavy pick-up box are sorted into a total number of 10.000 bins, which are composed of 100 v_{SW} and 100 w bins ranging from 0 to 1.000 km/s and zero to three respectively. This allows us to visualize the solar wind velocity dependence of w . For both plots the red curve denotes the maximum w caused by the highest E/q -ratio of the instrument, while the green curve denotes the minimum w due to the detector threshold.

As expected, O⁺ seems to be far more affected by this spectral cut-off than He⁺, especially under consideration that He⁺ has its maximum intensity in a w and v_{SW} range, that is cropped for O⁺. Counts of the He⁺ spectrum appear to increase with increasing solar wind velocity up to a certain point of about v_{SW}=700 km/s, where the occurrence of such high speeds becomes significantly rare. The same holds true for a lower limit of solar wind velocity, causing a strong depletion of counts at solar wind speeds below 350 km/s. Between these two limits the occurrence of velocity bins is assumed to be nearly constant with small aberrations, that are considered for calculations later in this chapter. Therefore, an increased number of counts in this range mainly originates from the efficiency related enhanced count rates on high solar wind velocities. A similar effect can be observed for the x-axis, where w bins below one and above two become significantly rare. In the typical pick-up range between $w=1$ and $w=2$ an increased w results in higher ion velocities, which explains the enrichment of events with increasing w . Both effects finally result in the observed peak of He⁺ at v_{SW}=600 and $w=1.9$, which in case of O⁺ can not be observed.

This implies an influence on the O⁺ spectrum, that is most pronounced on high solar wind velocities in the suprathermal range. Still, O⁺ seems to occur more frequent in high speed streams, even under the influence of the instrumental cut-off (see figure 3.5).

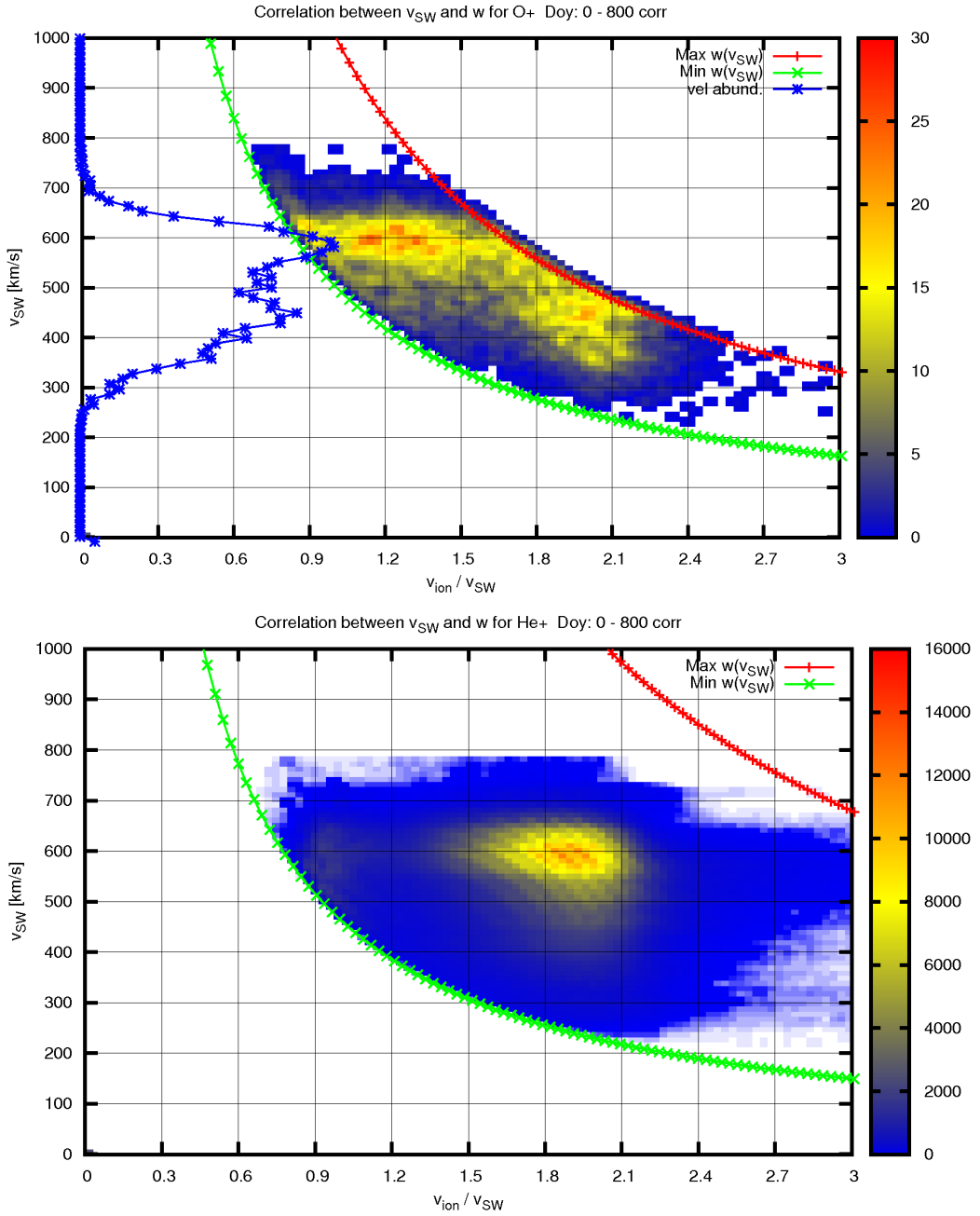


Figure 3.6: This plot shows the v_{SW} dependent cut-off of w -spectra for O^+ (upper panel) and He^+ (lower panel), which is from here on called vw -matrix. The x-axis denotes $w=v_{ion}/v_{SW}$ ranging from zero to three and the y-axis shows v_{SW} from 0 to 1.000. Both the x- and y-axes are divided into 100 equidistant bins. The color in each bin represents number of counts accumulated over a period of 700 days. The red curves in each of the plots visualize the highest measurable w bin in dependence of the solar wind velocity, caused by PLASTIC's maximum E/q -ratio of about 80keV/e. The green curves stand for the lowest possible w bin, caused by the SSD threshold. The upper panel also contains a blue curve, which is the normalized occurrence $\psi(v_{SW})$ of solar wind velocity bins for the given period.

But we have to point out that, despite better statistics, investigations on O⁺ in the fast solar wind ($v_{SW} > 500$ km/s) would be afflicted by an eminent error due to the instrumental cut-off, that could easily outreach any error caused by lower statistics. Hence, it is necessary to obtain missing parts of the spectrum, which is done in the next section of this chapter.

3.1.5 Reconstruction of the O⁺ w Spectrum

To reconstruct an O⁺ spectrum, we have to make some assumptions, which could narrow down some of the possible results. The most extensive one is the assumption of similar spectral shapes of He⁺ and O⁺, which not necessarily needs to be true, as pick-up helium is believed to originate mainly from the interstellar medium, while oxygen should mainly emanate from inner sources. Anyhow, He⁺ is the only pick-up ion that is virtually not affected by any instrumental cut-offs and is therefore well suited as a reference for extrapolation of counts in energy ranges, that can not be measured for other ions.

In order to reconstruct missing parts of the O⁺ spectrum we first compensate for the inconstant occurrence of v_{SW} bins in the upper panel of figure 3.6. For that we accumulated all appearing v_{SW} bins, using a time resolution of thirty minutes, with a v_{SW} bin width of 10 km/s in a range of $v_{SW} = [0:1000]$. The result $\psi(v_{SW})$ is then normalized and applied to the matrix in the upper panel of figure 3.6 by dividing all counts in each velocity and w bin by the normalized velocity occurrence.

$$C_{w,v} = \frac{C'_{w,v}}{\psi_v}, \quad (3.5)$$

where w and v (for v_{SW}) represent bin numbers, ψ the normalized velocity occurrence, C' the uncorrected number of counts and C the corrected number. The result would be equivalent to a vw -matrix, shown in figure 3.6, without fluctuations in intensity due to the erratic appearance of solar wind velocities. The next step is to extrapolate the O⁺ spectra in areas of the vw -matrix, that are influenced by the spectral cut-off. Those areas appear above the red curve and below the green curve presented in figure 3.6 in a total range of $v_{(-:+)} = [340:640]$. We limited our extrapolation to this velocity range, as it provides enough statistic for a reliable result and contains the most common velocity bins. An illustration of these extrapolated areas is presented in figure 3.7. The reconstruction of the spectrum is performed as follows:

$$\begin{aligned} F_{(w,A)} &= \Delta w \left(v_{(+)} - v_{(w,max/ion)} \right) \\ F_{(w,B)} &= \Delta w \left(v_{(w,max/ion)} - v_{(w,min/ion)} \right) \\ F_{(w,C)} &= \Delta w \left(v_{(w,min/ion)} - v_{(-)} \right) \end{aligned}$$

$F_{(w,X)}$ is the surface area of X in bin w , while $v_{(+/-)}$ and $v_{(w,max/min/ion)}$ denotes the upper/lower limit of our extrapolation range and accordingly maximum/minimum measurable velocity bin caused by the instrumental cut-off. Δw is the used bin width of 0.03.

$$C_{(w,A)} = \left(\frac{F_{(w,A)}}{F_{(w,B)}} C_{(w,B)} \right) \cdot \frac{\left(v_{(+)} + v_{(w,max/ion)} \right)}{\left(v_{(w,max/ion)} + v_{(w,min/ion)} \right)} \quad (3.6)$$

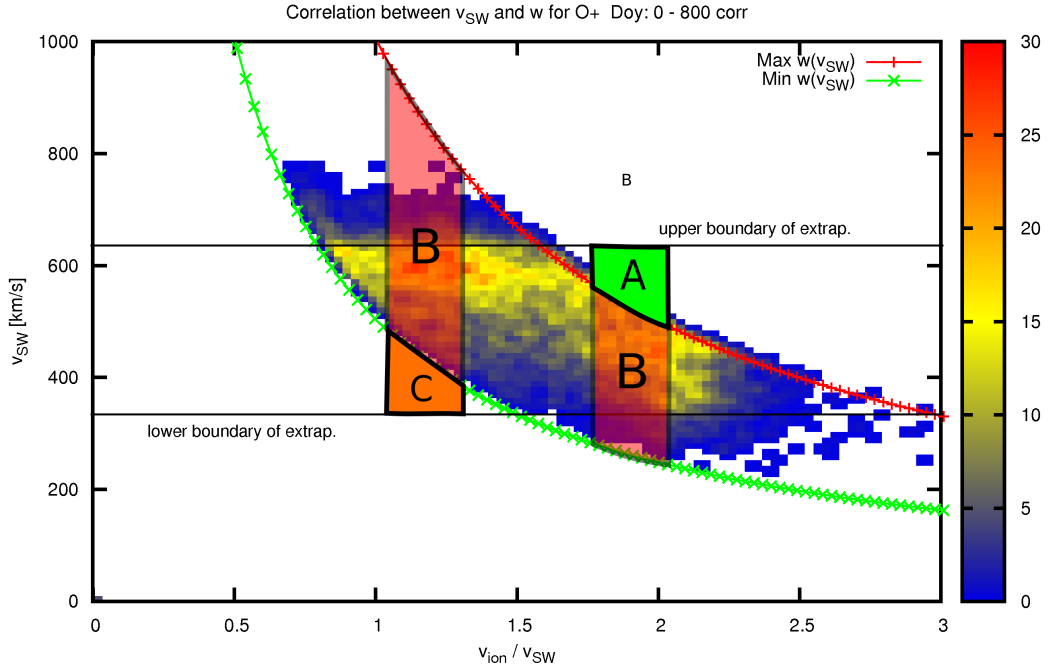


Figure 3.7: This plot illustrates the areas A and C, which are extrapolated by using events in area B. Area B covers the full velocity range for each w bin, that was not cut-off, while for area A and C the maximum and minimum velocity is specified by the extrapolation range shown in black lines. Reconstruction of counts is done for every w bin with a width of 0.03, hence the portrayed areas are not drawn to scale.

$$C_{(w,C)} = \left(\frac{F_{(w,A)}}{F_{(w,B)}} C_{(w,B)} \right) \cdot \frac{(v_{(w,min,ion)} + v_{(-)})}{(v_{(w,max,ion)} + v_{(w,min,ion)})}, \quad (3.7)$$

where $C_{(w,X)}$ denotes number of counts in $F_{(w,X)}$.

We assume a count density in each w bin, that is increasing/decreasing with the ascending/descending solar wind velocity respectively. Hence, we assign the counts $C_{(w,B)}$ in area $F_{(w,B)}$ to $C_{(w,A/C)}$ in proportion to area $F_{(w,A/C)}$. Counts in $F_{(w,A/C)}$ are then weighted by a factor (as seen on the right side of equations 3.6 and 3.7), which denotes the ratio of the average velocity covered by area $F_{(w,A/C)}$ and $F_{(w,B)}$. Anyhow, the correction of this efficiency related effect will unlikely reproduce counts in $F_{(w,A/C)}$ exactly, because it only compensates for different mean solar wind velocities in each of the areas and not for the single v_{SW} bins. The results of $C_{(w,A/C)}$ can therefore be considered as a lower limit of expected O^+ counts.

$$C_{(w,total)} = C_{(w,A)} + C_{(w,C)} + C_{(w,B)} \quad (3.8)$$

By summing $C_{(w,A/B/C)}$ we obtain reconstructed counts for each w bin, which finally results in our extrapolated w -spectrum of O^+ (figure 3.8). As mentioned before, we reconstruct only a lower limit of counts in $F_{(w,A/C)}$, which then requires further adjustments to fit a not observed real spectrum of oxygen. For that, we delete parts of the

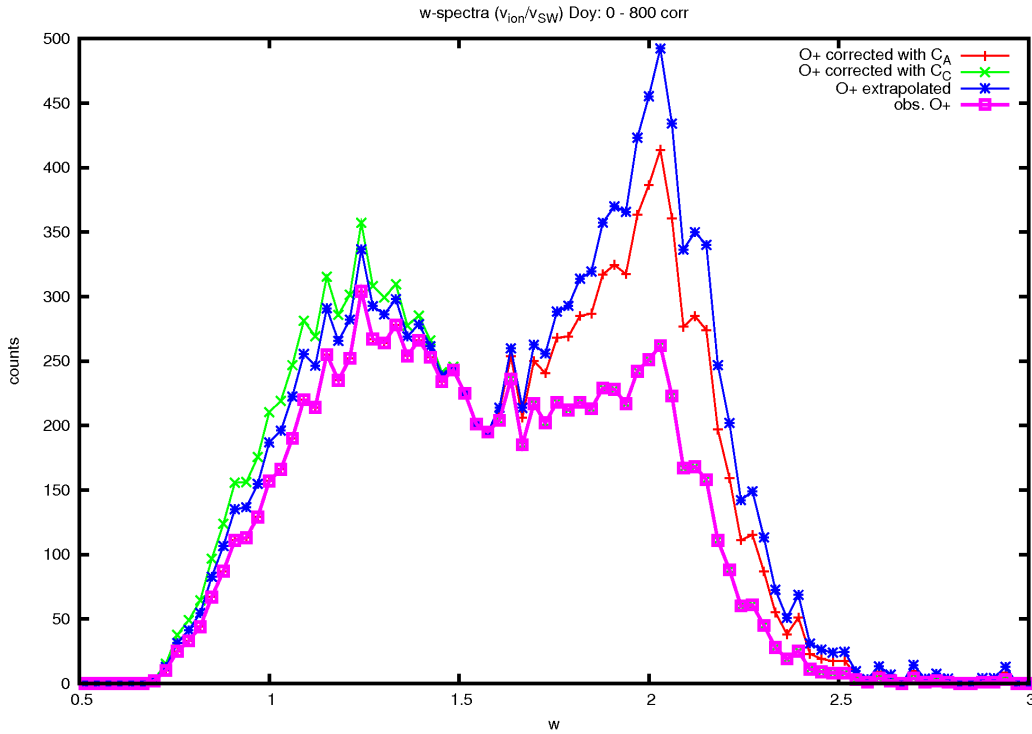


Figure 3.8: The reconstructed w -spectrum of O^+ is presented in blue. It accounts for the missing events in area A and C (red and green curve), which are additionally adjusted to the efficiency related increased count rates on higher solar wind velocities (blue curve). This extrapolation is considered to be an lower limit of the real pick-up oxygen spectrum. For comparison, the observed spectrum of O^+ is drawn in violet.

He^+ vw -matrix, that are cut off for O^+ . The cropped He^+ vw -matrix is then reconstructed by our algorithm, as described before. By comparing our reconstruction results and the observed He^+ vw -matrix, we are able to calculate a correction function $\beta(w)$ by dividing the observed counts in each w bin by the reconstructed ones for He^+ . As a result, we obtain a correction factor for each w bin, which accounts for the efficiency related increased counts on higher w bins. With $\beta(w)$ we are now able to reproduce the cropped vw -matrix of helium in a way, that the resulting w -spectrum is identical with the observed w -spectrum of helium.

If oxygen and helium would have a similar energy dependent efficiency and spectral shape, $\beta(w)$ can be used to reconstruct parts of the O^+ spectrum, that are cut off by the instrument.

$$C_{(w, total)} = \frac{1}{\beta_w} \cdot (C_{(w, A)} + C_{(w, C)}) + C_{(w, B)} \quad (3.9)$$

The method is illustrated in figure 3.9 for He^+ . The resulting O^+ spectrum is shown in figure 3.10.

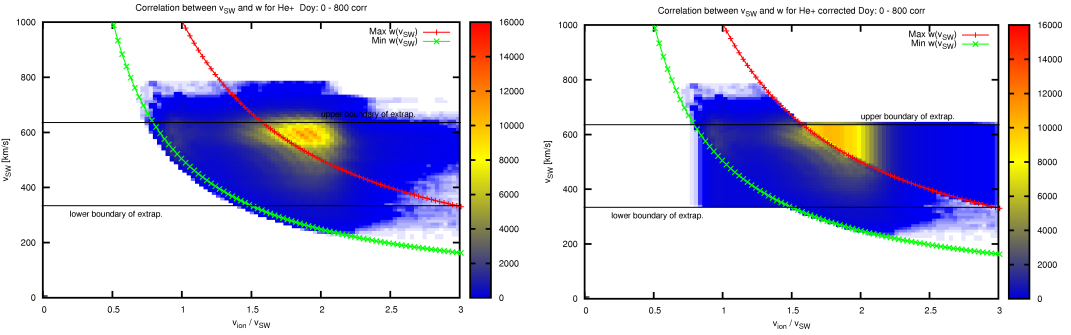


Figure 3.9: This figure compares the observed pick-up helium spectrum (left panel) with the reconstructed one (right panel). The right panel is produced by cropping out parts of the observed spectra, that are in the cut-off range of O^+ , which is above the red and below the green curve. The cropped parts of the vw -matrix are then reconstructed by applying our extrapolation algorithm and adjusted with the calculated correction function β . This finally results in a reconstructed w -spectrum of helium, that is identical with the observed one.

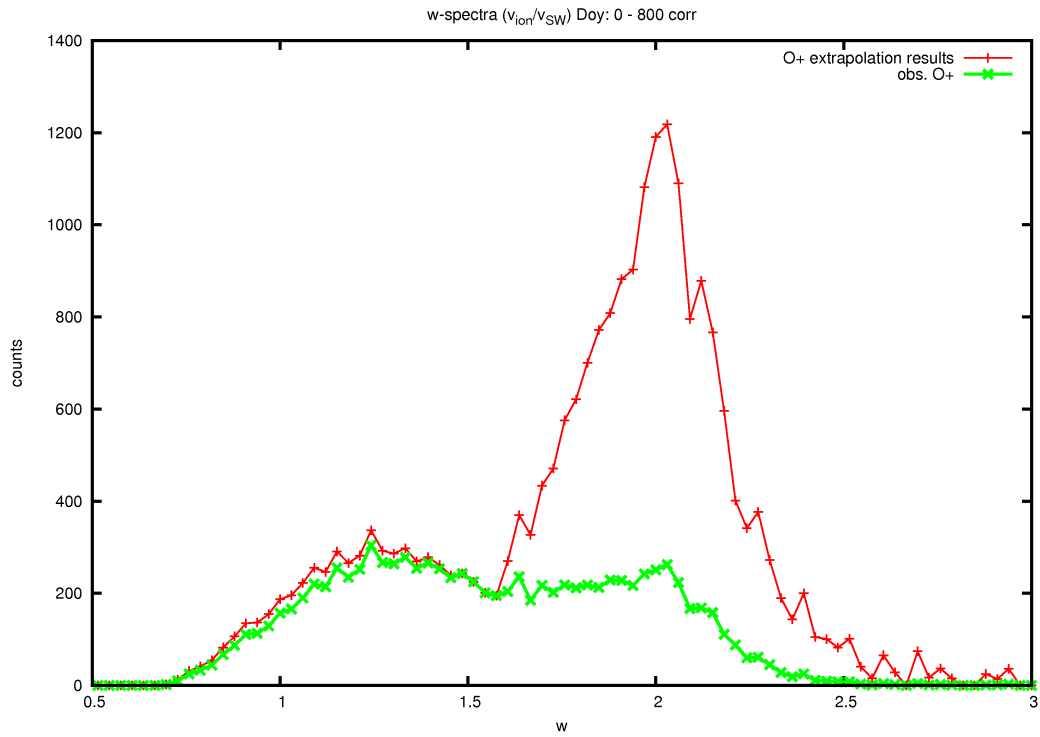


Figure 3.10: This figure shows the extrapolated w -spectrum of O^+ , which was then adjusted by the correction function $\beta(w)$ (red curve). The observed oxygen spectrum is drawn in green.

3.1.6 Discussion

Although the described method would be sufficient to extrapolate missing parts of a long-term O⁺ spectrum due to the instrumental cut-off, it is not possible to extrapolate spectra for smaller periods, as the quality of the results is heavily reliant on good statistics. Especially in the case of slow solar wind, where O⁺ is barely measurable, an extrapolation of only few oxygen counts will most likely lead to a relative error, that exceeds the 100%. It is also necessary to choose a period for reconstruction, where the solar wind velocity at least covers most velocity bins of our extrapolation range with v_(-:+)=[340:640] km/s and a bin width of 10 km/s to assure a statistical significance of the extrapolation result.

In addition, small scale structures of the O⁺ abundance, which could emanate from inner sources, would alter the reconstruction results in a way, that can not be foreseen, as we assumed a similar spectral shape of He⁺ and O⁺ for our algorithm. This assumption also implicates that both He⁺ and O⁺ have a similar detection efficiency, as we assumed a linear ascending number of counts with increasing solar wind velocity, which then was adjusted by the function $\beta(w)$. We have to keep in mind that $\beta(w)$ has been derived by dividing our extrapolated helium spectrum with the observed one to obtain a function, which applied to the extrapolation result, results in the observed spectrum. Thus, we know that $\beta(w)$ is a function of the He⁺ efficiency, which can not be applied to O⁺ without tolerating an eminent error.

Efficiency

To improve our extrapolation algorithm, one could use the actual efficiency of the corresponding ion to describe the velocity or rather energy dependent number of counts. The detection efficiency can either be obtained by using pre-flight values or several trigger rates of the instrument, which account for MCP aging and resulting time-dependent efficiency in contrast to the pre-flight results.

1. SF0: This is the "START" rate, which counts the number of triggered "START" events at the TAC board.
2. SFR0: This is the "STOP" rate, which counts the number of triggered "STOP" events at the TAC board, if a corresponding "START" exists.
3. S-VALID: This rate counts every valid signal, whereas the validation of a signal is basically defined by the instrument's electronics. The precise requirement for a valid signal is described in *Longworth* [Revision 2.0].
4. RA: This rate denotes the number of events, which trigger a position signal at the resistive anode. It is assumed to operate with 100% efficiency.

The total efficiency is then given by

$$\eta(E)_{tot} = \eta_{start} \cdot \eta_{stop} \cdot \eta_{valid} \quad (3.10)$$

$$= \left(\frac{SF0}{RA} \right) \cdot \left(\frac{SFR0}{SF0} \right) \cdot \left(\frac{S - VALID}{SFR0} \right) \quad (3.11)$$

$$= \frac{S - VALID}{RA}, \quad (3.12)$$

where both rates $S - VALID$ and RA are sorted by ESA steps. Now in order to obtain the efficiency of a single ion, one has to choose ESA steps, in which the chosen ion is most prominent and use equation 3.12 to derive the energy dependent parameter $\eta(E)_{tot}$. This method has already been applied for He^+ , He^{2+} and H^+ and is planned to be used for deriving the O^{6+} efficiency in the future. Although this approach is fitted for calculation of in-flight efficiencies, it is assumed to be afflicted by a distinct error caused by the assumption of an ideal RA trigger efficiency and the simple fact, that even the most prominent species like protons can not be fully separated from other species by ESA steps, which in turn leads to contaminated trigger rates. Hence, this error will increase with decreasing relative ion abundances in respect to the solar wind composition and complicates any efficiency calculation of the less abundant solar wind species, including heavy pick-up ions.

Because the efficiency for heavy PUIs is not available yet, we have used a different approach to deal with the instrumental efficiencies for our analysis. This approach is described in the next chapter in further detail.

3.2 Implications on Heavy Pick-up Abundances

In this section we analyze time series of pick-up ion count rates for He^+ , C^+ , O^+ , and Ne^+ in a time period of 750 days, beginning in February 2007 and ending in April 2009. We start with a general introduction of our applied method of time and velocity binning, which ensures a nearly constant efficiency of different pick-up species, followed by a detailed discussion about noticeable structures of the heavy pick-up count rates and their causes.

3.2.1 Heavy Pick-up Ion Abundances with PLASTIC

The method of obtaining our heavy pick-up data has already been described in chapter 3.1.2. In order to derive the He^+ count rates we used our box rate method described in chapter 2.5.2. For both data sets a maximum time resolution of sixty minutes is used, which in case of heavy pick-up ions is necessary to compensate for their rarity. We present in figure 3.11 time series of He^+ , C^+ , O^+ , and Ne^+ counts together with ratios of C^+/He^+ and O^+/He^+ , using a time resolution of 24 hours. For this figure we did not apply any form of correction or modification, hence it shows 24 hour averages of raw counts. As mentioned in the previous chapter Ne^+ is contaminated by oxygen counts, that fall into the classification range of neon (see figure 3.3), thus the panel labeled " Ne^+ " can only be considered as a maximum neon count rate.

One can notice an enrichment of counts aligned around November, 2007 and October, 2008, which is most pronounced for He^+ and Ne^+ and could be the result of a focusing effect described in chapter 1.3.2. For O^+ and C^+ count rates are slightly increased in this period, but it is impossible to decide, whether this is a real feature or caused by a missing efficiency correction on basis of this figure. This topic will be discussed in further detail later in this chapter.

There also seems to be a downward trend of counts with increasing time. This trend is likely caused by MCP aging. The aging effect results in decreased efficiencies and can be attenuated by raising the MCP voltage stepwise, which in turn leads to non-linear changes of the efficiency in time. This makes data analysis of long time series far more difficult, as one has to keep track of the MCP voltage changes in order to distinguish between particle events or rather sudden changes of the detection efficiency due to a higher MCP voltage. An increased MCP voltage also causes more noise in the time-of-flight signal, which degrades the quality of PHA words and is the reason why we mainly focussed our analysis on STEREO A in this thesis (see chapter A.2).

There are also several small scale structures visible, like an enhancement of O^+ and C^+ on, e.g., day 426 (2008/03/01), which is probably caused by a coronal mass ejection (see STEREO CME list <http://cor1.gsfc.nasa.gov/catalog/>). A CME-related enhancement of O^+ and C^+ has also been found with ACE/SWICS by Berger [2009]. As mentioned before, we are going to use a long-term binning to circumvent the efficiency related variation of count rates. Thus, this binning will not allow for a detailed analysis of these small scale structures.

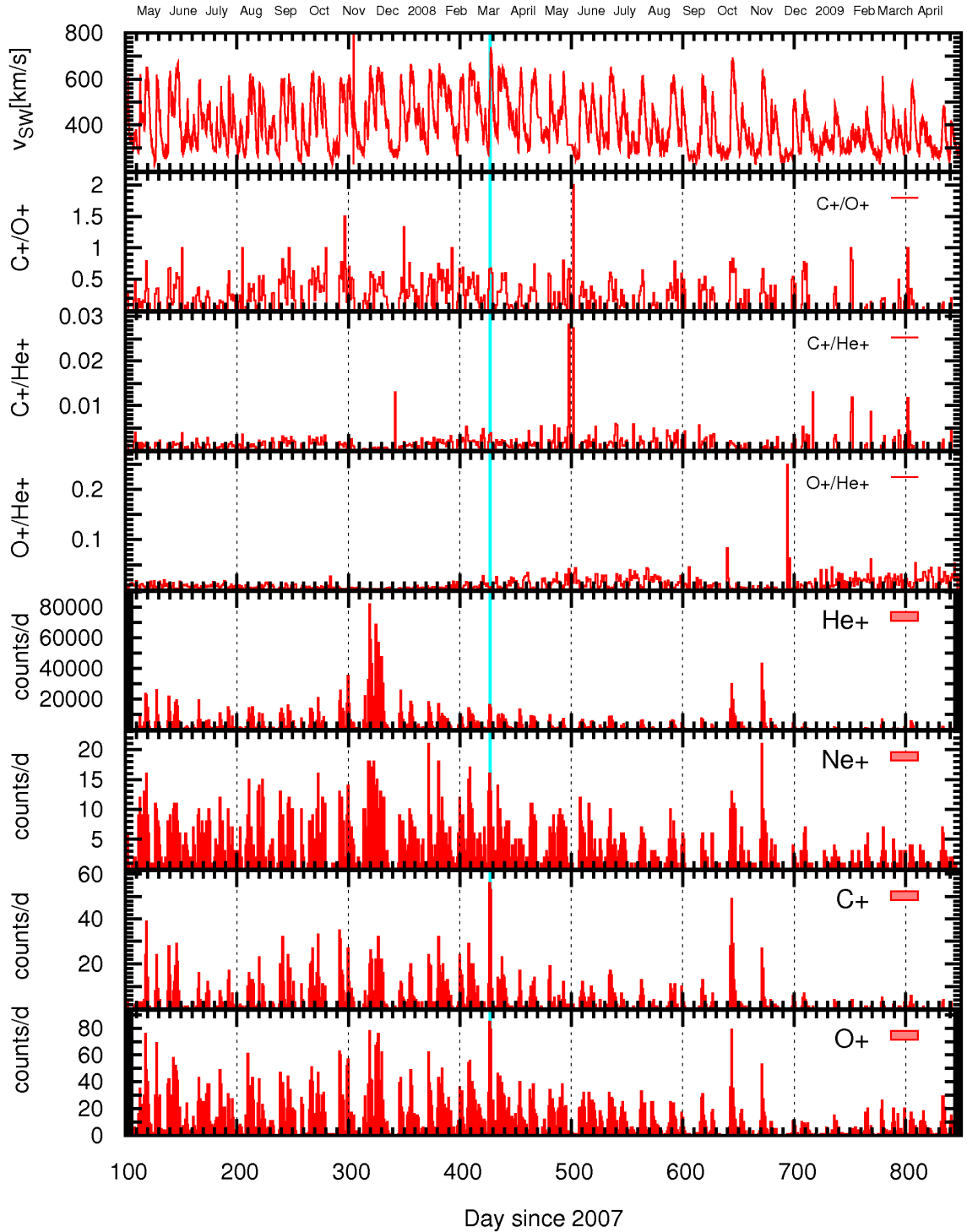


Figure 3.11: This figure shows pick-up ion count rates in a period of 750 days using a time resolution of 24 hours. The x-axis shows days since 2007. The panels show from top to bottom solar wind velocity, C^+/O^+ , C^+/He^+ , O^+/He^+ , He^+ counts, Ne^+ counts, C^+ counts and O^+ counts. The solar wind velocity in the top panel was obtained from the calculated proton moments of PLASTIC. The blue line marks the occurrence of a CME on 2008/03/01.

Figure 3.12 shows again counts of pick-up ions, but in a smaller time period and a higher time resolution of 10 hours. Here we can see a strong correlation of counts with the solar wind velocity for every species, which is caused by the energy dependent efficiency. But as the energy of a particle is proportional to its mass m and the solar wind velocity v_{SW} to the power of two, the efficiency will also change differently for different pick-up ions in time and hence, will not allow for a direct comparison of these species for short time periods. In slow solar wind the SSD threshold (see equation 3.4) in combination with the decreased efficiency can even result in an extinction of pick-up events (compare day 500 in figure 3.12), which prohibits the analysis of pick-up ions in these time periods at all.

Beside the velocity correlation there is also an enrichment of He^+ , C^+ and O^+ at the beginning of high speed streams, which is most likely caused by a compression region at the stream interfaces of CIRs (see day 408, 428, 432, 480 and 534 in figure 3.12). This density correlation has also been confirmed by Moebius [2009]. He assumed that PUIs undergo the same compression as the solar wind.

If we want to account for the efficiency related variations of PUI count rates, it is not sufficient to average counts over preferably long time periods. We have to consider, that the detection probability depends on the particle energy, which in turn depends on the solar wind velocity. The efficiency of PUIs would be constant, if we ensure a constant occurrence of solar wind velocities over time. We know the corresponding solar wind velocity v_{SW} for each measured pick-up event, which allows us to derive the number of velocity bins per time. If we use a time bin width, that is sufficient to cover almost all velocity bins, we can normalize the inconstant appearance of velocity bins with a bin width of 100 km/s by dividing the number of pick-up events per hour and velocity bin by the number of corresponding velocity bin occurrences within the chosen time bin interval t_w .

$$\bar{C}_{t_b} = \sum_{t=t_b}^{t_b+t_w} \sum_v \frac{C_{v,t}}{N_{v,t_b} t_w}, \quad (3.13)$$

where $C_{v,t}$ denotes pick-up counts of hour t and velocity bin v , N_{v,t_b} the number of occurred velocity bins in time bin t_b and \bar{C}_{t_b} the averaged hourly count rate of pick-up ions under the assumption of an even distributed solar wind velocity occurrence in time bin t_b . We suppose, that a time bin width t_w of 27 days is ideal, as it ensures a constant velocity occurrence not only by equation 3.13 but also by the solar rotation, which in an ideal case produces the same solar wind structures every 27 days. In fact, the solar rotation would be ~ 28 days for STEREO A and ~ 26 days for STEREO B, but for reasons of comparability we chose an averaged time of circulation for our time binning. The combination of a long time binning and solar wind velocity normalization then leads to a constant detection efficiency, which is composed of the respective velocity bin contributions in equal shares, over time.

For different pick-up species our binning still does not yield identical mean efficiencies. Thus, the obtained count rates do not give us the absolute abundances of PUIs. But they are sufficient to study relative changes of the abundances and allow us to analyze pick-up ion ratios and variations of the observed count rates.

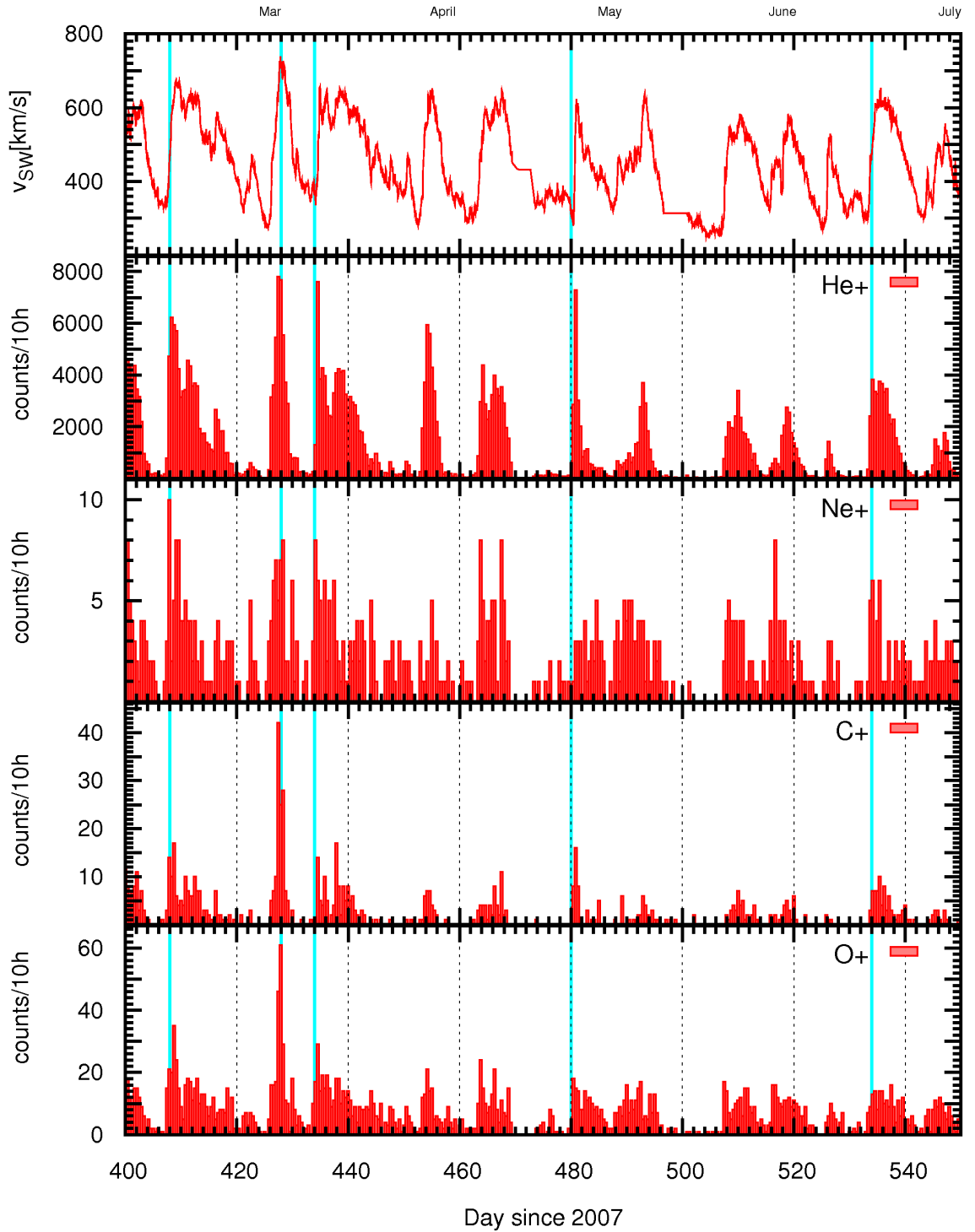


Figure 3.12: This figure shows pick-up ion count rates in a period of 150 days using a time resolution of 10 hours. The x-axis shows days since 2007. The panels show from top to bottom solar wind velocity, He^+ counts, Ne^+ counts, C^+ counts, and O^+ counts. The blue lines mark compression regions at the stream interfaces of Corotating Interaction Regions (CIRs).

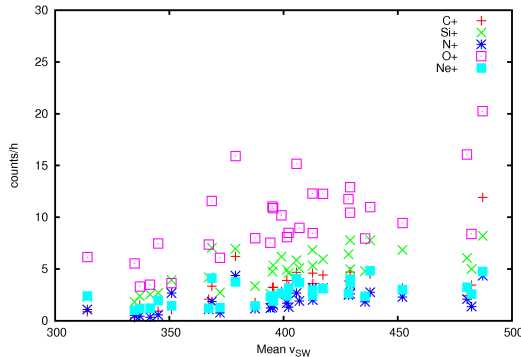


Figure 3.13:

Averaged counts per hour of heavy pick-up ions are plotted over the corresponding mean solar wind velocity. The averaged count rate per hour was derived with equation 3.13, while the mean solar wind velocity is averaged over 27 days. There is a small linear dependence of counts with v_{SW} , which is probably caused by an insufficient coverage of velocity bins in some 27-day bins.

In figure 3.13 we present the resulting averaged counts of various pick-up ions in dependence of the corresponding averaged solar wind velocity. If our binning procedure results in a constant efficiency, we would not expect any correlation between averaged counts and mean velocity. But it seems to exist a small correlation, or rather an upward trend of counts with increasing mean solar wind velocity, which is probably caused by an insufficient coverage of velocity bins in some 27-day bins. Nevertheless, this correlation is small and we expect our binning procedure to dispose most of the efficiency related effects.

In figures 3.14, 3.15 and 3.16, 3.17 we present results of our binning procedure in a time period of 750 days beginning in February, 2007 and ending in April, 2009 for STEREO A and STEREO B respectively. For both spacecraft pick-up ion count rates are plotted over day since 2007 and the running heliographic longitude in respect to 2007/01/01. We have to remark that for STEREO B almost exactly the same algorithms were used to obtain and classify pick-up ions from PHA Data. The only modification made, is a constant SSD_{chn} shift in our boxes (see figure 3.1) to account for the different SSD offsets compared to STEREO A. However, both instruments on STEREO A and B are not completely identical in terms of the solid state detector characteristics and conversion from ESA to E/q , TOF_{chn} to τ_{ns} and SSD_{chn} to E_{SSD}, hence our applied algorithms for mass-per-charge and mass could produce uncertainties in species classification and pick-up ion velocities for STEREO B, as both algorithms were optimized for A. In addition, the MCP voltage on B is already higher than on A, thus causing more noise in time-of-flight and greater uncertainties in m/q .

Because of that we will not discuss any features visible in figure 3.16 and 3.17, and just present it for reasons of completeness. In figure 3.14 several structures in the pick-up count rates are visible, which are possibly caused by changes of instrumental parameters. First we have to identify these periods as they interfere with our search for an enrichment of pick-up ions by gravitational focusing and sungrazing comets.

1. In mid February, 2007 the MCP voltage of PLASTIC A was increased by 184V to 2.843kV, which could have resulted in a steep increase of counts followed by a persistent decay until mid of July, 2007. This decay would also imply a subsequent slowly decreasing efficiency up to a certain level lasting nearly 100 days, which is most unlikely to be solely an effect of MCP aging. If we consider, that a similar structure occurs 300 days later in February, 2008 and another 350 days later in January, 2009, this structure is most unlikely to be caused by instrumental effects.

Possible reasons for this structure are discussed in the following chapters.

2. In mid June, 2007 the MCP voltage again was increased to 2.915kV, which in turn had hardly any effect on the number of pick-up events.
3. On April 13th, 2008 the MCP power supply went offline for a short period, after which the MCP voltage was gradually increased until April 17th to its highest value of 2.92kV so far. In this period an enrichment of N⁺ and C⁺ exists, which could have been caused by an enhanced efficiency. But still, this enhancement should have also had an effect on O⁺ and He⁺ counts, which is not the case.
4. In January, February and March 2009 the MCP voltage was increased stepwise up to 2.99kV. The only noticeable change in pick-up count rates in this period is a drop of He⁺ counts, which led to an increase of the C⁺/He⁺ and O⁺/He⁺ ratios in January lasting only a month.

From (1),(2),(3) and (4) we conclude, that although MCP voltage changes will affect the detection efficiencies and hence the number of pick-up events, they will most unlikely cause a distinct enrichment of counts as seen on days 100, 300, 400, 640, and 750. Thus, in the following section we present potential reasons for the enhanced number of pick-up events in these periods.

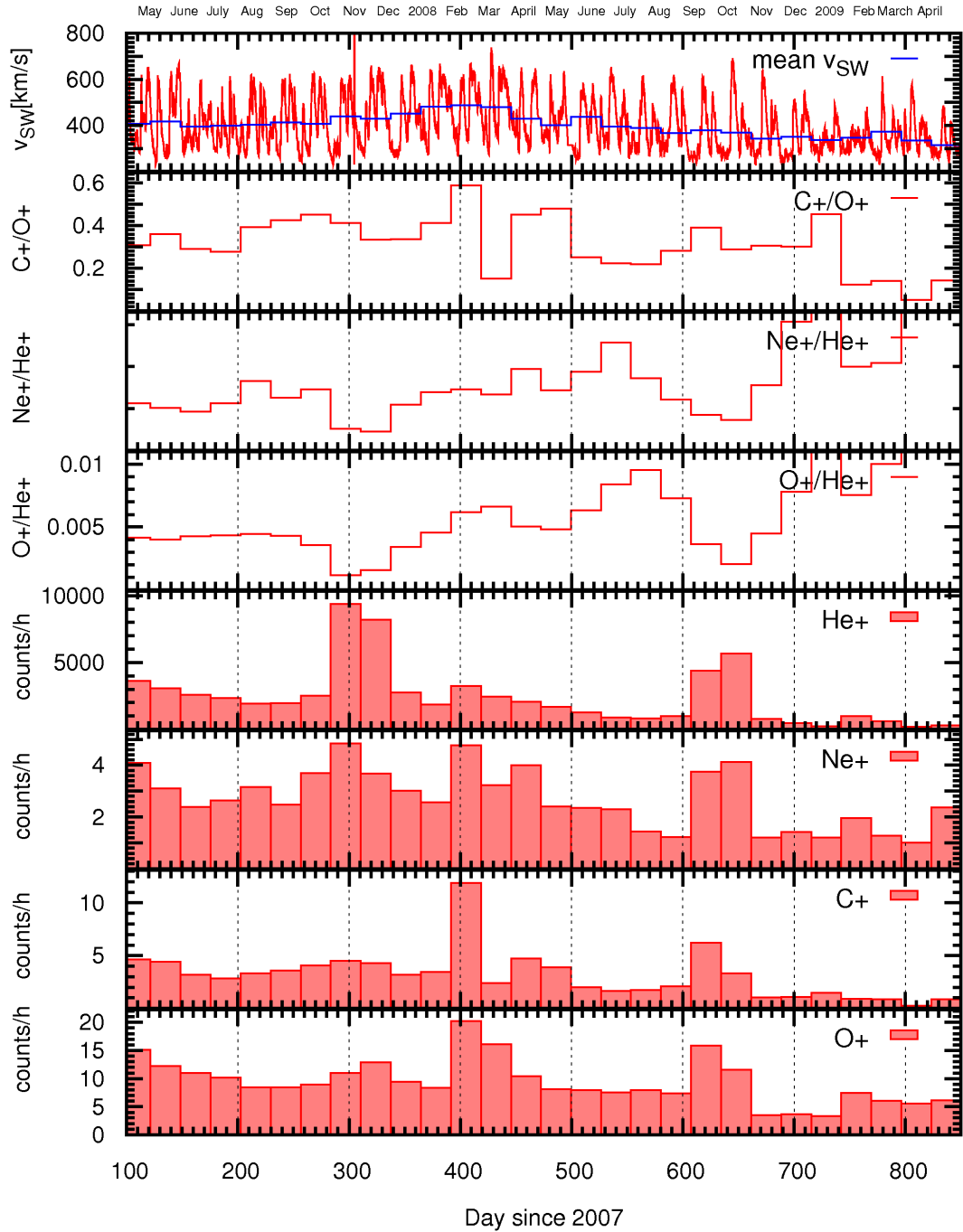


Figure 3.14: This figure shows pick-up ion count rates for STEREO A in a period of 750 days using a time resolution of 27 days and our binning procedure, which ensures a constant efficiency over time. The x-axis shows days since 2007. The panels show from top to bottom solar wind velocity, C^+/O^+ , Ne^+/He^+ , O^+/He^+ , He^+ counts/h, Ne^+ counts/h, C^+ counts/h and O^+ counts/h.

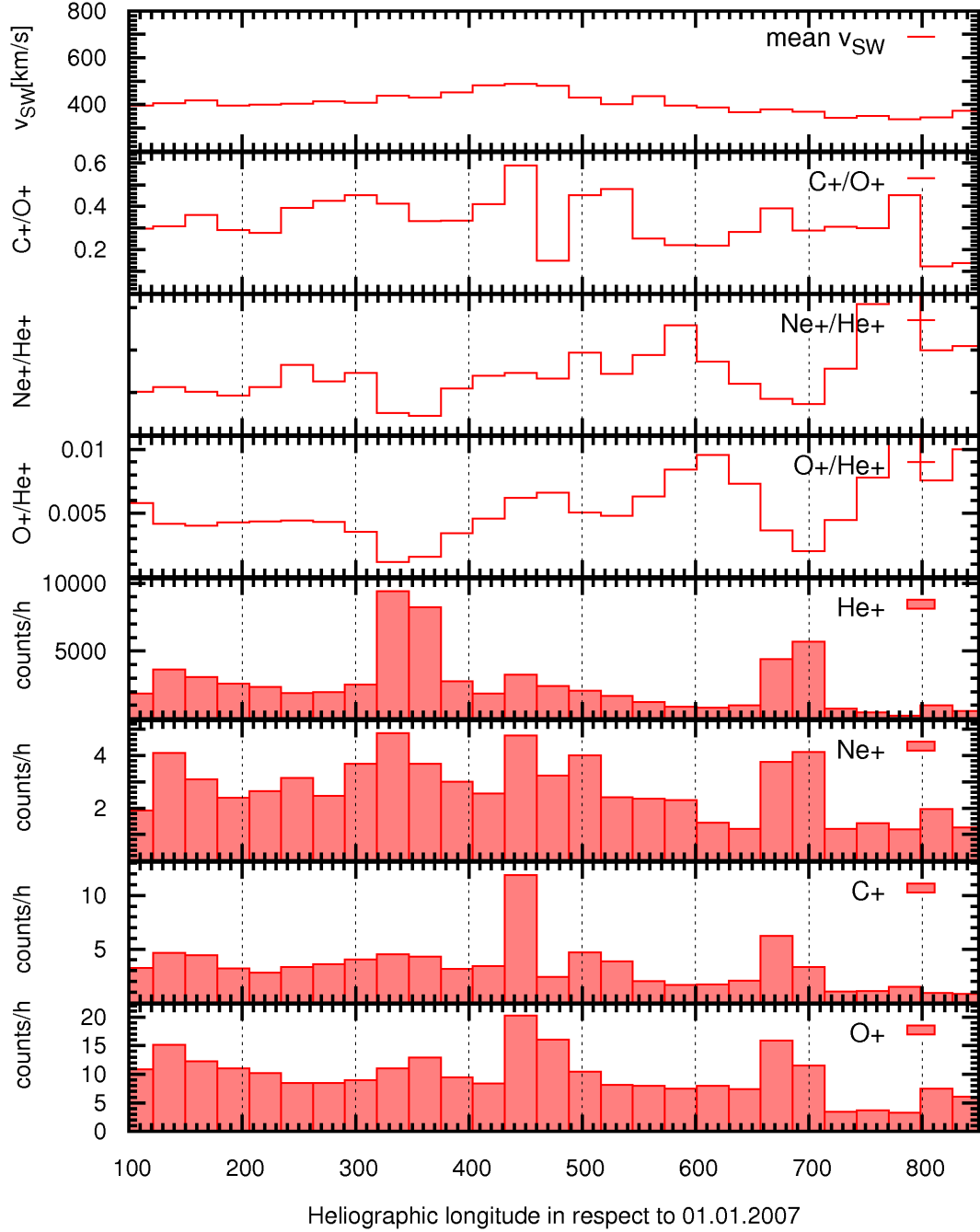


Figure 3.15: This figure shows pick-up ion count rates for STEREO A in a period of 750 days using a time resolution of 27 days and our binning procedure, which ensures a constant efficiency over time. The x-axis shows the running heliographic longitude in respect to 2007/01/01. The panels show from top to bottom solar wind velocity, C^+/O^+ , Ne^+/He^+ , O^+/He^+ , He^+ counts/h, Ne^+ counts/h, C^+ counts/h and O^+ counts/h.

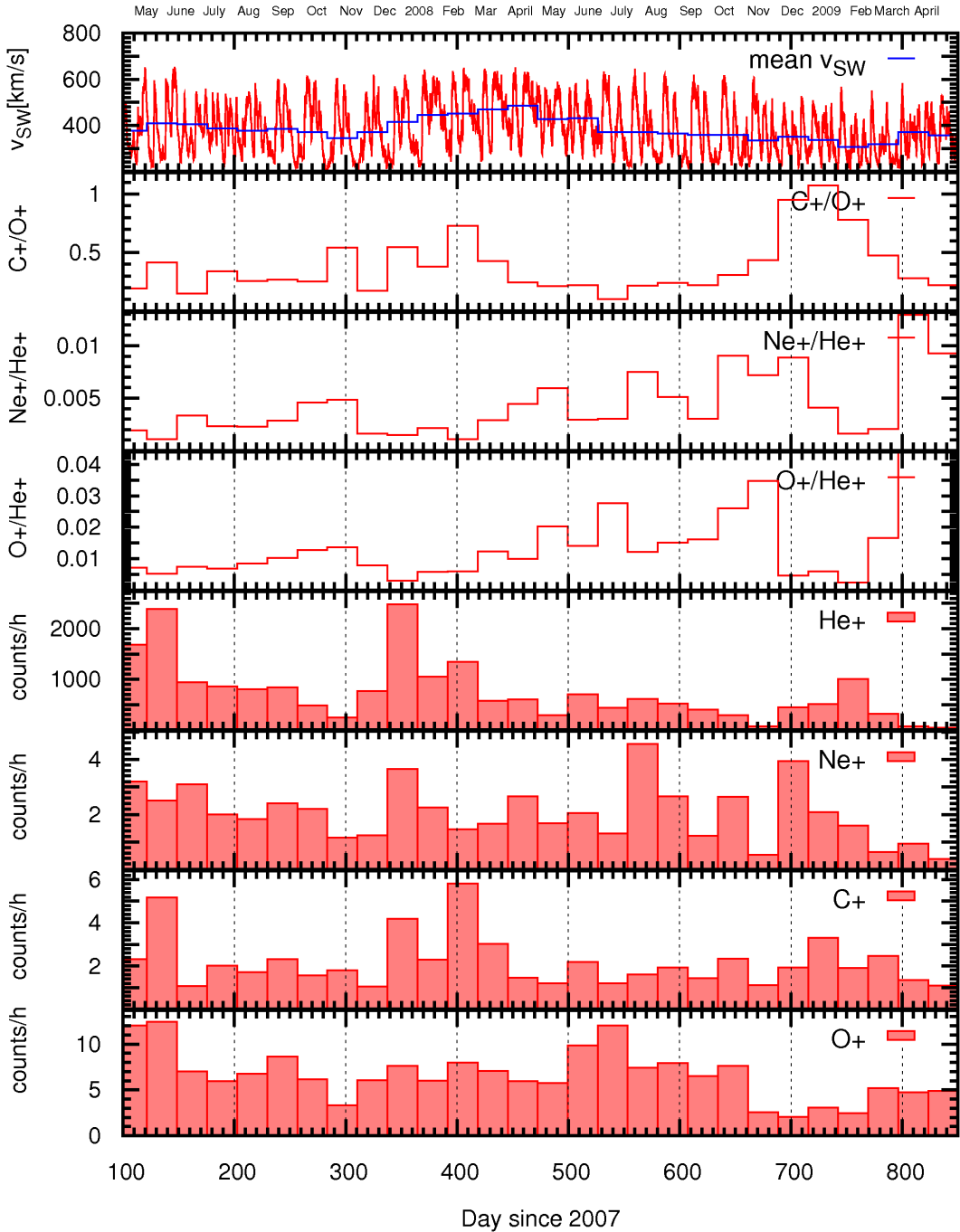


Figure 3.16: This figure shows pick-up ion count rates for STEREO B in a period of 750 days using a time resolution of 27 days and our binning procedure, which ensures a constant efficiency over time. The x-axis are days since 2007. The panels show from top to bottom solar wind velocity, C^+/O^+ , Ne^+/He^+ , O^+/He^+ , He^+ counts/h, Ne^+ counts/h, C^+ counts/h and O^+ counts/h.

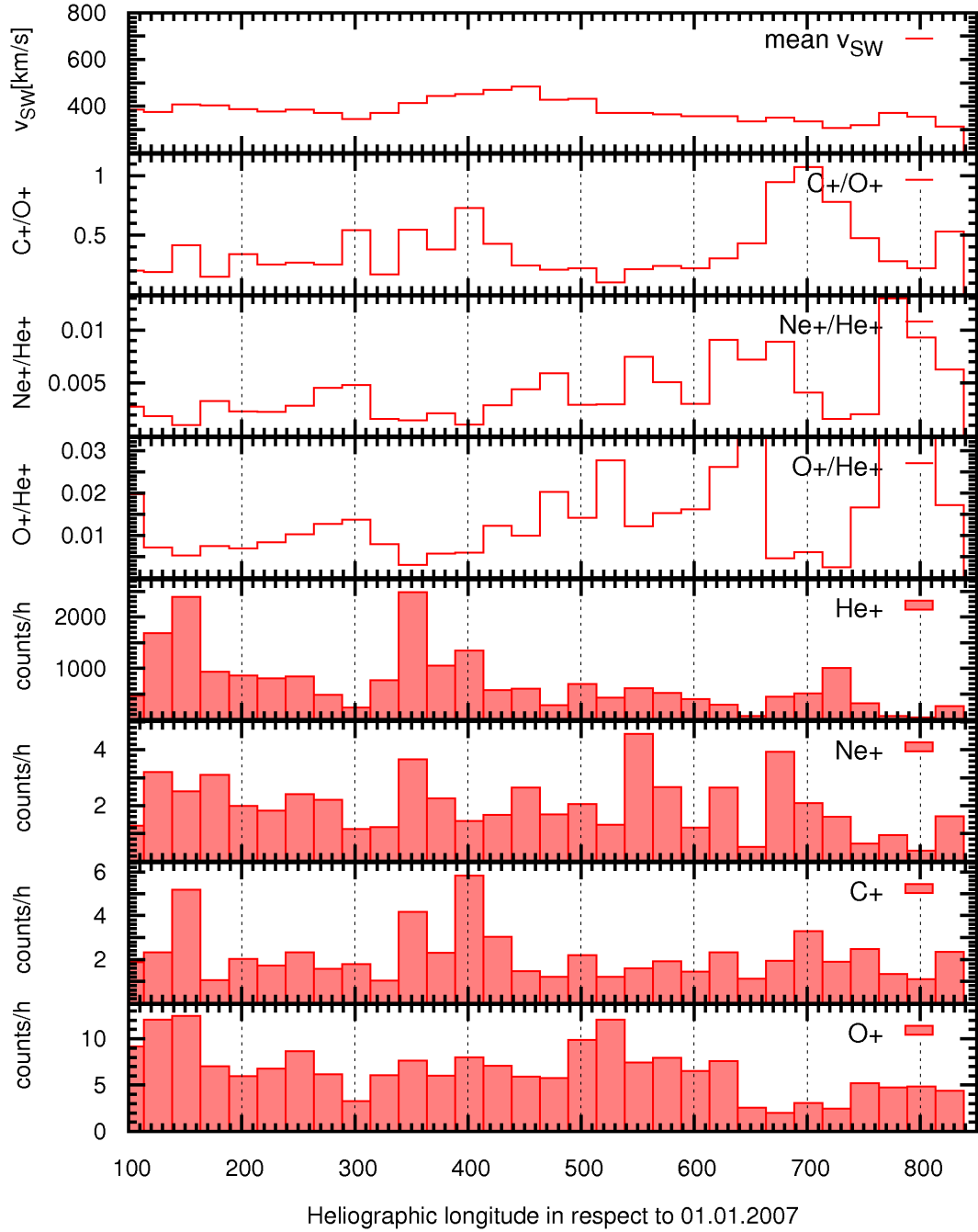


Figure 3.17: This figure shows pick-up ion count rates for STEREO B in a period of 750 days using a time resolution of 27 days and our binning procedure, which ensures a constant efficiency over time. The x-axis shows the running heliographic longitude in respect to 2007/01/01. The panels show from top to bottom solar wind velocity, C^+/O^+ , Ne^+/He^+ , O^+/He^+ , He^+ counts/h, Ne^+ counts/h, C^+ counts/h and O^+ counts/h.

3.2.2 Sungrazing Comets

In the year 1880 Heinrich Kreutz observed repeated returns of comets very close to the sun and suggested, that they could be members of a related comet group, that had separated from each other at some earlier perihelion passage [Marsden, 2005]. Up to now over 1000 sungrazing comets have been observed with the SOHO/LASCO coronographs, which also allow the determination of precise orbital parameters of these objects and so were able to confirm the idea of Kreutz. Today, we know that there exists even more than one group of sungrazing comets, which are named after their discoverers Kreutz, Meyer, Kracht and Marsden. While members of a group have very similar orbital parameters caused by an equal origin, the groups itself differ from each other as shown in figure 3.18.

On their approach phase sungrazers will gradually release water (70%), carbon dioxide (10%) and carbon oxide (20%) molecules, caused by sublimation of the volatile components. On their perihelion passage most of the comets' nuclei (if not all) will completely disintegrate and due to the vicinity to the sun, then be fully dissociated. We obtain from *Greenberg* [1999] the mass composition of cometary nuclei with 43% H, 27% O, 25% C and 5% iron and other atoms. The contributions of both the approach phase and perihelion passage could lead to an enhancement of pick-up ions, as the released material will be nearly instantaneously ionized by solar radiation and then picked up by the solar wind. Although, this enhancement would only last from hours to days, the sheer amount of released cometary material should produce a distinct enrichment of pick-up ions, which is even visible with our long time averages. Neglecting transportation of pick-up ions in heliographic longitude, we would expect a detection of these inner source pick-up ions released from cometary coma and nuclei once a year for an Earth bound spacecraft and every \sim 340 days for STEREO A at a time where both the spacecraft and sungrazer can be connected by a radial line originating at the sun. Here we assume a radial propagation of cometary pick-up ions, as seen by *Gloeckler* [1986] for comet 21P/Giacobini-Zinner and *Gloeckler* [2000] for comet C/1996 B2 Hyakutake. From *Bzowski and Krolikowska* [2005] we obtain the detection interval of sungrazing comet related pick-up ions for an Earth bound spacecraft with

- Interval - Earth bound spacecraft:
July 30th - Nov. 3rd
- Approximated Interval - STEREO A:
June 30th - Oct. 3rd, 2007.

Comparing these dates with our pick-up ion count rates from figure 3.14, we do not see any noticeable increase of pick-up events in this period. Though, three months earlier on day 100 of 2007 an enrichment of He^+ , O^+ , C^+ and Ne^+ is visible, which could have emanated from sungrazers, assuming unprecise detection intervals from *Bzowski and Krolikowska* [2005]. This event reoccurs on day 400, which is consistent with STEREO A's time of circulation, considering a maximum uncertainty of 27 days for both events. Nevertheless, the enhancement of He^+ and Ne^+ in these periods can not be explained by released cometary volatile or nuclei components, considering the cometary composition, and a sustained decay of counts for three months is not expected, as the sungrazing comet related pick-up events should only last from hours to days. Furthermore, a contribution to the pick-up count rate by cometary dust, which could at least explain the enhancement

of helium and neon, has been already ruled out by *Sekanina* [2000].

Thus, we suppose that sungrazing comets are not the reason for the enrichment seen in figure 3.14, but still could be the cause for small time variances of the pick-up count rates.

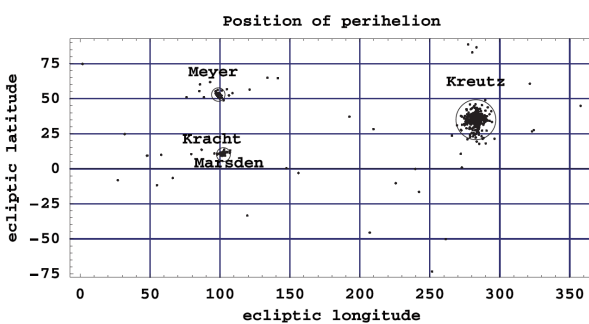


Figure 3.18:

This plot shows the distribution in ecliptic longitude and latitude of observed sungrazers at their perihelion passage. Although the Marsden and Kracht comets have very similar orbits close to the sun, their orbit parameters still allow a distinction of those groups. The picture was taken from *Bzowski and Krockowska* [2005].

3.2.3 Focusing Cone

First observations of the helium focusing cone took place in 1984/85 with the SULEICA instrument on the IRM spacecraft of the AMPTE mission [*Möbius et al.*, 1985]. Since then, understanding and observation of the focusing effect has been substantially improved by new sensitive time-of-flight mass spectrometers like SWICS and PLASTIC, allowing observation of cone transits continuously since 1998, whereas an Earth bound spacecraft, such as ACE, will fly through the cone once a year and STEREO A and B every 346 and 388 days respectively. The cone does not necessarily maintain its structure on each fly-by, as it is dependent on physical properties of He atoms in the local interstellar medium, their velocity relative to the sun, their number density, temperature and ionization processes in the heliosphere [*Gloeckler et al.*, 2004].

Figure 3.19 shows five He^+ cone transits from 1998 to 2002 measured by ACE/SWICS in a $w=v_{\text{ion}}/v_{SW}$ range of 1.4 to 2. Here, not only the change of the He^+ density with solar activity is visible, but also a large day-to-day variability (light violet curve), which is probably caused by varying ionization rates, alfvén speeds and/or a non-radial expansion of the solar wind [*Gloeckler et al.*, 2004]. From the five transits in 1998, 1999, 2000, 2001, 2002 one can obtain the ecliptic longitude of the interstellar wind flow direction with $\lambda=74.43^\circ \pm 0.33^\circ$, which is in good agreement with measurements by the Ulysses spacecraft and EUVE satellite.

In figure 3.20 the first cone passage of STEREO A PLASTIC is shown. It was measured in a $w=v_{\text{ion}}/v_{SW}$ range of 1.45 to 1.85 for 1 and 9 day sliding averages (light violet and red curve respectively), using the efficiency correction described in chapter 3.1.6. It shows a similar day-to-day variability of He^+ counts and a similar cone structure with a slightly shortened passage time caused by STEREO A's shortened time of circulation in respect to ACE. However, the increase of He^+ counts in the cone seems to be more distinct with PLASTIC as with ACE, considering similar activity states of the sun (see figure 1.2). A reason for that could be the different w ranges used for obtaining helium pick-up counts, which could result in a higher background for SWICS produced by solar

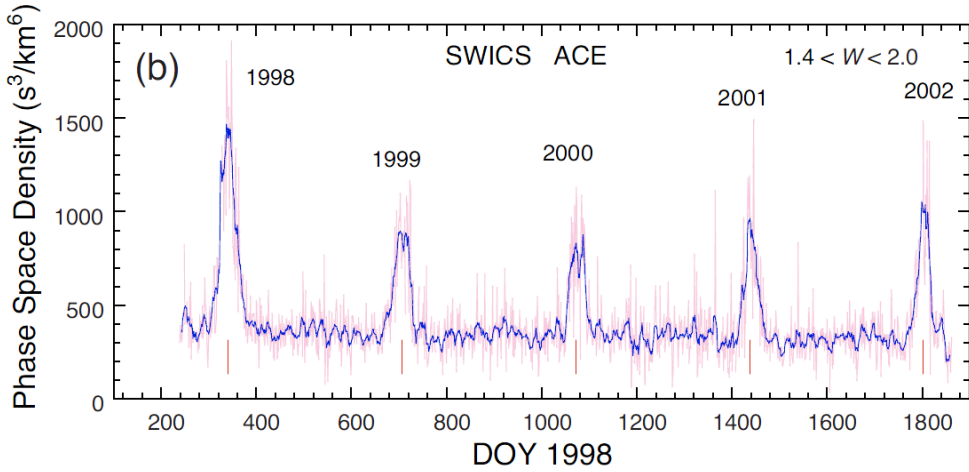


Figure 3.19: This figure shows five transits of the gravitational focusing cone of interstellar helium with ACE/SWICS. Pick-up helium was measured in a w range of 1.4 to 2 using a 1 day average (light violet curve) and 9 day sliding average (blue curve). The y-axis denotes phase space density and the x-axis day since 1998. In the year 2000 the sun was in a state of high activity, which resulted in smaller ionization rates and a weakly pronounced cone at this time, whereas the distinct cone of 1998 results from an enhanced ionization rate during solar minimum (see figure 1.2). The picture was taken from *Gloeckler et al. [2004]*.

wind H^+ and He^{2+} spill over.

Figure 3.21 shows our derived time series of pick-up counts in the same period as in figure 3.20 with a resolution of 1 hour. In order to isolate the O^+ and C^+ distribution in our pick-up box rate, we had to exclusively use triple coincidences, while for figure 3.20 also double coincidences were used. Furthermore, no efficiency correction or modifications to account for a cut-off of the heavy pick-up spectra were made, in figure 3.21. Thus, we observe a strong correlation of pick-up events with the solar wind velocity as described in previous chapters. Because of that, a cone structure, as seen in figure 3.20, is barely visible or rather strongly influenced by the varying solar wind velocity. Nevertheless, we can highlight the distinct enhancement of pick-up helium at day 330 with over 8000 counts per hour, which marks the highest count rate of He^+ from 2007 to 2009 so far, while on the contrary C^+ , Ne^+ and O^+ do not show a well pronounced increase of counts in this period.

Using our time and velocity binning from chapter 3.2.1, we see in agreement with *Moebius [2009]* a helium cone transit on day 300 and day 640 within uncertainties of ± 27 days caused by the chosen bin width of 27 days (see figure 3.14). Furthermore, a noticeable enrichment of heavy pick-up ions occurs in periods of the helium cone transit. On day 300 this enrichment is most pronounced for Ne^+ with only small increases of counts for C^+ and O^+ , while for day 640, marking the second cone passage of PLASTIC, a distinct peak for each of our analyzed pick-up ions is apparent. We have to point out, that an enrichment of Ne^+ during the second transit could potentially be caused by enriched oxygen, that fell into the m/q classification range of neon (compare figure 3.3). In figure 3.22 we present the angular dependency of pick-up ion fluxes $F(r, \theta)$ originat-

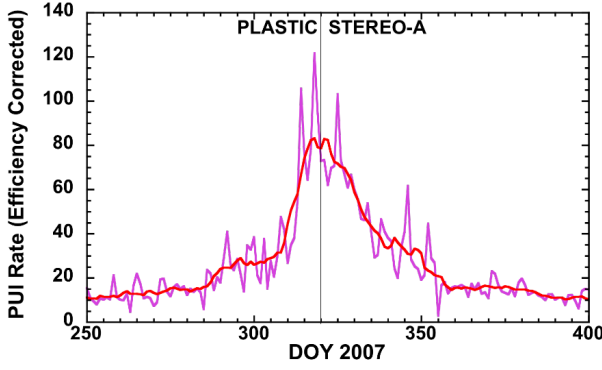


Figure 3.20:

This figure shows the first He^+ cone transit of STEREO A with PLASTIC in a w range of 1.45 to 1.85. The y-axis denotes the efficiency corrected count rate while the x-axis denotes days of the year 2007. The cone passage occurred on day 319. The picture was taken from *Moebius [2009]*.

ing in the interstellar medium, which was originally derived by *Vasyliunas and Siscoe [1976]*. It is calculated as follows:

$$F(r, \theta) = \frac{n_\infty}{v_\infty} \frac{1}{\sin(\theta)} \frac{r_0^4}{r^2} R_{ionis}^2 \cdot \left[\theta \Psi \left(\frac{p_{01}}{\lambda \theta} \right) + (2\pi - \theta) \Psi \left(\frac{p_{02}}{\lambda (2\pi - \theta)} \right) \right],$$

with

$$\begin{aligned} \lambda &= r_0^2 \theta / (\tau v_\infty) \\ \Psi(x) &= x e^{-1/x} - E(1/x) \\ -E(1/x) &= \int_{1/x}^{\infty} dt \frac{e^{-t}}{t}, \end{aligned}$$

where n_∞ and v_∞ denote the velocity and density of pick-up ion species in the interstellar medium, p_{01} and p_{02} impact parameters defining each point in the ecliptic by two orbits, r_0 a reference point at 1 astronomical unit, R_{ionis} the ionization rate at point $P(r, \theta)$ and θ the angle between the inflow direction of the LISIM and point $P(r, \theta)$. Due to a lower ionization efficiency of He^+ and Ne^+ by solar radiation, these species are able to penetrate deep into the heliosphere, which is not the case for O^+ and C^+ [*Kallenbach et al., 2000*]. In figure 3.22 we see, that focusing of interstellar neutrals is most efficient for He^+ . The increase of the He^+ flux in times of the cone transit is about 100 times higher as for oxygen and thus assumingly as for carbon, considering similar ionization potentials of O and C. But a decrease of the O^+/He^+ ratio in the order of two magnitudes is not observed (see figure 3.14) and therefore we do not expect oxygen and carbon to be of interstellar origin. Further evidence is provided by *Gloeckler and Geiss [1998]*, who derived an upper limit of the abundance ratio of interstellar C^+/O^+ in the heliosphere of 0.05. Our derived C^+/O^+ ratio lies in the range of 0.1 and 0.6, but is also influenced by the species-dependent cut-off and efficiency.

Considering the similar masses of carbon and oxygen, the spectral cut-off would have a similar effect on C^+ as on O^+ , and thus is unlikely the reason for the observed ratio. An efficiency related effect on the observed ratio would implicate, that the detection probability of C^+ would be 2 to 10 times higher than for O^+ , which is also not likely. In fact, investigations with ACE/SWICS showed, that the efficiency of O^+ is higher than for C^+ , thus our derived ratio is even too low. Therefore, we conclude, that our

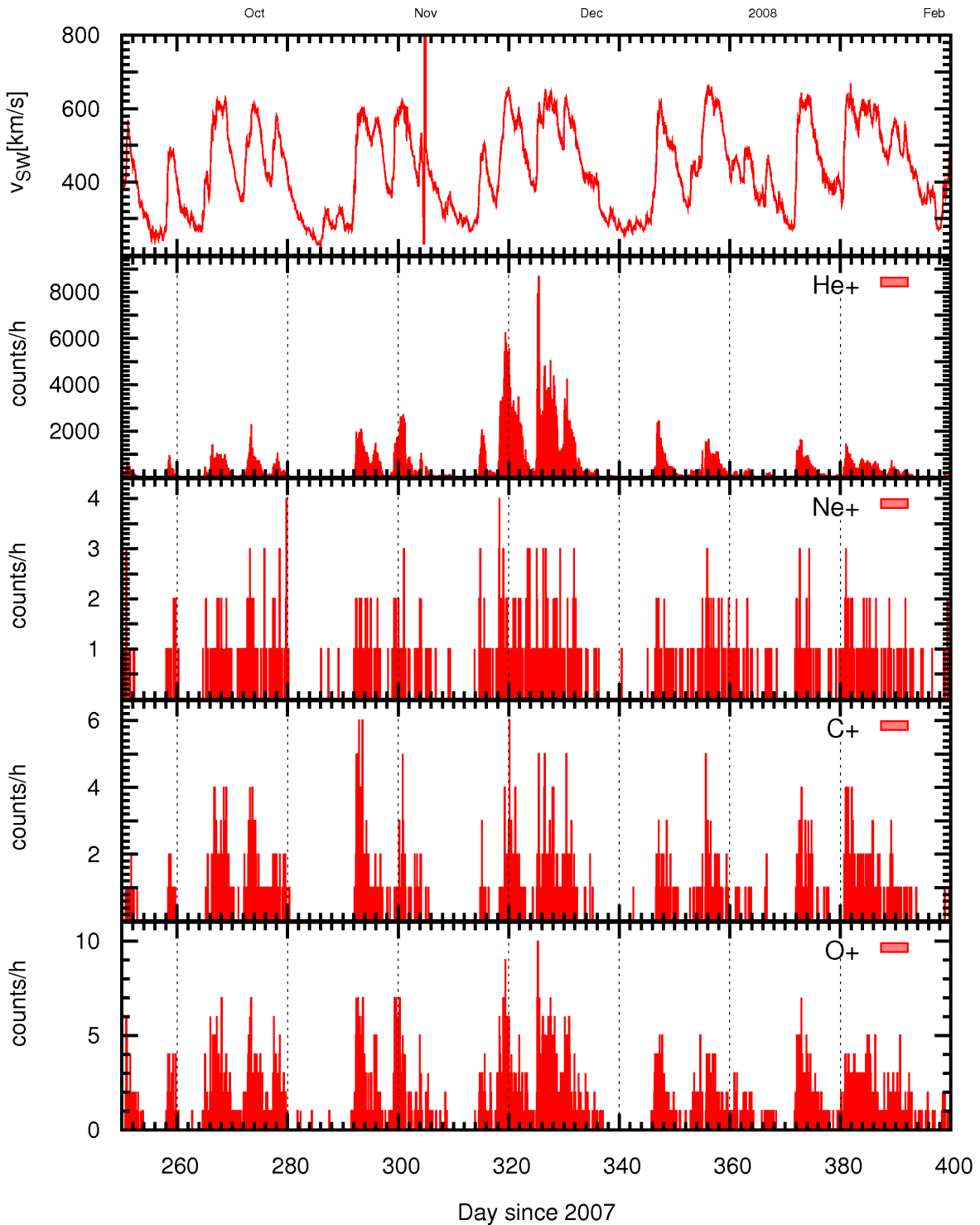


Figure 3.21: This figure shows pick-up ion count rates within the first cone transit of STEREO PLASTIC in 2007 using a time resolution of 1 hour. On the x-axis are days since 2007. The panels show from top to bottom solar wind velocity, He^+ counts, Ne^+ counts, C^+ counts and O^+ counts.

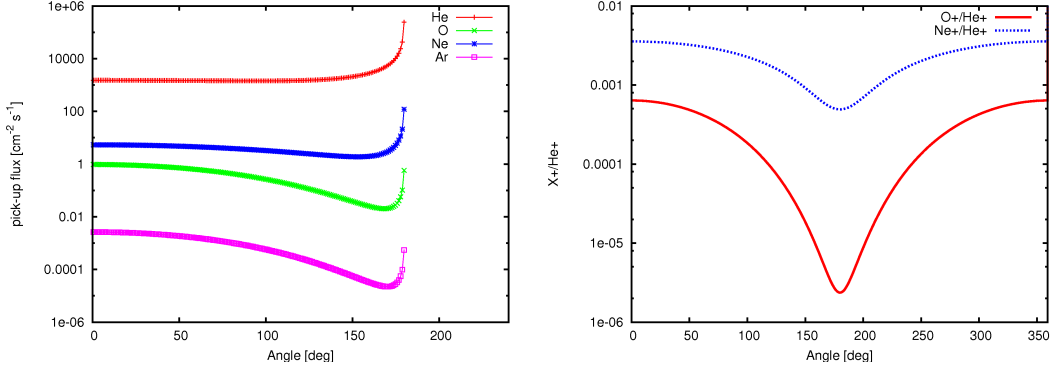


Figure 3.22: The left figure shows the angular dependence of pick-up ion fluxes for He^+ , O^+ , Ne^+ and Ar^+ at one AU. The angle is measured between the in-flow direction of the LISM and the point of observation in the ecliptic. The increase of counts at an angle of 180 degree is caused by focusing of interstellar neutrals. The right figure shows the expected ratio of O^+/He^+ and Ne^+/He^+ measured by a spacecraft orbiting the sun at one AU. The cone transit is aligned around 180 degrees. For oxygen and neon we see a depletion of counts with respect to helium, of about two orders magnitude and 0.5 respectively, in this area.

derived C^+/O^+ ratio is too high to be of interstellar origin. In addition, oxygen and carbon suffer losses by charge exchange with interstellar protons in the 100-200 AU wide filtration region beyond the heliopause [Bertaux *et al.*, 1985], which also depletes the expected count rate of interstellar O^+ and C^+ ions. On the other hand, the change of our calculated ratio Ne^+/He^+ in times of the cone transit is in rough agreement with the observed relative change of about 0.5. Thus, we suppose, that an enrichment of He^+ and Ne^+ on day 300 and 640 could be caused by gravitational focusing of interstellar neutrals, while for other pick-up species the interstellar neutrals only contribute minor fractions to the total observed count rate. This has also been suggested by *Moebius and Klecker* [2009].

3.2.4 Inner-source Pick-up Ions

Recent investigations on pick-up ions led to the idea of an inner source being only few solar radii away from the sun, an area filled with interplanetary dust particles orbiting the sun [Schwadron and Geiss, 2000]. The origin of the, so called, inner-source pick-up ions is attributed to these dust grains, which have been saturated with solar wind. Sputtering by solar radiation, energetic particles or solar wind ions then leads to disintegration of the outermost layer of a dust grain, which in turn could release solar wind particles, that were neutralized and trapped inside the grain some time before. The removed solar wind atoms are picked up by the solar wind and convected outwards, whereas the long distance between the source region and a spacecraft orbiting the sun at one AU results in a highly thermalized pick-up ion distribution. The composition of the inner-source pick-up ions is in good approximation solar, which is not surprising considering the implantation of ions, that are also of solar origin.

Subsequent work of *Wimmer-Schweingruber and Bochsler* [2002] notes, that sputtering of the outermost layer of dust grains would also lead to an enrichment of pick-up ions, that were born from dust grain material, e.g. Si or Mg. But such an enhancement has not been observed, thus other processes near the sun might be responsible for the birth of inner-source pick-up ions. *Wimmer-Schweingruber and Bochsler* [2002] assumed a population of very small interplanetary dust particles, which could have been created by collisions between dust grains with relative speeds of 10km/s. If the diameter of these dust grains is smaller than the penetration range of ions hitting the surface of a dust particle, solar wind ions would fly through it and exchange charge with the grain material. This results in a net neutralization of these ions. Afterwards they are ionized by solar radiation and picked up by the solar wind magnetic field.

Despite different explanations on the birth of inner-source pick-up ions, each ansatz produces ratios of pick-up ions comparable to the solar wind. We already assumed pick-up helium and neon to be of interstellar origin caused by inefficient ionization by solar radiation, but C⁺ and O⁺ are most likely not able to travel that far into the heliosphere to produce a distinct flux at one AU. Thus, we expect oxygen and carbon to originate from an inner source and accordingly to be of solar origin using the idea of *Wimmer-Schweingruber and Bochsler* [2002] and *Schwadron and Geiss* [2000]. From *von Steiger* [1991] we obtain for the mean ratio of carbon to oxygen in the solar wind

$$C/O = 0.70 \pm 0.11, \quad (3.14)$$

which is in rough agreement with our measured ratio of C⁺/O⁺ ≈ 0.3 ranging between 0.15 and 0.6 in 2007 and 2008. Aberrations of our derived ratio compared to results from *von Steiger* [1991] could be caused by different detection efficiencies (compare chapter 3.2.1) or different instrumental cut-offs of carbon and oxygen. While latter should have a small effect due to similar masses of carbon and oxygen, a higher detection probability of O⁺ could have resulted in a decrease of our derived ratio (see chapter 3.2.3).

An inner-source of pick-up ions caused by solar wind ions penetrating small dust grains still could not explain an enrichment of C⁺ and O⁺ in times of the cone transit. But under consideration, that our derived ratio of C⁺/O⁺ shows no distinct changes on day 300 and 640, we can at least exclude the possibility of pronounced gravitational focusing of interstellar carbon and oxygen around the sun. Thus, the observed increased count rates are likely caused by other processes.

One possible reason for this enrichment, could be gravitational focusing of interstellar

dust. Observations with the Ulysses dust detector between 3 and 5 AU and measurements by in-situ detectors on board Cassini, Galileo, and Helios were able to identify a stream of interstellar dust particles with a size of few μm inside the heliosphere [Krüger and Grün, 2008]. They move on hyperbolic trajectories and are focused around the sun, similar to interstellar neutrals. Radiation pressure and interaction with the interplanetary magnetic field, however, prevent sub- μm grains from penetrating to a distance of 5 AU [Grün et al., 1994]. Thus, we would not expect an enhancement of pick-up ions by a focused enrichment of dust grains, which were penetrated by solar wind ions. μm grains on the other hand are too large to account directly for the production of inner source PUIs. But due to fragmentation they might be the source of a population of sub- μm grains, which would show the same focusing as their source.

Such a population then could explain the observed variation of pick-up ions count rates with PLASTIC in times of the cone transit. The increased density of these sub- μm dust particles around the sun would lead to an enhanced production rate of ISPUIs, which in turn could cause an increased flux of heavy pick-up ions in these regions.

4 Outlook

Although, we were able to cover various important aspects of suprathermal pick-up ions with PLASTIC, some of our ideas could not be realized in time. In this chapter we present some unfinished work, which covers the efficiency calculation, rate data and the "virtual detector" of PLASTIC.

4.1 Detection Efficiency with PLASTIC

As mentioned in chapter 3.2, most of our work was hampered by the unknown probability for detection of solar wind ions, as it is necessary for deriving fluxes. The probability for a valid double coincidence is composed of three parts, which is the "STOP", "START" and "VALID" efficiency (see chapter 3.1.6). For triple coincidences an additional term has to be considered, that denotes the probability to trigger an energy signal in the SSD. In our investigations of pick-up ions we are solely using triple coincidences and therefore need to calculate the probability of PUIs to trigger an energy signal. The, so called energy efficiency η_E , can be derived by studying Triple Coincidence Rates (TCR) and Double Coincidence Rates (DCR) of the PHA data.

We have calculated η_E for He^+ and O^+ in the Wide Angle Partition SSD. Each particle with a related "STOP" and "START" signal will trigger an energy signal in the SSD with a likelihood of η_E . Particles without a related energy signal are assigned to an energy bin of zero. The ratio of TCR to DCR + TCR gives us the relative amount of events with a corresponding energy signal and thus is a first evaluation of the energy efficiency η_E .

$$\begin{aligned} \frac{C_{TCR}}{C_{DCR} + C_{TCR}} &= \frac{I\eta_{start}\eta_{stop}\eta_{valid}\eta_E}{I\eta_{start}\eta_{stop}\eta_{valid}(1 - \eta_E) + I\eta_{start}\eta_{stop}\eta_{valid}\eta_E} \\ &= \eta_E, \end{aligned}$$

where I denotes the flux of an ion. To obtain C_{TCR} and C_{DCR} , we fitted 1-dimensional gaussians to the O^+ and He^+ distributions for the double coincidences and 2-dimensional gaussian for the triple coincidence distributions in our long-term ET matrices. The integral of this two gaussian distribution yields C_{TCR} and C_{DCR} . This ansatz assures a small influence of background counts caused by time-of-flight pile-up (see chapter 2.5.4). Nevertheless, this ansatz was only capable of calculating the energy efficiency for a fraction of the solar wind composition, as most ions could not be resolved in the double coincidence distributions. Figure 4.1 shows our results for He^+ and O^+ together with results for He^{2+} , H^+ and Heavies, which were derived without fitting their distribution and therefore are strongly affected by high number of background counts.

For the future, we plan to derive the total efficiency η_{total} , including η_{stop} , η_{start} , η_{valid} , and η_E , for the more abundant solar wind ions and pick-up ions in the SWS, WAPSSD and WAPNOSSD. An ansatz to calculate $\eta_{stop} \cdot \eta_{start} \cdot \eta_{valid}$ is presented in chapter 3.1.6.

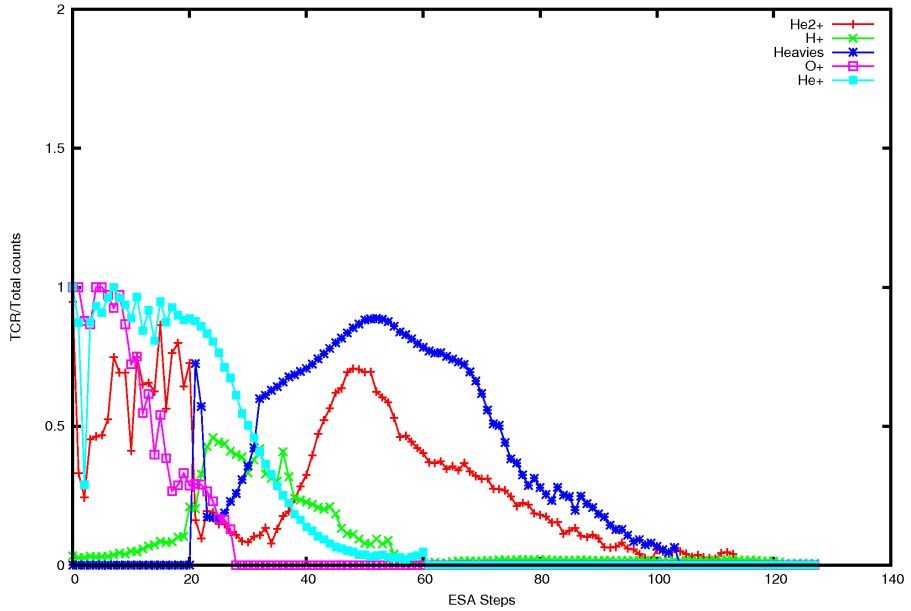


Figure 4.1: This figure shows our derived energy efficiency η_E . The y axis denotes the ratio of $C_{TCR}/C_{TCR}+C_{DCR}$ and the x axis ESA steps from 0 to 127. For each ESA step a gaussian distribution was fitted to the He^+ and O^+ distribution in our long-term ET matrices (700 days), which provides the necessary number of triple and double coincidences without a distinct influence of background counts. For other ions in this figure, we used a box rate method to obtain values for C_{TCR} and C_{DCR} .

4.2 Virtual Detector

Based on previous work of *Berger* [2008], who developed a virtual detector for ACE/SWICS, we have built a virtual detector for PLASTIC, that is able to derive spectra, as would be observed with the instrument. Due to the complexity of PLASTIC's entrance system, the virtual detector will help to understand the influence of PLASTIC's duty cycle to an observed spectrum.

For now, this model is a very basic representation of PLASTIC and does not simulate the instrument in every detail. It accounts for the instrument's different sections, geometry factors, position bins, deflection bins, energy-per-charge bins and durations of measurement. We have tested the virtual detector using core beam distributions represented by two bi-Maxwellians, which are symmetric about the magnetic field vector. This kind of distribution is common for fast solar wind protons [Marsch *et al.*, 1982] and presumably for heavy solar wind ions [Berger, 2008]. A basic example of the virtual detector is illustrated in figure 4.2. A typical core beam distribution (shown in the topmost and bottom-right panel) is used to calculate the expected spectrum for SWS, WAPSSD and WAPNOSSD (shown in the bottom-left panel).

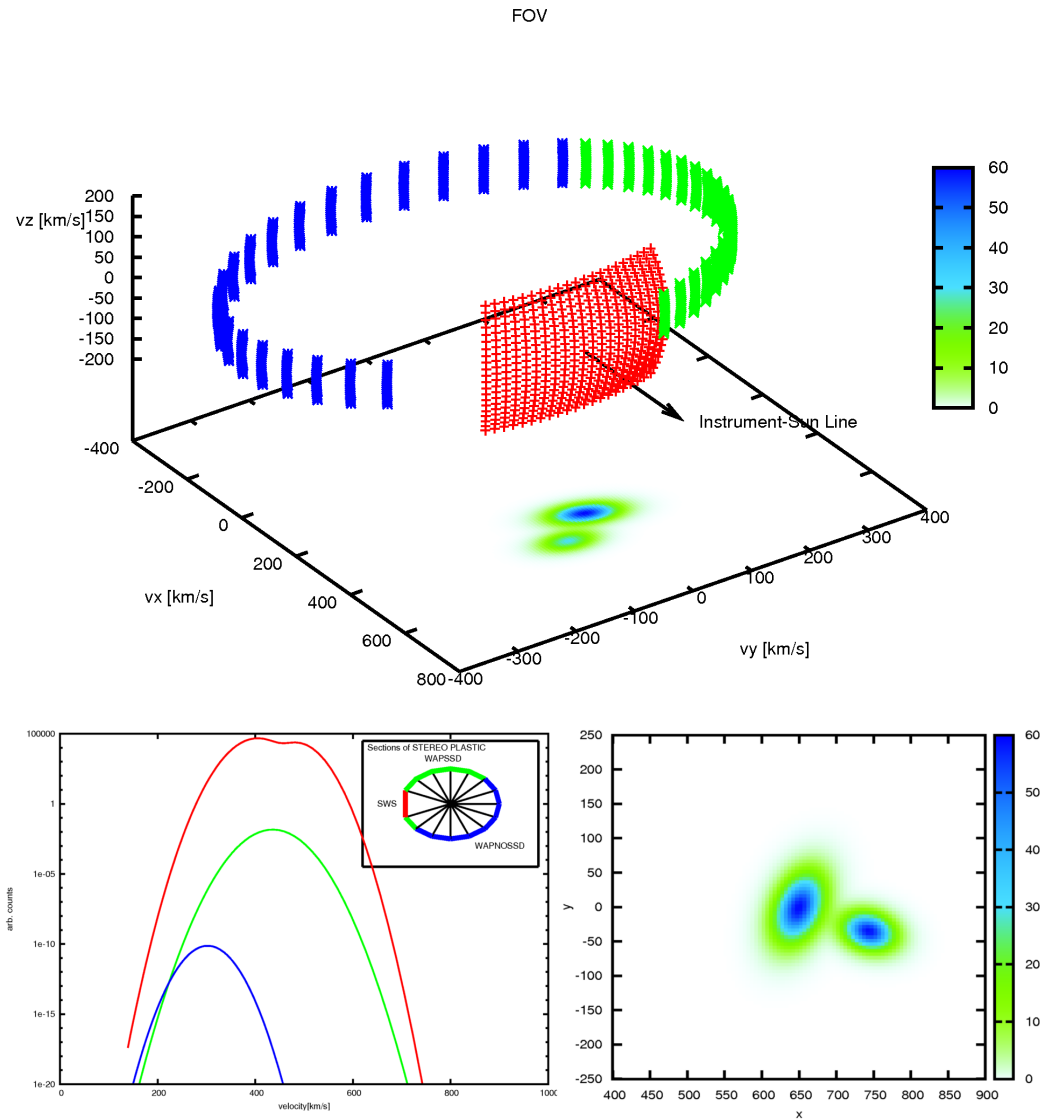


Figure 4.2: The top figure shows the acceptance range of PLASTIC's different sections (SWS (red), WAPSSD (green) and WAPNOSSD (blue)) in velocity space for an arbitrary ESA step. The $v_x - v_y$ -plane shows a cut of the velocity distribution at $v_z=0$ (also shown in the bottom right panel), whereas the real velocity distribution is a 3-dimensional one. To derive the resulting spectra in the bottom left panel, we integrate the velocity distribution along the shell-like areas representing the acceptance of PLASTIC's different sections. This was done for each ESA step with an uncertainty of $\Delta E/q=6\%$. The integration result is then transformed by PLASTIC's duty cycle into a spectrum, as observed by PLASTIC, by applying the correct measurement time and geometry factor to the corresponding ESA bin, position bin and section. The bottom left panel shows the resulting energy spectra for SWS, WAPSSD and WAPNOSSD. We note, two position bins of WAPSSD are not drawn in the topmost panel. But still, they are considered for calculations of the spectrum.

4.3 Rate Data

PLASTIC's rate data is produced on board by using m/q - m -tables. Each event is assigned to a mass and mass-per-charge given by their TOF, ESA, and SSD bin and then sorted into a corresponding box rate. Up to now, the used tables for m and m/q are based on pre-calibration calculations. Because of that, we decided not to use PLASTIC's rate data, as it could produce distinct uncertainties in m and m/q due to the usage of pre-calibration values. Nevertheless, the rate data is going to be improved by uploading new tables to the instrument, which are based upon our in-flight calibration (see chapter A.4).

For future use we have developed the necessary software to analyze PLASTIC's rate data. Their advantage is, that they are not affected by a limited telemetry as PHA data, and thus provide better statistics (see chapter 2.4). An exemplary selection of rate data is shown in figures 4.3, 4.4, 4.5 for SWS, WAPSSD and WAPNOSSD.

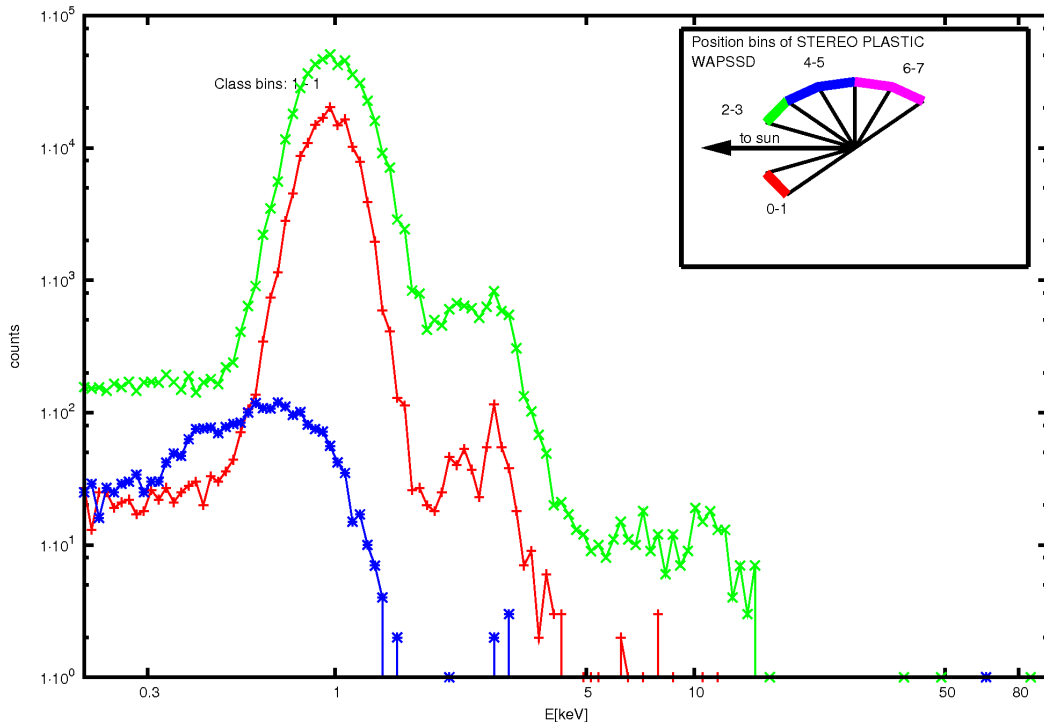


Figure 4.3: This figure shows H^+ DCR over energy for STEREO A PLASTIC - WAPSSD in a period of 3 days starting at day of year 169 in 2007. The line color is linked to different position bins of this section, which are drawn at the top right of this figure.

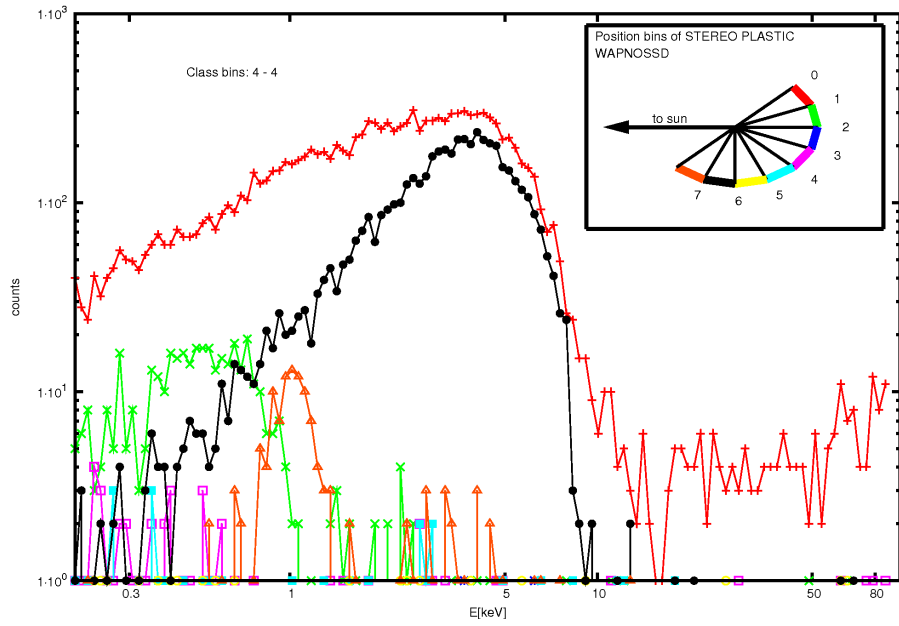


Figure 4.4: This figure shows He^+ DCR and Fe DCR over energy for STEREO A PLASTIC - WAPNOSSD in a period of 3 days starting at day of year 169 in 2007. The line color is linked to different position bins of this section, which are drawn at the top right of this figure.

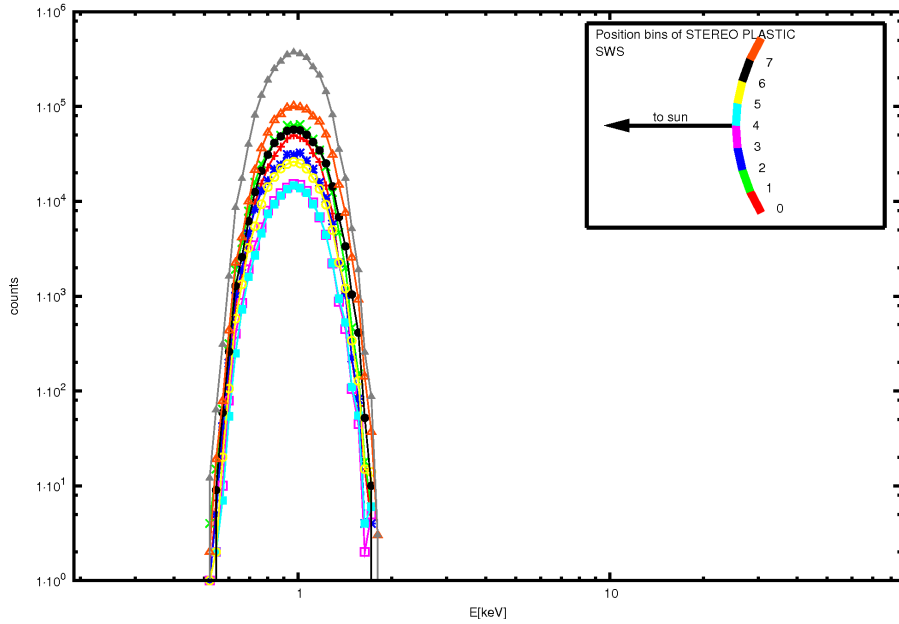


Figure 4.5: This figure shows H^+ TCR over energy for STEREO A PLASTIC - SWS in a period of 3 days starting at day of year 169 in 2007. The line color is linked to different position bins of this section, which are drawn at the top right of this figure.

5 Summary & Conclusions

In this thesis we analyzed pick-up ions at 1 AU with STEREO PLASTIC for the year 2007 and 2008 using PHA data. We showed that PLASTIC is capable of resolving the heavy pick-up ions, that is C^+ , O^+ and Ne^+ , in the PHA data. This was achieved by an analysis of long-term mass-per-charge spectra. A multi-gaussian fit, consisting of five distinct distributions for each of the heavy PUI species, was used to define ranges in mass-per-charge space that allow us to extract pick-up carbon, oxygen and neon from PHA data. The combination of PLASTIC's huge geometric factor and the current prolonged state of low solar activity, provides an ideal condition to investigate heavy pick-up ions with PLASTIC.

However, our investigations were hindered by the unknown efficiency and spectral cut-off of heavy pick-up ions. Both effects could be partially attenuated by using a combination of velocity binning and long time averages. In addition, we were able to develop a preliminary method of reconstructing missing parts of the spectrum for long-term data. This method can not be used for our investigations of short-term data and thus, we were not able to study absolute abundances of PUIs and instead analyzed their relative changes.

For our data analysis, we investigated long time series of heavy pick-up ions, i.e. carbon, oxygen and neon, and were able to identify the helium cone traversal on day 300 and 640 in 2007 and 2008. For the first time we saw that not only an enhancement of He^+ was observable in these periods, but also an enrichment of the less abundant heavy pick-up ions. Based on recent investigations on pick-up ions, summarized in *Kallenbach et al.* [2000], and an analytic approach, originally developed by *Vasyliunas and Siscoe* [1976], we concluded, that Ne^+ originates in the interstellar medium, while C^+ and O^+ most likely have its source near the sun. In addition, our observed ratio of $C^+/O^+ \approx 0.3$ seems to be in rough agreement with the solar wind value of ~ 0.7 considering the different detection probabilities of carbon and oxygen.

Recent investigations of *Wimmer-Schweingruber and Bochsler* [2002] showed, that a population of small dust particles could be responsible for the observed flux of pick-up oxygen and carbon. The dust particles may serve as a catalyst in producing inner-source pick-up ions, or be a direct source of the volatile C and O if interstellar dust grains retain enough condensed C and O, which is then liberated into the vicinity of the sun.

In the framework of this thesis we are going submit a paper to the Journal of Geophysical Research Letters (JGRL) with the title "Signatures of gravitational focusing of interstellar dust in inner-source pick-up ions?", which addresses a possible explanation of an increased pick-up carbon and oxygen count rate in times of the cone traversal. It is presented in chapter A.5 and after the co-authors acceptance ready for submission. Additionally, our developed software can be used as a basis for further data analysis with STEREO PLASTIC. It allows investigations of PLASTIC's rate data and PHA data for each section of the instrument, i.e. Solar Wind Section, Wide Angle Partition SSD and Wide Angle Partition NOSSD. In the framework of this thesis, the software was used to

perform several in-flight calibrations of the instrument.

1. We have calculated the energy efficiency η_E for He^+ and O^+ for the WAPSSD, which is necessary for the calculation of the total efficiency η_{total} . With the total efficiency it would be possible to calculate ion fluxes from raw count rates (see chapter 4.1).
2. We have calculated the expected positions of ions in the ET matrices, which is crucial in order obtain composition spectra (see chapter A.3).
3. Based on the derived ion positions, we have been able to calculate new mass and mass per charge tables for the instrument, which are used for species classification of PLASTIC's rate data. Once uploaded, the new tables will considerably improve the quality of the rate data (see chapter A.4).
4. We have developed a virtual detector, which is needed for a correct interpretation of observed spectra (see chapter 4.2).

A Appendix

A.1 Energy Conversion

SSDID j	X _A	Y _A	Z _A	X _B	Y _B	Z _B
0	1	2.276	-0.838	2	2.16	-21.06
1	5	2.302	8.09	1	2.13	-23.2
2	2	2.291	1.429	0	2.24	-26.29
3	3	2.263	3.738	0	2.09	-24
4	5	2.235	7.495	2	2.19	-20.27
5	7	2.227	12.909	4	2.16	-17.49
6	4	2.225	5.283	2	2.13	-20.46
7	3	2.214	4.03	2	2.14	-19.95
8	8	2.211	14.252	7	2.09	-10.66
9	4	2.16	-6.74	6	2.1	-12.87
10	2	2.219	0.977	4	2.01	-14.73
11	6	2.22	10.795	3	2.11	-19.02
12	4	2.223	5.155	1	2.18	-23.17
13	4	2.223	5.014	5	2.09	-15.13
14	0	2.269	-3.128	4	2.24	-18.14
15	0	2.357	-2.912	0	2.24	-25.56

Table A.1: Table of energy conversion factors for STEREO A/B.

Using the tabel above, one can derive the residual energy of an event for each SSD pixel and spacecraft by using the following equation

$$E_{i,j} = (SSD_{i,j} - X_{i,j}) \cdot Y_{i,j} + Z_{i,j}, \quad (\text{A.1})$$

where i stands for the instrument "A" or "B", j for the SSD pixel number, SSD for the SSD bin and X, Y, Z for the corresponding conversion factors. The resulting residual energy is in units of keV.

A.2 MCP Bias

DATE	MCP VOLTAGE [kV]	DATE	MCP VOLTAGE [kV]
02.01.07	2.556	13.04.08	0
31.01.07	2.635	15.04.08	1.4
02.02.07	2.763	16.04.08	2.64
06.02.07	2.788	17.04.08	2.92
07.02.07	2.763	26.01.09	2.94
08.02.07	2.695	16.02.09	2.96
17.04.07	2.843	31.03.09	2.985
13.06.07	2.915	-	-

Table A.2: Changes of MCP voltage for STEREO A from the PLASTICs command logs.

DATE	MCP VOLTAGE [kV]	DATE	MCP VOLTAGE [kV]
01.01.07	2.600	18.11.08	3.180
29.01.07	2.720	26.11.08	3.200
03.04.07	2.776	-	-
10.04.07	2.900	-	-
12.04.07	2.966	-	-
01.05.07	3.040	-	-
08.05.07	3.110	-	-
05.12.07	3.159	-	-

Table A.3: Changes of MCP voltage for STEREO B from PLASTICs command logs.

A.3 Ion Positions in ET Matrix

As a prerequisite for our analysis on heavy pick-up ions, it was necessary to derive the theoretical TOF and SSD bin positions for each ion in the ET matrices. The ion positions allow us to assign PHA words to corresponding ions. From this we can derive energy spectra, that are needed for the calculation of solar wind properties (see chapter 2.5.4).

The ion positions in the ET matrices will be of great use for further analysis on composition spectra, especially for the case of adjacent ions, that can not be resolved by applying box rates. Instead one can fit multiple distributions to the PHA data using our derived ion positions to sustain information on the composition, even for ions that are only separated by a few TOF and SSD channels.

In addition, we were able to perform an in-flight calibration of the instrument by adjusting the pre-calibration mass and mass-per-charge algorithms to our derived ion positions, which will considerably improve the quality of PLASTIC's rate data (see chapter A.4).

A.3.1 TOF Position

The first step is to invert equation 2.3 to get an expression for the time-of-flight and residual energy in dependence of mass and mass-per-charge. We get

$$\tau_{ns} = \sqrt{\frac{m}{2q} \cdot ((E/e + V_{PAC}) \cdot \alpha(E, m)) \cdot d}, \quad (\text{A.2})$$

where τ_{ns} is the time-of-flight in nano seconds, m the ion mass, q the ion charge state, $\alpha(E, m)$ the percental energy loss in the carbon foil, d the time-of-flight path, E/e the energy-per-charge and V_{PAC} the post acceleration voltage. The only parameter that is unknown is $\alpha(E, m)$. To obtain the parameter $\alpha(E, m)$ we used SRIM (the Stopping and Range of Ions in Matter, developed by James F. Ziegler) to simulate the differential energy loss of ions in PLASTIC's carbon foil. SRIM accounts for interaction of particles with the material's nucleus and electrons, while we use a combination of both for our calculations. We assumed a carbon foil density of $3.5 \mu\text{g}/\text{cm}^2$ and a thickness of 144\AA . The differential energy loss was simulated for all common solar wind ions up to iron. An example of the simulated differential energy loss for O^{6+} is presented in figure A.1.

We then need to derive the total energy loss in PLASTIC's carbon foil. For that, we use the simulated differential energy losses to integrate over the foil thickness in steps of one \AA . This was done for all major solar wind ions. By calculating the ratio of the initial ion energy and the energy after the carbon foil passage, we obtain the energy and species dependent parameter

$$\alpha(E, m) = \frac{E(m, E/q, d_{foil} = 144 \text{\AA})}{E(m, E/q, d_{foil} = 0 \text{\AA})},$$

where $E(m, E/q, d)$ is the energy of a particle with mass m , energy-per-charge E/q , and a depth of penetration d .

With the derived parameter $\alpha(E, m)$ and equation A.2 we are now able to calculate the expected TOF channel of incident ions,

$$\tau_{ns} = \tau_{slope} \cdot \tau_{chn} + \tau_{off} \quad (\text{A.3})$$

$$\Rightarrow \tau_{chn} = \frac{\sqrt{\frac{m}{2q} \cdot ((E/e + V_{PAC}) \cdot \alpha(E, m)) \cdot d} - \tau_{off}}{\tau_{slope}}. \quad (\text{A.4})$$

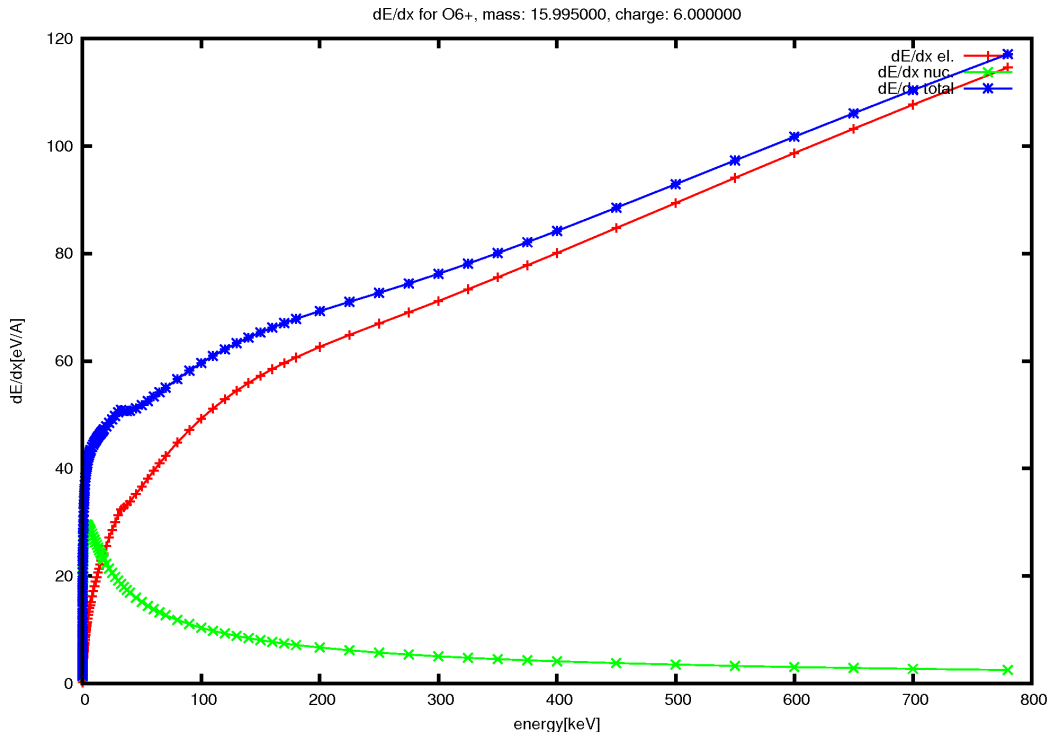


Figure A.1: This figure shows the differential energy loss of O^{6+} in carbon as a function of the total energy. The red curve denotes energy loss caused by electrons and the green curve by nucleus interaction, while the blue curve is the sum of both contributions.

Values for $\tau_{off} = 1.3$ and $\tau_{slope} = 0.25$ were derived in the pre-calibration phase of the instrument. Nevertheless, we had to adjust the parameter τ_{off} to achieve a good correlation between our derived TOF positions and peak positions in the PHA data. We note, that other factors have to be considered for a precise determination of the TOF positions. Especially the time-of-flight slope and conversions for energy-per-charge are also based upon pre-calibration values. But we found, that a constant shift of 4.2 ns is sufficient for an approximation of the TOF positions.

With equations A.2 and A.3 we are able to calculate the correct time-of-flight positions for every ion up to iron. They are presented in figures A.3 and A.4.

A.3.2 SSD Position

In order to derive the SSD position of incident particles we used the derived parameter $\alpha(E, m)$ to calculate the residual energy of ions after their carbon foil passage.

$$E_{res} = (E/e + V_{PAC}) \cdot \alpha(E, m) \quad (\text{A.5})$$

E_{res} then has to be multiplied with $\beta(E, m)$, the Pulse Height Defect (PHD) of the solid state detector. $\beta(E, m)$ denotes the percental fraction of the residual energy, that will be measured by the SSD.

$$E_{SSD} = \beta(E, m) \cdot E_{res} \quad (\text{A.6})$$

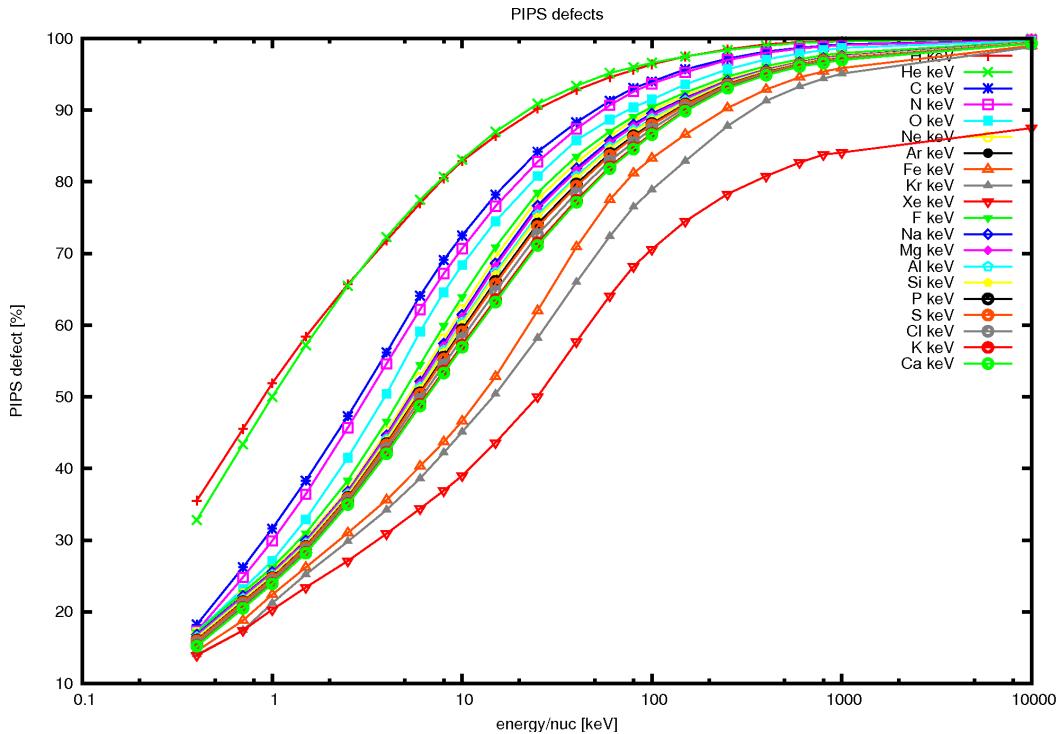


Figure A.2: This figure shows Pulse Height Defects for different ions, that were used for the calculation of E_{SSD} . The y-axis denotes the percental fraction of measured particle energy in the SSD and the x-axis denotes incident energy of particles. For H, He, C, N, O, Ne, Ar, Fe, Kr, X values from *Kötén* [2005] are used, while the remaining are the result of a linear interpolation in mass.

To obtain $\beta(E, m)$, one could use the derived values from pre-flight calibration, which were not available at the time. Instead, we use in-flight calibrated values for $\beta(E, m)$ from ACE/SWICS [*Kötén*, 2005] and applied them to PLASTIC. This is a reasonable step, as both the SSDs for SWICS and PLASTIC are CANBERRA Passivated Implanted Planar Silicon (PIPS) detectors, which presumably results in similar (but still not identical) characteristics of the dead layer, leakage current and noise. Thus, it is necessary to adjust the results from SWICS by a correction factor in order to fit PLASTIC's SSDs. To be precise, one would have to make this adjustments for each of PLASTIC's sixteen SSDs separately, because they all have different detector properties. But as our long term data is averaged over all SSD pixels and our ion positions are based upon that, it is presumably sufficient to calculate an averaged correction factor over all SSD pixels. The results of the SWICS pulse height defect values from *Kötén* [2005] are presented for H, He, C, N, O, Ne, Ar, Fe, Kr, X in figure A.2. To obtain information on the PHD of other ions we used a linear interpolation in mass between these ions, which seems to be a good approximation and is also shown in figure A.2 for F, Na, Mg, Al, Si, P, S, Cl, K, Ca. We find that a constant correction factor of -4.2 percent applied to PHD_{ACE} fits the PLASTIC data well. It was derived by comparing the SSD channel position for He^{2+} , O^{6+} , H^+ , and He^+ obtained from long-term ET matrices with the calculated ones using PHD_{ACE} .

The last step is to convert the derived SSD energy into a corresponding SSD channel, which should be done by using table A.1, but as our calibration data is averaged over all sixteen SSD pixel we couldn't use the precise energy conversion and instead used

$$E_{chn} = E_{SSD} \cdot 0.45 + 2.9,$$

which was obtained from table A.1 averaging the conversion factors for pixel 4 and 5 of STEREO A, as they are the best responding SSD pixels. The resulting SSD channel positions are presented in figures A.3 and A.4 together with the TOF channel positions.

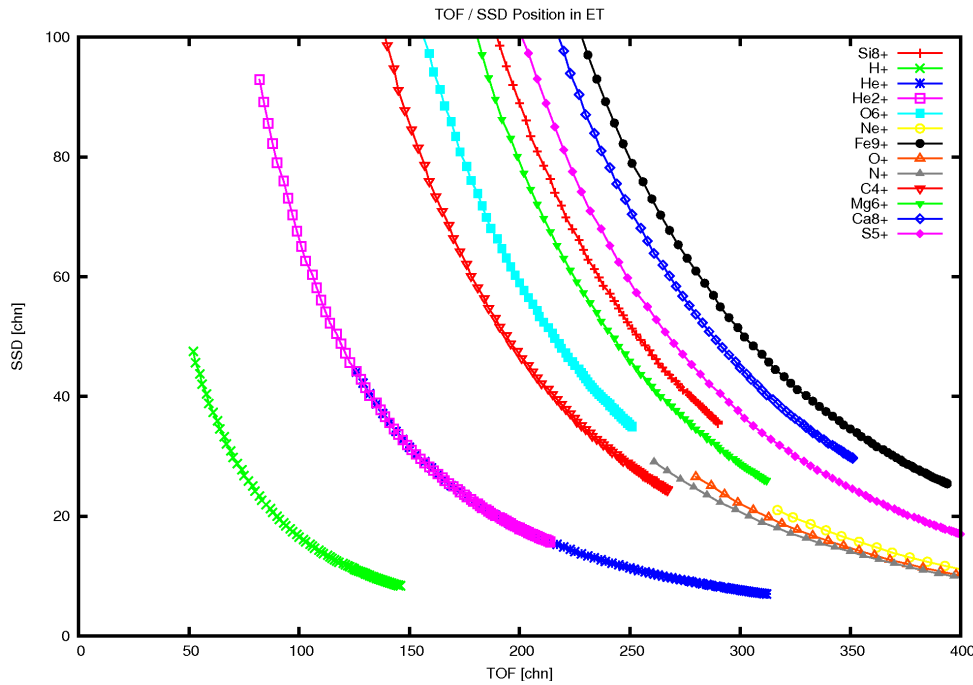


Figure A.3: This figure shows our derived ion positions in the ET matrix for various ions, where each point of the same color stands for a different ESA step ranging from 0 (top-left data points) to 128 (bottom-right data points).

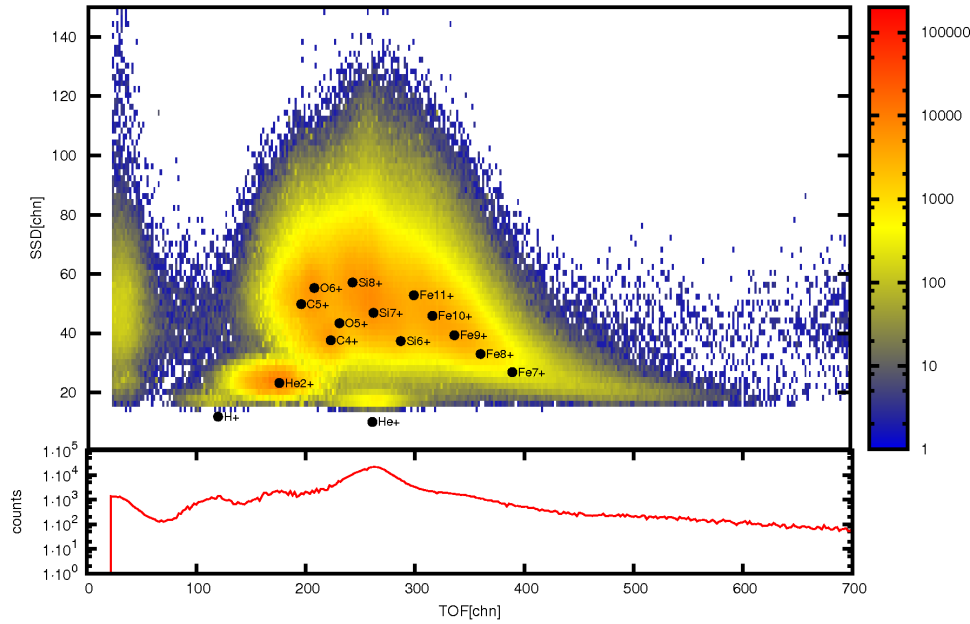


Figure A.4: This plot shows an ET matrix of ESA step 46 together with our ion positions. Our positions seem to fit the data well.

A.4 PLASTIC In-Flight Calibration

PLASTIC's rate data is defined by rectangular boxes in mass and mass-per-charge space, which means, that any event, falling into one of the rate boxes, is linked to the corresponding rate (e.g. the O⁶⁺ rate is defined as a box in m over m/q space, that is roughly centered around $m=16$ and $m/q=16/6$). The rates then do not contain any information on the SSD or TOF channel of incident events, but rather provide accumulated counts sorted by time bin, ESA step, deflection bin, position bin and species, whereas the actual bin width for each information can differ depending on the species [Kistler and Ellis, 2007].

To assign incident ions to their corresponding rate, PLASTIC makes use of, so called, look-up tables, which provide mass and mass-per-charge for every combination of TOF, ESA bins and TOF, SSD bins respectively. These tables are calculated on ground and can be sent to the instrument if required. The currently used tables are based upon pre-calibration calculations and have not been changed since. As a result, the currently used look-up tables produce incorrect mass and mass-per-charge values from TOF, SSD and ESA bins. Thus, the m and m/q distribution are shifted and are not well covered by their corresponding rate box anymore. In order to improve the quality of PLASTIC's rate data, we calculated new look-up tables for the instrument based upon our derived ion positions, which will provide the correct mass and mass-per-charge of measured events.

A.4.1 Mass per Charge Table

The new m/q tables are calculated by an algorithm, which is based upon the pre-calibration algorithm

$$\begin{aligned} V_{PAC} &= 19.7 \\ E/q &= 0.2 \cdot 1.048954246^{128-ESA} \\ c1 &= \frac{(4.38e7)^2}{(1e9)^2 d^2} \\ \tau_{ns} &= \tau_{slope} \cdot \tau_{chn} + \tau_{off} \end{aligned}$$

$$m/q = c1 \cdot (V_{PAC} + E/q - 2) \cdot \tau_{ns}, \quad (\text{A.7})$$

with $\tau_{off}=1.3$ and $\tau_{slope}=0.25$. This algorithm is independent from the particle mass and thus, does not account for the species and energy dependent parameter $\alpha(E, m)$. As a result, equation A.7 calculates the mass-per-charge of PHA events without the consideration of the particles' energy loss in PLASTIC's carbon foil, which ultimately results in an incorrect m/q assignment.

To improve the m/q tables, we decided to implement the mass dependency in form of an ESA dependent offset τ_{off} . In order to derive this time-of-flight offset, we first created m/q over time-of-flight sequences for each ESA step based upon our ion positions. These sequences were then fitted with a modified version of the mass-per-charge algorithm from equation A.7. We used a time-of-flight slope τ_{ns} of 0.2373 and chose $\tau_{off}(ESA)$ to be the free parameter of our fit. The fit results are shown in figure A.5.

From the fitted sequences we obtained the ESA dependent parameter τ_{off} , which was

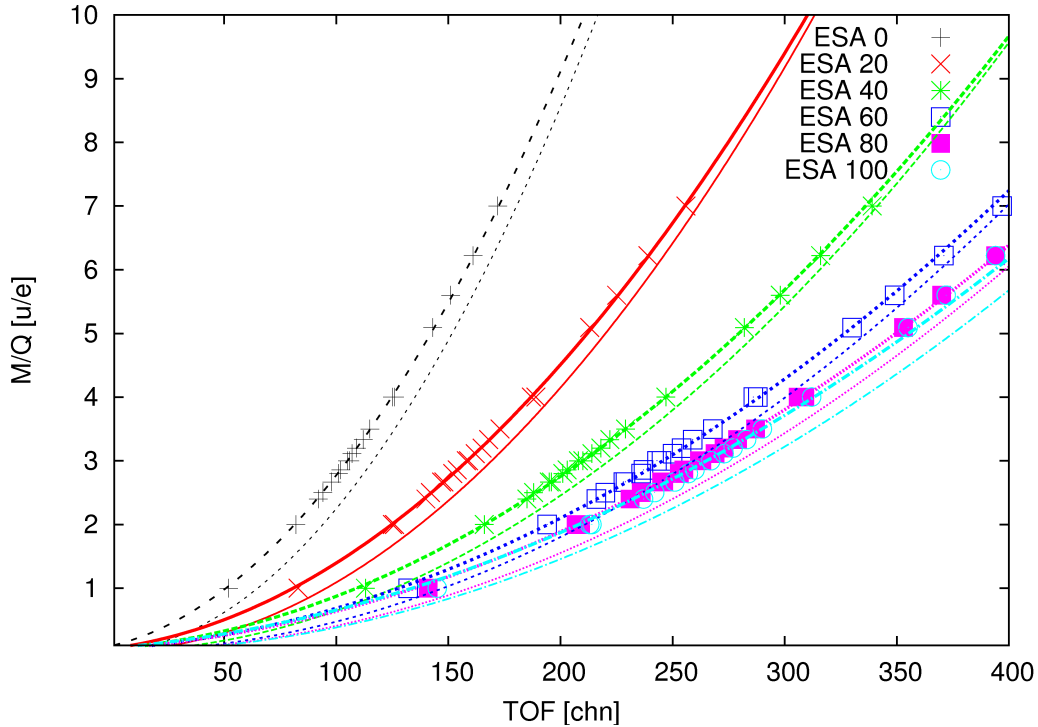


Figure A.5: This figure shows m/q over time-of-flight sequences for different ESA steps based upon our derived ion positions. The data points, which denote our calculated ion positions for H^+ , He^+ , He^{2+} , C^+ , C^{4+} , C^{5+} , C^{6+} , O^+ , O^{5+} , O^{6+} , Ne^+ , Ne^{5+} , Ne^{6+} , Ne^{8+} , Mg^{8+} , Mg^{9+} , Si^+ , Si^{8+} , Si^{9+} , Si^{10+} , Fe^{8+} , Fe^{9+} , Fe^{10+} , Fe^{11+} , are fitted by a modified mass-per-charge algorithm used in the instrument, resulting in an ESA dependent time-of-flight offset τ_{off} . The thicker curves show our fit results created with the new algorithm, while the thinner curve denotes the currently used algorithm on the instrument. The new algorithm reproduces the observed positions considerably better, while the old one deviates up to 20 channels, which results in an incorrect assignment of events to the rate data. We have to point out, that our algorithm is optimized for ESA 0 to 100. Above ESA step 100 it still might produce incorrect mass-per-charge values for protons and alphas in the slow solar wind.

then fitted with a power-law function

$$f(x) = a \cdot ESA^b + c, \quad (\text{A.8})$$

with the resulting fit parameters $a=0.00574698$, $b=1.47412$ and $c=5.5$ (see figure A.6). Using the expression from equation A.8 for τ_{off} and a time-of-flight slope $\tau_{slope}=0.2373$ for the m/q algorithm A.7, then allows to account for the species and energy dependent parameter $\alpha(E, m)$. To illustrate the improvement compared to the old $m-m/q$ tables, we present a mass and mass-per-charge matrix, which was calculated by our new algorithm in figure A.8.

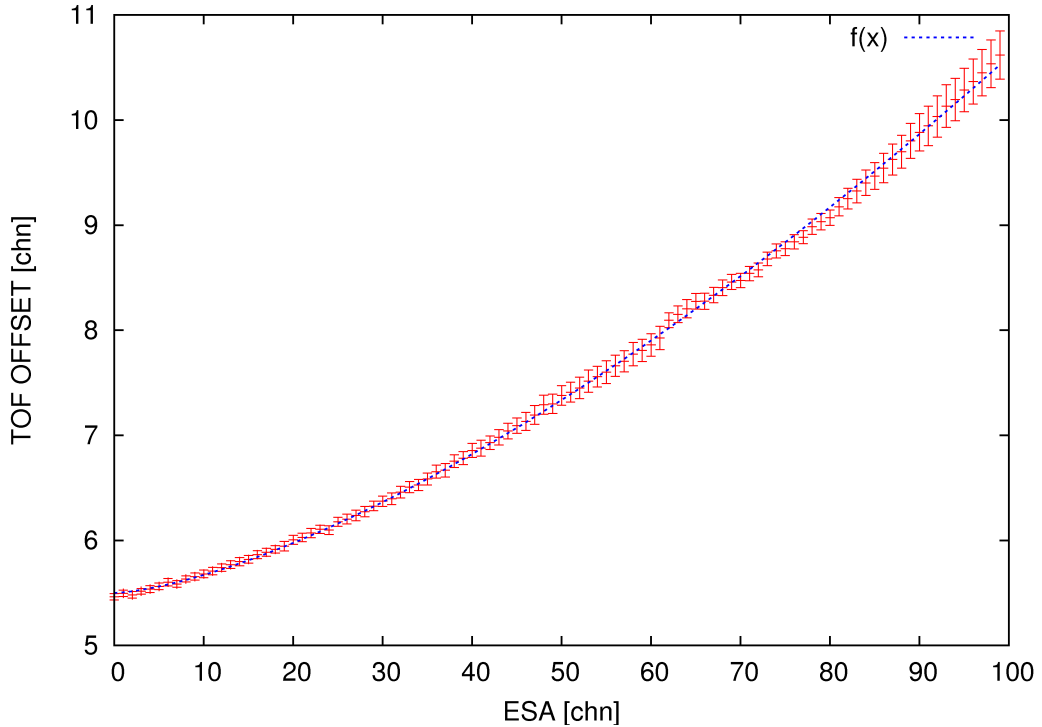


Figure A.6: This figure shows our derived time-of-flight offsets for each ESA step in red and the resulting power-law fit function in blue.

A.4.2 Mass Table

The mass table for the instrument was derived by *Berger* [2009]. It was created using a non-linear interpolation between the TOF/SSD sequences of different species in figure A.3.

A.4.3 Discussion

Our new algorithms for mass and mass-per-charge will considerably improve the quality of PLASTIC's rate data. As a demonstration of this improvement we have converted long-term PHA data using both the pre-calibration and our new algorithm. The results for ESA step 20 are shown in figures A.7 and A.8 together with a selection of rate boxes. In figure A.7 one can see that the distributions of He^+ , O^+ , He^{2+} , and Fe^{7+-9+} are not centered inside the corresponding rate box. Thus, the rate boxes miss a large fraction of counts. The fact that the distributions are shifted towards smaller m and m/q also results in a large contribution to adjacent rate boxes, as seen for He^{2+} and ${}^3\text{He}^{2+}$.

Our new algorithm, however, accounts for the energy and species dependent energy loss in PLASTIC's carbon foil. As a result, the distributions of He^+ , O^+ , He^{2+} and Fe^{7+-9+} are well centered inside their corresponding rate boxes. Also, contributions of adjacent ions to the rate boxes are decreased, as seen for He^{2+} .

Nevertheless, we have to note that even with the new algorithm the box rates are still polluted by adjacent ion distribution (see He^{2+}). This, however, is due to PLASTIC's confinement to rectangular boxes for the rate classification. The boxes are defined by

an upper/lower limit of mass and mass-per-charge and thus, are aligned along the m and m/q direction in figures A.7 and A.8. The ion distributions on the other hand are aligned along the TOF and SSD channel directions in figure A.4, which causes the ion peaks to be skewed in mass and mass-per-charge space. As a result, the definition of the rate boxes becomes significantly more difficult, as one has to make a compromise between the distribution coverage and pollution of adjacent ions.

Nevertheless, it is planned to upload the improved look-up tables for STEREO A (and later for STEREO B).

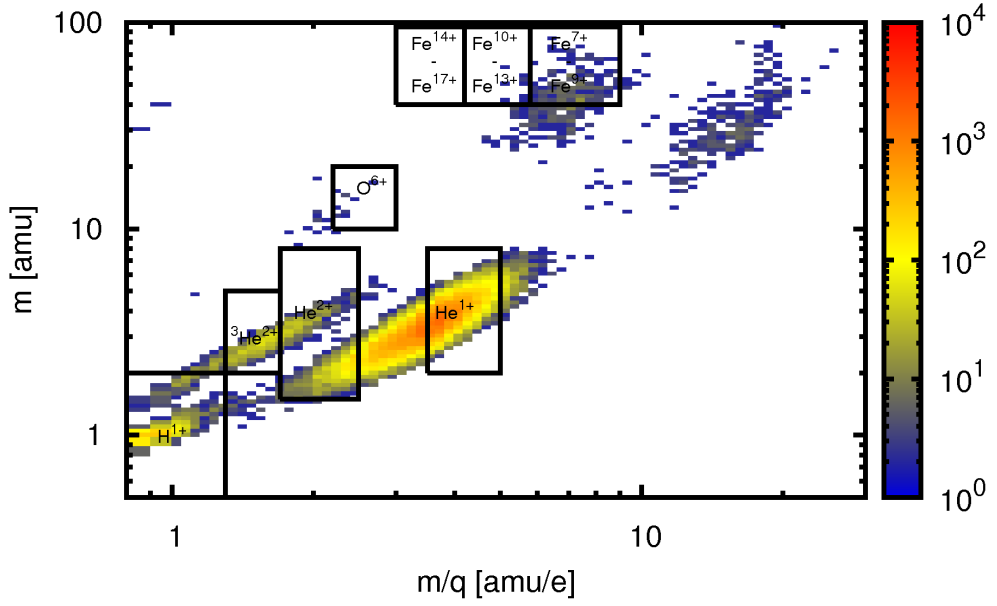


Figure A.7: This figure shows a m over m/q matrix of PHA words in a period of 700 days for STEREO A - ESA 20. The calculation of m and m/q was done with the pre-flight algorithms, currently used for the flight-model. Box rates for several ions are shown. They are used to assign a species to each measured event. This figure was taken from Berger [2009].

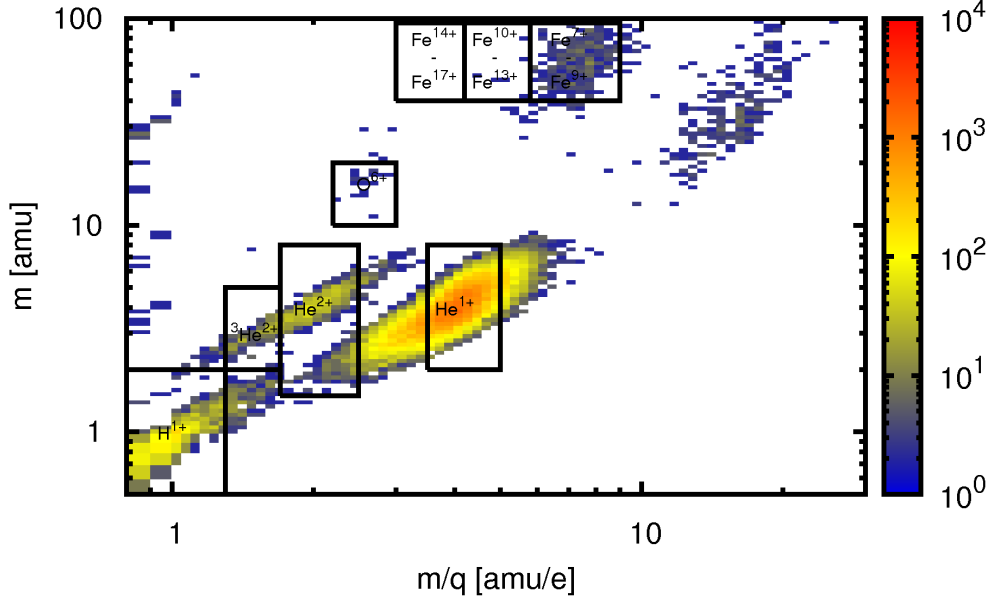


Figure A.8: This figure shows a m over m/q matrix of PHA words in a period of 700 days for STEREO A - ESA 20. The calculation of m and m/q was done with the new in-flight calibrated algorithms. Box rates for several ions are shown. They are used to assign a species to each measured event. This figure was taken from Berger [2009].

A.5 Geophysical Research Letters Submission

Signatures of gravitational focusing of interstellar dust in inner-source pick up ions?

Christian Drews¹, Lars Berger¹, Robert F. Wimmer-Schweingruber¹, Antoinette B. Galvin², Berndt Klecker³, Eberhard Möbius²

Previous work [e.g. *Gloeckler et al.*, 2004] has shown that pickup ions in the heliosphere are either of interstellar or solar wind origin. Because interstellar neutral He is focused by the gravitation of the Sun, count rates of interstellar He pickup ions show a distinctive peak when the observer has the Sun between himself and the interstellar inflow direction. Using the large geometric factor of the PLAsma and SupraThermal Ion Composition (PLASTIC) instrument on the Solar TErrestrial RElations Observator (STEREO) mission, we have clearly identified this so-called He focusing cone. Remarkably, not only He⁺ pickup ions are enhanced during these periods, but we also measured clear enhancements of C⁺ and O⁺ pickup ions during passage of the focusing cone. This is not expected for interstellar C and O and, indeed, the C/O ratio does not change appreciably across these time periods. Therefore, we argue, these enhancements are due to enhanced production of inner-source pickup ions, possibly by the gravitational focusing of interstellar dust particles.

1. Introduction

Observations of singly-charged ions with abundances similar to but still distinct from those of the solar wind [*Gloeckler and Geiss*, 1998; *Gloeckler et al.*, 2000] have been interpreted as due to an inner source of pickup ions close to the Sun [*Schwadron et al.*, 2000]. In this picture, the solar wind is absorbed by dust particles close to the Sun and later re-emitted as atoms, singly-charged ions, or even molecules. The peak production of such inner-source pickup ions appears to lie between about 10 and 20 solar radii from the Sun [*Schwadron et al.*, 2000]. The process of re-emission is unclear, especially the contribution by sputtering has been contested[*Wimmer-Schweingruber and Bochsler*, 2003]. The freshly created ions are picked up by the solar wind and convected outwards where they can be discerned from ordinary solar wind ions by their non-thermal velocity distributions and by their low charge states.

There exists also an other “inner source” of pickup ions, but only for elements with a long ionization time. Interstellar atoms (in this case mainly He and Ne) can enter the heliosphere unimpeded by the turbulent magnetic field in

the heliosheath and outer heliosphere. Once close to the Sun, they are ionized, picked up and can again be observed as singly charged ions [*Möbius et al.*, 1985; *Gloeckler et al.*, 1998]. Because of the relatively low relative speed between heliosphere and the local interstellar medium, the trajectories of atoms are focused behind the Sun, leading to an enhancement in the production rate of pickup ions, termed the “focusing cone” [e.g. *Möbius et al.*, 1985; *Gloeckler et al.*, 2004]. This focusing does not act on interstellar hydrogen because the solar photon pressure more or less counter-acts gravitation.

Here, we report observation of inner-source pickup ions with the PLAsma and SupraThermal Ion Composition (PLASTIC) instrument [*Galvin et al.*, 2008] on the Solar TErrestrial RElations Observatory (STEREO) [*Kaiser et al.*, 2008] mission. STEREO consists of two spacecraft, A and B, one moving ahead (A) of the Earth, and one behind (B) at an angle increasing by roughly 22° per year. PLASTIC is a time-of-flight mass spectrometer which, by a combination of electrostatic deflection, time-of-flight and total energy measurement, measures the kinetic energy, mass and charge of heliospheric ions. It has a large geometric factor which makes it especially well-suited for the investigation of rare inner-source pickup ions. We used the Solar Wind Section (SWS) of PLASTIC for our analysis which provides a field of view of 45° in the ecliptic and ± 20° in the polar direction, and is centered on the Sun-Earth line.

Currently the Sun is in an unusually prolonged state of low activity, resulting in a very simple structure of the inner heliosphere dominated by the interaction of high-speed streams from coronal holes and slow solar wind. Since early 2007, we have been observing a more or less regularly recurring patter of alternating high-speed streams and slow wind. This period is ideal for our studies of inner-source pickup ions because it is nearly entirely free from interplanetary coronal mass ejections (ICMEs) which show occasional enhancements of low charge states of heavy ions [e.g. *Gloeckler et al.*, 1999]. Indeed, only 8 ICMEs were observed in-situ at STEREO from January, 2007 to August, 2008 which ensures a very clean interplanetary background for observing pickup ions.

2. Data Analysis

We used PLASTIC Pulse Height Analysis (PHA) words to determine the energy, mass, and mass-to-charge ratio of heavy pickup-ions, mainly C⁺, N⁺, O⁺ and Ne⁺, as well as heavier ions, such as Mg⁺, Si⁺, S⁺. The PHA words provide the full measurement information, energy per charge, E/q , time of flight, τ , and residual energy E_{res} measured in the solid-state detectors [*Galvin et al.*, 2008]. As PLASTIC steps down through its E/q range beginning at $E/q \sim 80\text{keV}/e$, heavy pickup ions are well separated from the solar wind because of their single charge and the fact that all ions in the solar wind flow at roughly the same speed. Because pickup ions are rare, we have limited ourselves to a time resolution of 1 hour or longer.

¹Institute for Experimental and Applied Physics,
Christian-Albrechts-University zu Kiel, Germany

²Space Science Center & Department of Physics,
University of New Hampshire, New Hampshire

³Institute for Experimental and Applied Physics,
Christian-Albrechts-University Kiel, Germany

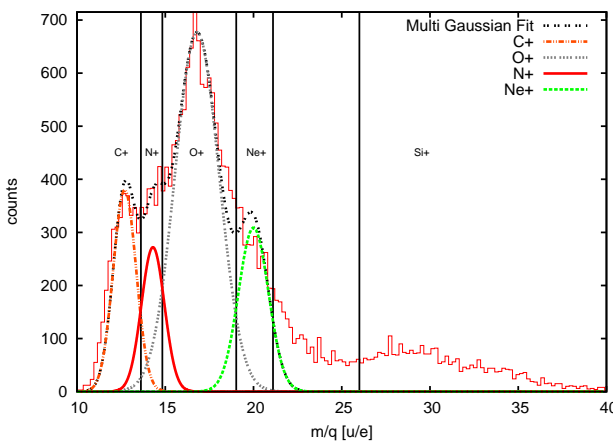


Figure 1. Mass-per-charge (m/q) spectrum of heavy pick up ions measured with PLASTIC on STEREO A during a period of 700 days. The x-axis shows mass per charge and the y-axis raw counts. All events are sorted into m/q bins with a width of 0.4 amu/e. The contributions of C^+ , O^+ , N^+ , Ne^+ (colored curves) are determined by a fit of 4 Gaussians (black curve). Based upon this fit, we defined m/q ranges (black vertical lines), for the corresponding ions, of which only C and O are used in this work.

In Fig. 2 we present a time series of count rates of heavy PUIs with $m/q < 21$ for STEREO A in a period of two months. Counts were accumulated over eight hours to ensure adequate statistics. A strong correlation with the solar wind velocity, caused by the energy and species dependent detection probability (efficiency) can be seen. In fast solar wind streams, ions have a higher kinetic energy and thus have a higher chance of triggering a valid event. In slow solar wind streams the probability of triggering a valid event decreases proportionally to the particle's mass and energy. This systematic effect introduces a bias into our measure-

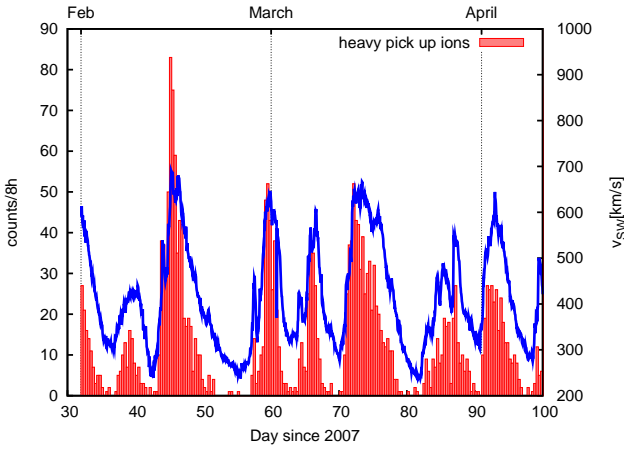


Figure 2. A time series of 8-hour count rates of heavy pick up ions with $m/q < 21$ is shown (red). The blue curve shows the corresponding proton bulk velocity time series. Count rates are strongly correlated with solar wind speed as no efficiency correction has been applied for this Figure.

ments that can be corrected for by applying an efficiency function that is available for several ions based on pre-flight beam calibrations. However, in actual flight conditions, we must also compensate for the aging of the Micro Channel Plates (MCP) that leads to a decrease in detection efficiency for the time-of-flight measurements. This gain decrease is periodically compensated for by adjusting the MCP bias voltage, and this makes the overall efficiency function time-dependent and complicated. We therefore pursue the approach discussed below for the corrections. Apart from the velocity correlation one also notices an enrichment of counts at the leading edges of high-speed streams which is most likely caused by the compression of the solar wind (see days 45, 60, 72 and 93 in Fig. 2).

Figure 1 demonstrates that different species of heavy PUIs can be resolved, especially carbon and oxygen (and He, not shown), upon which this work is based. The m/q classification is based on the time-of-flight measurement which in turn is sensitive to the energy lost in the thin carbon foil used in PLASTIC to trigger the start signal of the time-of-flight measurement. To predict the observed m/q bin of different heavy PUI species, we simulated the species- and energy-dependent energy loss, $\alpha(E, m)$, in PLASTIC's carbon foil for C^+ , O^+ , N^+ and Ne^+ and calculated the resulting mass per charge by equation (1). Results are presented in table 1.

$$\frac{m}{q} = 2(E/e + V_{PAC}) \alpha(E, m) \left(\frac{\tau}{d}\right)^2, \quad (1)$$

Table 1. Expected m/q bins after energy loss in carbon together with $\Delta m/q$, which denotes the absolute uncertainties of our calculation. Species classification is achieved by defining an upper/lower limit of m/q for the respective ion.

Ion	m/q [u/e]	$\Delta m/q$ [u/e]	m/q_l	m/q_u
C^+	12.7	x	10.0	13.7
N^+	14.3	x	-	-
O^+	16.8	x	14.7	19.2
Ne^+	20.0	x	-	-

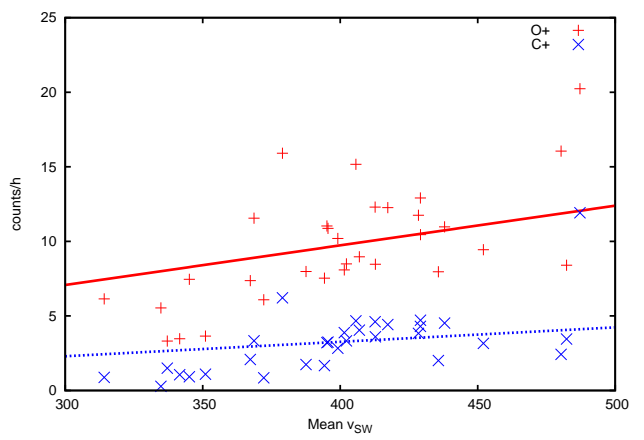


Figure 3. Averaged counts per hour of heavy pick up ions are plotted over the corresponding mean solar wind velocity. The averaged count rate per hour was derived with equation 2, while the mean solar wind velocity is averaged over 27 days. There is a small linear dependence of counts with v_{SW} , which is probably caused by an insufficient coverage of velocity bins in some 27-day bins.

where d denotes the flight path of ions in the instrument and V_{PAC} the post acceleration voltage. $\alpha(E, m)$ describes the species dependent energy loss in the carbon foil.

The m/q spectrum is then fitted by a combination of four gaussian using the derived m/q values from table 1 as the center of density. From the fit we see that overlap of the four discrete heavy PUI distribution prevents us from defining m/q ranges for the less abundant heavy pick up ions, i.e. nitrogen and neon. Nevertheless, contributions to the O^+ and C^+ distribution by N^+ and Ne^+ can be neglected, considering their relative abundance with respect to oxygen and carbon. Thus, we define an upper/lower limit of mass per charge for C^+ and O^+ , which is our criterion for species classification (presented in table 1).

The large variability of count rates seen in Fig. 2 are the result of two effects. On the one hand, as already alluded to, the probability to trigger a valid event depends on the velocity of the ion. On the other hand, within one single temporal bin, many different values for solar wind speed are likely to have occurred. If we consider long time bins, we can remove part of the velocity dependence by giving every velocity bin an equal weight. This can be done even if we do not know the exact velocity or energy dependence of the detection efficiency. Therefore, we consider, from now on, only long-term averages and bin all quantities into 27-day temporal bins. Within one 27-day bin, we consider hourly values for the pickup-ion count rates our basic data product and divide the velocity range $300 \text{ km/s} < v < 1000 \text{ km/s}$ into 7 velocity bins, each 100 km/s wide. We now count how often every velocity bin occurs and call that number N_{v,t_b} , where t_b is the time of the temporal (27-day) bin. In each

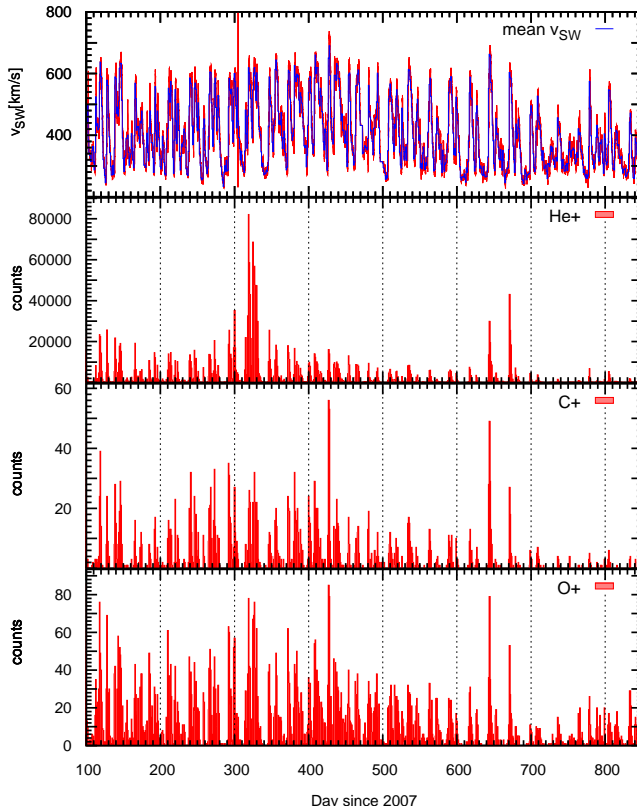


Figure 4. The lower three panels show time series of count rates of He^+ , O^+ and C^+ using a bin width of 24 hours. The topmost panel shows the corresponding proton bulk velocity.

velocity bin, we count the number of pickup ions measured, C_{v,t_b} . In order to be able to compare the results from time bin b with those in time bin $b + 1$, we need to ensure that all velocity bins have the same weight. Therefore, we sum the ratio of pickup-on counts per velocity bin, $C_{v,t}$, with the number of occurrences of that bin, N_{v,t_b} and divide it by the length of the temporal bin, t_w , expressed in hours. This then gives us a smoothed value for the hourly count rate, \bar{C}_{t_b} ,

$$\bar{C}_{t_b} = \sum_{t=t_b}^{t_b+t_w} \sum_v \frac{C_{v,t}}{N_{v,t_b} t_w}, \quad (2)$$

The length of the time bin, t_w is determined by some typical time scale, in our case, solar rotation. Choosing one solar rotation as the time width should remove most of the remaining velocity dependence because of the quasi-regular recurrence of high speed streams and slow wind in this unique period of solar activity. Therefore, we chose a bin width, t_w , of 27 days. Note that this is not really the rotation period at STEREO A, where it would be 28 days, neither is it that of STEREO B where it would be about 26 days, but the average of the two, which also coincides with the synodic rotation period. This choice assures that we can compare our data with observations with STEREO B or

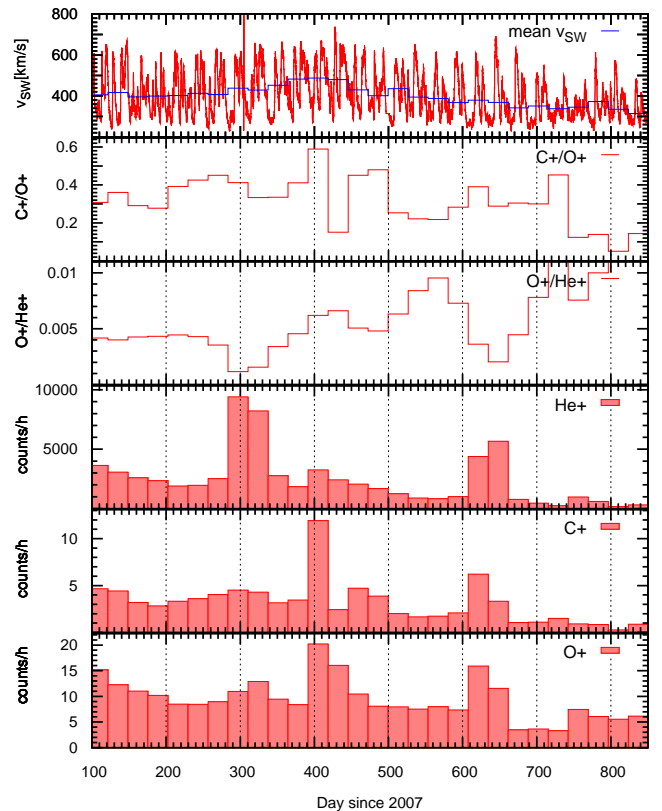


Figure 5. Mean pick up ion count rates of STEREO A for a period of 750 days. Counts are binned over 27 days and normalized to a constant occurrence of velocity bins with a width of 100 km/s (Consult text for details on the binning procedure). The lower three panels show time series of mean count rates of O^+ , C^+ and He^+ and the two panels above show ratios of O^+/He^+ and C^+/O^+ . The topmost panel shows the corresponding proton bulk velocity.

with ACE or SOHO. Note that this procedure also reduces the effect of compression areas because these typically contain several velocity bins. The remaining and now relatively weak velocity dependence can be seen in Fig. 3 which shows the resulting averaged counts per hour of oxygen (+) and carbon (+) pick up ions plotted vs. their corresponding rotation-averaged solar wind speed. If our binning procedure removed the efficiency dependence, we would expect no correlation between averaged counts and mean velocity. This is not the case, the count rates still vary by a factor slightly less than two over a solar wind speed range from just above 300 km/s to just below 500 km/s. The linear fits which are also shown are partially driven by the points associated with the enhancement of C⁺ and O⁺ around day 420. Because the change in average solar wind speed between adjacent solar rotations is small, we have chosen to ignore this remaining weak dependence, but need to remember that our results can be uncertain to within a factor of two if we compare data from periods of different solar wind speeds.

3. Data Interpretation

We are now able to create time series of pickup-ion count rates for He⁺, C⁺ and O⁺ with a maximum resolution of one hour. Pickup helium (He⁺) data was accumulated in analogy to the heavy PUIs by defining an upper/lower limit of τ and E_{res} per energy step in an E/q range from 80 keV/e to 5 keV/e. A 700-day time series beginning in February 2007 is presented in Fig. 4 together with solar wind velocity. Apart from the already mentioned detection-efficiency-related correlation of count rate with solar wind speed, several structures are visible. Most noticeable is an enrichment of He⁺, C⁺ and O⁺ around days 320 and 640 which coincide with the traversal of the Helium focusing cone by STEREO A. The enrichment of carbon and oxygen in these periods will be discussed shortly.

Although small-scale structures, which could be related to CMEs or other phenomena, are observable (e.g. day 420), we won't discuss any of these features because we are not applying any efficiency correction in this work. Instead, we will focus our investigation on major structures, which then allows a long-term time binning in combination with a velocity binning and assures a nearly constant detection efficiency over time.

Figure 5 shows the same time period as Fig. 4, but using the binning procedure given by equation 2 and discussed above. We again see the helium cone traversal on days 300 and 640 within uncertainties of ± 27 days caused by the chosen bin width of 27 days. However, there is also a noticeable enrichment of carbon and oxygen during the periods of the helium focusing cone traversal. This enrichment of C and O is considerably more pronounced during STEREO A's second passage of the He focusing cone.

The He focusing cone appears to be more pronounced on day 300 than on the second passage around day 640. This could be an effect of changes in the instrument settings, especially adjustments of the Micro Channel Plate (MCP) bias voltage, or also an effect of MCP aging. While this is important for detailed studies, this apparent change in the intensity of the focusing will not influence our findings detailed below. Several sources [Möbius *et al.*, 1985; Gloeckler and Geiss, 1998; Bertaux *et al.*, 1985] have confirmed He⁺ to be mainly of interstellar origin, with the ensuing gravitational focusing of interstellar neutral helium being the source of the enrichment during passage of the focusing cone. However, neutral interstellar oxygen and carbon are ionized much farther out in the heliosphere than He because of their higher ionization probability. Their abundance within one AU is

depleted by two orders of magnitude, which tells us that interstellar C and O can not be responsible for the increase of C and O count rates during the traversal of the helium cone. Moreover, the ratio of carbon to oxygen count rates does not change appreciably across the focusing cone. The solar wind C/O ratio is relatively constant over the velocity ranges covered in these and the adjacent time periods. While the absolute value of C/O derived directly from count rates, without applying calibration data, may still be off by a factor of two or so, the fact that we do not see a noticeable change in this ratio tells us that there is, indeed, no appreciable contribution from interstellar C or O during these periods. This is all the more remarkable, as Gloeckler and Geiss [1998] give a value of 0.05 for the interstellar C/O in the heliosphere, nearly an order of magnitude different from the (uncalibrated) value observed by PLASTIC, and, more importantly, an order of magnitude different from the solar wind value of $\sim 0.6 - 0.7$.

Given the discussion in the previous section, let us make the reasonable assumption that C/O in most other time periods in Fig. 5 is dominated by inner-source C and O. This has nearly solar wind composition which dramatically differs from that of the interstellar medium. Therefore, the enhancements of C and O can not be due to interstellar C and O, but must come from another source.

On the other hand, we do see a clear drop in the ratio of O⁺/He⁺ during both cone traversals. Again, 27-day averaged solar wind velocities do not change appreciably across this time period, they do also not coincide with instrumental changes such as increases in MCP bias voltage. Therefore, we argue, the enhancements of C and O during the traversals of the He focusing cone are real.

4. Discussion and Conclusions

Using data from the PLASTIC instrument aboard STEREO, we have observed enhancements of the count rate in He⁺ during passage of the so-called focusing cone. It is generally believed that these enhancements are due to the gravitational focusing of interstellar helium on its passage through the heliosphere. The thus enhanced neutral He density results in an enhanced production rate of pick up He⁺ which can be and has been observed [Möbius *et al.*, 1985; Gloeckler *et al.*, 2004]. Coincident with these enhancements in He⁺, we have also observed enhancements of singly charged carbon and oxygen ions. We have argued that these enhancements are real and can not be due to instrumental effects. Because both C⁺ and O⁺ are predominantly not of interstellar origin, these coincident enhancements can not be a consequence of focused interstellar C and O, but must be due to some other effect. One possible cause of these enhancements could be the focusing of interstellar dust which may serve as a catalyst in producing inner-source pickup ions, or be a direct source of the volatile C and O if interstellar dust grains retain enough condensed C and O which is then liberated in the vicinity of the Sun.

Acknowledgments.

This work was supported, in parts, by the German Science Foundation, DFG, under grant Wi-2139/4-1 and NASA STEREO Contract NAS5-00132 at UNH.

References

- Bertaux, J. L., R. Lallement, V. G. Kurt, and E. N. Mironova (1985), Characteristics of the local interstellar hydrogen determined from PROGNOZ 5 and 6 interplanetary Lyman-alpha line profile measurements with a hydrogen absorption cell, *Astron. Astrophys.*, , 150, 1–20.

- Galvin, A. B., L. M. Kistler, M. A. Popecki, C. J. Farrugia, K. D. C. Simunac, L. Ellis, E. Möbius, M. A. Lee, M. Boehm, J. Carroll, A. Crawshaw, M. Conti, P. Demaine, S. Ellis, J. A. Gaidos, J. Googins, M. Granoff, A. Gustafson, D. Heirtzler, B. King, U. Knauss, J. Levasseur, S. Longworth, K. Singer, S. Turco, P. Vachon, M. Vosbury, M. Widholm, L. M. Blush, R. Karrer, P. Bochsler, H. Daoudi, A. Etter, J. Fischer, J. Jost, A. Opitz, M. Sigrist, P. Wurz, B. Klecker, M. Ertl, E. Seidenschwang, R. F. Wimmer-Schweingruber, M. Koeten, B. Thompson, and D. Steinfeld (2008), The Plasma and Suprathermal Ion Composition (PLASTIC) Investigation on the STEREO Observatories, *Space Sci. Rev.*, **136**, 437–486, doi:10.1007/s11214-007-9296-x.
- Gloeckler, G., and J. Geiss (1998), Measurement of the abundance of helium-3 in the sun and in the local interstellar cloud with SWICS on Ulysses, *Space Sci. Rev.*, **84**, 275 – 284.
- Gloeckler, G., and J. Geiss (1998), Interstellar and Inner Source Pickup Ions Observed with SWICS on ULYSSES, *Space Science Reviews*, **86**, 127–159, doi:10.1023/A:1005019628054.
- Gloeckler, G., J. Cain, F. M. Ipavich, E. O. Tums, P. Bedini, L. A. Fisk, T. Zurbuchen, P. Bochsler, J. Fischer, R. F. Wimmer-Schweingruber, J. Geiss, and R. Kallenbach (1998), Investigation of the composition of solar and interstellar matter using solar wind and pickup ion measurements with SWICS and SWIMS on the ACE spacecraft, *Space Sci. Rev.*, **86**, 497 – 539.
- Gloeckler, G., L. A. Fisk, S. Hefti, N. Schwadron, T. Zurbuchen, F. M. Ipavich, J. Geiss, P. Bochsler, and R. Wimmer (1999), Unusual composition of the solar wind in the 2 May 1998 CME observed with SWICS on ACE, *Geophys. Res. Lett.*, **26**, 157 – 160.
- Gloeckler, G., L. A. Fisk, J. Geiss, N. A. Schwadron, and T. H. Zurbuchen (2000), Elemental composition of the inner source pickup ions, *J. Geophys. Res.*, **105**, 7459 – 7463.
- Gloeckler, G., E. Möbius, J. Geiss, M. Bzowski, S. Chalov, H. Fahr, D. R. McMullin, H. Noda, M. Oka, D. Ruciński, R. Skoug, T. Terasawa, R. von Steiger, A. Yamazaki, and T. Zurbuchen (2004), Observations of the helium focusing cone with pickup ions, *Astron. Astrophys.*, **426**, 845–854, doi: 10.1051/0004-6361:20035768.
- Kaiser, M. L., T. A. Kucera, J. M. Davila, O. C. St. Cyr, M. Guhathakurta, and E. Christian (2008), The STEREO Mission: An Introduction, *Space Science Reviews*, **136**, 5–16, doi:10.1007/s11214-007-9277-0.
- Möbius, E., D. Hovestadt, B. Klecker, M. Scholer, G. Gloeckler, and F. M. Ipavich (1985), Direct observation of He^+ pick-up ions of interstellar origin in the solar wind, *Nature*, **318**, 426 – 429.
- Schwadron, N. A., J. Geiss, L. A. Fisk, G. Gloeckler, T. H. Zurbuchen, and R. v. Steiger (2000), Inner source distributions: Theoretical interpretation, implications, and evidence for inner source protons, *J. Geophys. Res.*, **105**, 7465 – 7472.
- Wimmer-Schweingruber, R. F., and P. Bochsler (2003), On the origin of inner-source pickup ions, *Geophys. Res. Lett.*, **30**, 1077 – 1080, DOI: 10.1029/2002GL015218.

Christian Drews, Institut für experimentelle und angewandte Physik, Christian-Albrechts-Universität zu Kiel, Leibnizstr. 11, 24118 Kiel, Germany (drews@physik.uni-kiel.de)

Lars Berger, Institut für experimentelle und angewandte Physik, Christian-Albrechts-Universität zu Kiel, Leibnizstr. 11, 24118 Kiel, Germany (berger@physik.uni-kiel.de)

Robert F. Wimmer-Schweingruber, Institut für experimentelle und angewandte Physik, Christian-Albrechts-Universität zu Kiel, Leibnizstr. 11, 24118 Kiel, Germany (wimmer@physik.uni-kiel.de)

List of Abbreviations

ACE	Advanced Composition Explorer
AU	Astronomical Unit
CIR	Corotating Interaction Region
CME	Coronal Mass Ejection
DPU	Data Processing Unit
ESA	ElectroStatic Analyzer
ESEA	Entrance System / Energy Analyzer
ET	Energy / Time-of-flight
FIP	First Ionization Potential
FOV	Field Of View
FWHM	Full Width at Half Maximum
IDPU	Instrument Data Processing Unit
ISPUI	Inner-Source Pick-Up Ion
LIC	Local Interstellar Cloud
LISM	Local InterStellar Medium
MCP	Micro Channel Plate
PHA	Pulse Height Analysis
PIPS	Passivated Implanted Planar Silicon
PLASTIC	PLAsma and Suprathermal Ion Composition
PUI	Pick-Up Ion
SSD	Solid State Detector
STEREO	Solar TErestrial RElations Observatory
SWICS	Solar Wind Ion Composition Spectrometer
SWS	Solar Wind Section
TOF	Time-Of-Flight
WAP	Wide Angle Partition
WAPNOSSD	Wide Angle Partition (without residual energy measurement)
WAPSSD	Wide Angle Partition (with residual energy measurement)

Bibliography

- Allegrini, F., Ion optical calibration of the PLASTIC sensor on STEREO, Ph.D. thesis, Universitaet Bern, Philisophische Naturwissenschaftliche Fakultaet, 2007.
- Berger, L., Velocity Distribution Functions of Heavy Ions in the Solar Wind at 1 AU, Ph.D. thesis, Christian-Albrechts-Universitaet Kiel, Mathematisch-Naturwissenschaftliche Fakultaet, 2008.
- Berger, L., Private Discussion, 2009.
- Bertaux, J., R. Lallement, V. G. Kurt, and E. N. Mironova, Characteristics of the local interstellar hydrogen determined from pognoz 5 and 6 interplanetary lyman-alpha line profile measurements with a hydrogen absorption cell, *Astronomy and Astrophysics*, 150, 1–20, 1985.
- Bertaux, J. L., Evidence for a source of an extraterrestrial hydrogen lyman-alpha emission, *Astronomy and Astrophysics*, 11, 200, 1971.
- Blush, L., F. Allegrini, and P. Bochsler, Development and calibration of major components for the stereo/plastic instrument, *Adv. Space Res.*, 36, 1544–1556, 2005.
- Bzowski, M., and M. Krolikowska, Are the sungrazing comets the inner source of pickup ions and energetic neutrals, *The Astrophysical Journal*, 435, 723–732, 2005.
- Cummings, A., E. Stone, and C. Steenberg, Composition of anomalous cosmic rays and other heliospheric ions, *The Astrophysical Journal*, pp. 194–210, 2002.
- Fisk, L., Motion of the footpoints of heliospheric magnetic field lines at the sun: Implications for recurrent energetic particle events at high heliographic latitudes, *Geophysical Research*, 15, 547–553, 1996.
- Galvin, A., et al., The plasma and suprathermal ion composition (plastic) investigation on the stereo observatories, *Space Science Review* (2008), 136, 437–486, 2007.
- Geiss, J., G. Gloeckler, U. Mall, R. von Steiger, A. B. Galvin, and K. W. Ogilvie, Interstellar oxygen, nitrogen and neon in the heliosphere, *Astronomy and Astrophysics*, 282, 924–933, 1993.
- Geiss, J., G. Gloeckler, L. Fisk, and R. von Steiger, C⁺ pick-up ions in the heliosphere and their origin, *Geophysical Research*, pp. 373–377, 1995.
- Gloeckler, G., Cometary pick-up ions observed near giacobini-zinner, *Geophysical Research*, 13, 251–254, 1986.
- Gloeckler, G., Interception of comet hyakutakes ion tail at a distance of 500 millionkilometres, *Nature*, 404, 576–578, 2000.

- Gloeckler, G., and J. Geiss, Interstellar and inner source pick-up ions observed with swics, *Space Science Review*, 86, 127–159, 1998.
- Gloeckler, G., E. Möbius, J. Geiss, M. Bzowski, S. Chalov, and H. Fahr, Observations of the helium focusing cone with pickup ions, *Astronomy and Astrophysics*, 426, 845–854, 2004.
- Greenberg, J. M., Morphological structure and chemical composition of cometary nuclei and dust, *Adv. Space Res.*, 90, 149–161, 1999.
- Grün, E., B. Gustafson, L. Mann, M. Baguhl, G. E. Morfill, A. Taylor, and H. Zook, Interstellar dust in the heliosphere, *Astronomy and Astrophysics*, 286, 915–924, 1994.
- Kallenbach, R., J. Geiss, G. Gloeckler, and R. von Steiger, Pick-up ion measurements in the heliosphere - a review, *Astrophysics and Space Science*, 274, 97–114, 2000.
- Kallenrode, M.-B., *Space Physics: An Introduction to Plasmas and Particles in the Heliosphere and Magnetospheres*, Springer Verlag, 2004.
- Karrer, R., Ion optical calibration of the PLASTIC sensor on STEREO, Ph.D. thesis, Universitaet Bern, Philisophische Naturwissenschaftliche Fakultaet, 2007.
- Kistler, L., and L. Ellis, *Level 1 Data Document*, 2007.
- Köten, M., Detection efficiencies for STEREO/PLASTIC and ACE/SWICS, Master's thesis, Christian-Albrechts-Universitaet Kiel, Mathematisch-Naturwissenschaftliche Fakultaet, 2005.
- Krüger, H., and E. Grün, Interstellar dust inside and outside the heliosphere, *Space Science Review*, 143, 347–356, 2008.
- Longworth, S. P., *Logic Reference Document*, Revision 2.0.
- Luhmann, J., D. Curtis, and P. Schroeder, Stereo impact investigation goals, measurements, and data products overview, *The STEREO Mission*, pp. 117–185, 2007.
- Marsch, E., R. Schwenn, H. Rosenbauer, K. H. Mühlhauser, W. Pillip, and F. M. Neubauer, Solar wind protons - three-dimensional velocity distributions and derived plasma parameters measured between 0.3 and 1 au, *Geophysical Research*, 87, 52–72, 1982.
- Marsden, B. G., Sungrazing comets, *The Astrophysical Journal*, 43, 75–102, 2005.
- Möbius, E., D. Hovestadt, B. Klecker, G. Gloeckler, and F. M. Ipavich, Direct observation of he+ pick-up ions of interstellar origin in the solar wind, *Nature*, 318, 426–429, 1985.
- Moebius, E., He pickup ion observation in the inner heliosphere, in *PLASTIC Teleconference*, pp. 16–18, 2009.
- Moebius, E., and B. Klecker, Private Discussion, 2009.
- Schwadron, N., and J. Geiss, On the processing and transport of inner source hydrogen, *Geophysical Research*, 105, 7473–7481, 2000.

- Sekanina, Z., Solar and heliospheric observatory sungrazing comets with prominent tails: Evidence on dust-production peculiarities, *The Astrophysical Journal*, 545, 69–72, 2000.
- Vasyliunas, V. M., and G. Siscoe, On the flux and the energy spectrum of interstellar ions in the solar system, *Geophysical Research*, pp. 1247–1252, 1976.
- von Steiger, R., Variable carbon and oxygen abundances in the solar wind as observed in earths magnetosheath by ampte/cc, *The Astrophysical Journal*, pp. 791–799, 1991.
- von Steiger, R., N. A. Schwadron, L. A. Fisk, J. Geiss, G. Gloeckler, S. Hefti, B. Wilken, R. F. Wimmer-Schweingruber, and T. H. Zurbuchen, Composition of quasi-stationary solar wind flows from ulysses/swics, *Geophysical Research*, pp. 217–227, 2000.
- Wimmer-Schweingruber, R. F., and P. Bochsler, On the origin of inner-source pickup ions, *Geophysical Research*, 30, 1077, 2002.

Danksagung

An erster Stelle danke ich Herrn Prof. Dr. R. F. Wimmer-Schweingruber und Dr. L. Berger für die sehr gute Betreuung dieser Arbeit.

Mein Dank geht auch an alle anderen Mitglieder der Arbeitsgruppe Extraterrestrik der Universität Kiel. Besonders hervorzuheben ist die Hilfe von Dipl.-Phys. Onno Kortmann und Michael Buttgereit in Sachen EDV, die Unterstützung von Dr. M. Koeten bei der "in-flight" Kalibrierung des Instrumentes, die Unterstützung von cand.-Phys. Viktor Hrkac bei der Datenauswertung und Dipl.-Phys. Bent Ehresmann, Dipl.-Phys. Rolf Paspircgilis und Dr. R. Rodde für das Korrekturlesen dieser Arbeit.

Zusätzlich danke ich der Arbeitsgruppe "Department of Physics" der Universität New Hampshire für die Unterstützung hinsichtlich des Instrumentes PLASTIC.

Ganz besonders danke ich meiner Familie, Gert Anold Drews, Veronika Drews, Stefanie Drews und meiner Freundin, Stefanie Beyer, für die moralische Unterstützung ohne die eine Fertigstellung dieser Arbeit nicht möglich gewesen wäre.

Eidesstattliche Erklärung

Ich versichere hiermit, dass ich meine Diplomarbeit mit dem Thema

Flux of Suprathermal Ions measured by STEREO PLASTIC

selbstständig verfasst und keine anderen als die angegebenen Quellen und Hilfsmittel benutzt habe. Die Arbeit wurde bisher keiner anderen Prüfungsbehörde vorgelegt und auch nicht veröffentlicht.

Kiel, September 28, 2009

Christian Drews